UAB

Universitat Autònoma de Barcelona

UAB

Universitat Autònoma de Barcelona

DOCTORAL THESIS

Hybrid plasmonic-photonic nanostructures for enhanced spectroscopies

Author
Cristiano Matricardi

Director
Agustín Mihi

Tutor
Jordi Hernando

Science faculty Chemistry department

Doctoral program in Material Science

Instituto de ciencia de materiales de Barcelona
Nanostructured Materials for Optoelectronics and Energy Harvesting

ICMAB

Academic year - 2020

CSIC

ACKNOWLEDGEMENT

MOTIVATION

"What matter most is how well you walk
through the fire of your comfort zone"
Charles Bukowski

There is an increasing interest in the use of nanostructures to improve light matter interaction. In this context, nanostructured metals have been taken into consideration due to their exciting optical properties. Their properties arise from the interaction of the incoming photons and the free electron cloud in the metal, leading to very high electric field confinement with potential use in near field optical sensing, light trapping or photodetection. To excite these plasmon resonances in a metal, one has to account for the momentum mismatch between the bound surface plasmon polariton and the free propagating incoming photon. This additional momentum can be provided, for instance, by scattering of nanoparticles, a prism or a diffraction grating. The latter configuration is advantageous since the periodicity of the architecture determines the frequencies at which surface plasmon polaritons (SPPs) are excited, irrespective of the plasmon frequency of the metal. Thus, if the metal is periodically corrugated, surface plasmons can interfere forming standing waves. This is the case of Plasmonic Crystals, metallic architectures with periodically organized motifs engineered to sustain new resonant hybrid modes. Actually, plasmonic crystals can sustain a wide variety of plasmonic resonances (propagating and localized) that can further couple with each other to produce strong hybrid resonances. The scope of this thesis is to explore how some scalable and straightforward nanofabrication techniques can be used to achieve complex nanostructures that can intensively interact with the visible and near infrared light giving rise to these hybrid resonances. These novel architectures will be fabricated via soft nanoimprinting lithography. As the word "*soft*" says, this procedure involves materials like polymers and resins whose stiffness is way

lower than that of materials used in electron beam lithography, interference lithography and other techniques of nanofabrication. The novel plasmonic crystals fabricated in this work show interesting properties that extend the light confinement typical of single nanoparticles adding control over spatial distribution and control over radiation properties such as polarization. We are ready to start our discussion regarding this rich world. We will unveil how objects hundred thousand times smaller than a hair can be designed to make possible the manipulation of light. We take light , squeeze it to the nanoscale, we concentrate and mold its flow, and let it propagate where and how we want

PREFACE

This dissertation is the result the work carried out in the Nanostructured Materials for Optoelectronics and Energy Harvesting (NANOPTO) research group at the Institute of Materials Science of Barcelona. Part of this work was conducted in collaboration with the Bionanoplasmonic group at the CIC BiomaGUNE in San Sebastian. This work is dedicated to the nanofabrication, characterization and application of complex plasmonic nanostructures with engineered optical properties. The manuscript is divided in three sections, which in turn are divided in several chapters.

SECTION I. This section is divided into two chapters each one addressing different aspects of nanotechnology. **Chapter 1** summarizes the importance of plasmonics giving some examples on how it has accompanied us since ancient times. Subsequently, a theoretical discussion on the optical properties gives us the tools to study and understand plasmonic effects and allow us to decide which material fits better for plasmonic applications. Then a brief discussion on the state of the art of plasmonics will highlight how this field is rapidly changing looking for more efficient devices. The emphasis will be put on two techniques used in this work such as Surface Enhanced Fluorescence (SEF) and Surface Enhanced Raman Scattering (SERS). **Chapter 2** describes different approaches to fabricate nanostructured devices, namely top down and bottom up, discusses the main characterization techniques and highlights the strength of unconventional fabrication methods based in soft nanoimprinting methods. The description will include the protocol used for the fabrication of molds for nanoimprint lithography used in this work.

SECTION II. This section is composed by the **Chapter 3** and is dedicated to the fabrication, optical characterization and surface enhanced fluorescence studies

with asymmetric plasmonic crystals. The fabrication process combines thermal nanoimprint lithography (top down) with tilted thermal evaporation (bottom up). The experimental parameters will be treated in detail to achieve high reproducibility over large areas as well as tunability of the optical properties. The symmetry breaking leads to asymmetric optical response that can be efficiently engineered to perform polarization selective fluorescence enhancement. Furthermore, the ease of tunability of geometrical parameter along with the throughput of nanoimprint lithography leads to the fabrication of large array of homogeneous nanogaps that has been demonstrated to have outstanding performance in surface enhanced fluorescence.

SECTION III. This section is devoted to the merger of two different techniques namely nanoimprint lithography (top-down) and nanoparticles self-assembly (bottom-up). **<u>Chapter 4</u>** describes in detail the template self-assembly process from its basic concepts to the key parameter that affects the assembly and long-range homogeneity. In this discussion will be presented a new controlled method to achieve template self-assembly form both gold nanospheres and nanorods. The optical characterization reveals the hybridization between localized plasmon resonances and diffraction modes which allows the tuning of resonances by changing the lattice parameter of the array. **<u>Chapter 5</u>** will be devoted to the application of supercrystals as Surface enhanced Raman spectroscopy sensors. This study unveils the optimal geometrical parameters and conditions to achieve the maximum enhancement when working with infrared laser that are known to be useful in biology but at the same time extremely inefficient in solution based of other not enhanced methods.

LIST OF ABBREVIATION

AFM	Atomic Force Microscopy
EBL	Electron Beam Lithography
EM	Electromagnetic
FDTD	Finite Difference Time Domain
FTIR	Fourier Transform Infrared Spectroscopy
FWHM	Full Width Half Maximum
IR	Infrared
LSP	Localized Surface Plasmon
NIL	Nanoimprint Lithography
NIR	Near infrared
PDMS	Polydimthylsiloxane
PMMA	Poli(methylmethacrylate)
SEF	Surface enhanced fluorescence
SEM	Scanning electron Microscopy
SERS	Surface enhanced Raman Spectroscopy
SLR	Surface Lattice Resonance
SP	Surface Plasmon
SPP	Surface Plasmon Polariton
SPR	Surface plasmon resonance
UV	Ultraviolet
VIS	Visible

TABLE OF CONTENTS

SECTION I

CHAPTER ONE
INTRODUCTION TO PLASMONICS

CHAPTER TWO
NANOFABRICATION AND CHARATERIZATION OF NANOSTRUCTURES

SECTION II

CHAPTER THREE
ASYMMETRIC PLASMONIC CRYSTALS WITH TUNABLE OPTICAL PROPERTIES

SECTION III

CHAPTER FOUR
TEMPLATE SELF-ASSEMBLY OF GOLD NANOPARTICELS SUPERCRYSTALS

CHAPTER FIVE

TUNABLE PLASMONIC SUPERCRYSTALS FOR SERS

GENERAL CONCLUSIONS AND OUTLOOKS

APPENDIX A

SECTION I

INTRODUCTION

CHAPTER ONE

INTRODUCTION TO PLASMONICS

T his chapter will explore the basic principles of plasmonic crystals and provide tools to correctly understand the physical and chemical concepts involved in this work. On one hand we have Plasmons, collective oscillations of free electrons in solid materials. Whether those oscillations are confined in a small particle or on a flat surface, they can give rise to resonances that are strictly localized or that can propagate along the surface. Plasmonics is a science that deals with all those kinds of resonances and plays with them modifying their oscillation frequencies, intensities as well as their location and nature. On the other hand, we have ordered arrays of nanostructures that modify the propagation of photons in the same way ionic lattices do with electrons in crystalline solids. Those arrays are called photonic crystals and give us a tool to play with light, modifying the propagation direction, through diffraction of the incident beam. At this point, when plasmonics meets photonics a new class of materials can be designed and by their union we can engineer which incident energies of light we want to harvest or concentrate in our metal surface in order to give rise to a world of physical phenomena that nowadays are exploited in various fields of science: biology, photovoltaics, catalysis, chemical sensing, applied optics, fundamental physics, these fields are experiencing a revolutionary change thanks to new plasmonic systems. In order to understand the importance of plasmonics for the development of this thesis I will put emphasis on the concepts that let us understand what plasmons are, which type of plasmons can exist under different conditions, and how relevant are in spectroscopic applications.

~ ● ~

1.1 INTRODUCTION

Plasmonics is a rapidly growing and well-established research field, which covers various aspects of surface plasmons towards the realization of a variety of surface-plasmon-based devices.

The phenomenon of surface plasmon polaritons has been known for a long time. Already in 1902, R. W. Wood, while monitoring the spectrum of white light after reflection by an metallic grating, noticed, "I was astounded to find under certain conditions a drop from maximum illumination to minimum. The drop certainly from 10 to 1, occurred within a range of wavelengths not greater than the distance between the sodium lines".[1] This first experiment revealed something that had much more ancient roots. An example of the use of plasmonic effects is the famous Lycurgus cup, whose colors are originated in metals colloids, dated back to the Roman Empire. Everyone working in this field have this precious example in mind when thinking at the origin of plasmonics. However, another illustration where plasmonics effects reveal their potential is photography. In particular the ancestor of photography: the Daguerreotype. This technique was the first successful form of photography, named after Louis-Jacques-Mandé Daguerre, who invented the technique in collaboration with Nicéphore Niépce in the 1830s. Daguerre and Niépce found that if a copper plate coated with silver iodide was exposed to light in a camera, then fumed with mercury vapors and fixed (made permanent) by a solution of common salt, a permanent image would be formed. The revolution was not only due to the fact that an image can be fixed on a substrate but also because the extremely high resolution was a real photography breakthrough at that time. These first images have also other unique optical characteristics, including a high sensitivity to viewing angle, and occasionally, subtle coloration. Because of the long exposure times required for capturing an image, the subject matter was frequently buildings or landscapes imaged under natural lighting, and many of these images show the surprisingly realistic coloration of a blue-sky background as shown in Figure 1.1a. Their unique sensitivity to viewing angle provides a critical clue to the nature of the

chemistry of daguerreotypes: the image-rendering chemistry involves the creation of nanoparticles capable of redirecting incident light in a spectrally dependent manner (Figure 1.1b), rather than merely absorbing light and creating a flat contrast, as one would anticipate with molecular chromophores used in subsequent photographic processes. Size, shape, and chemical concentration of metallic nanoparticles formed during exposure to light, give rise to the characteristics of daguerreotype images[2].
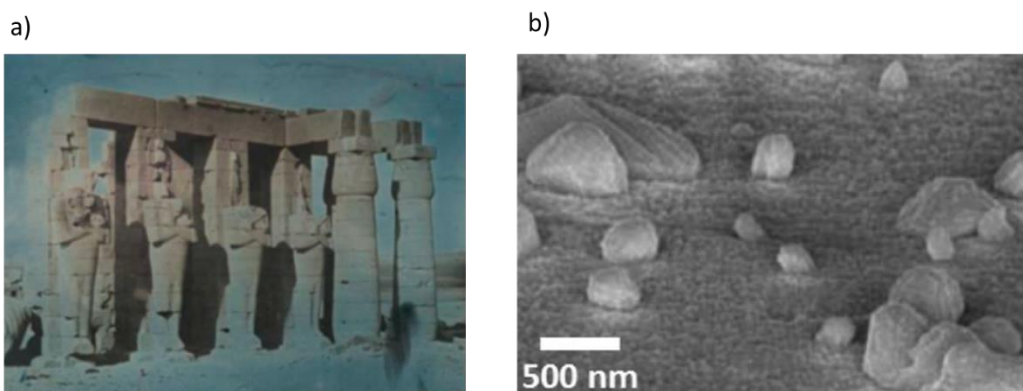
Figure 1.1 Examples of 19th- and 21st-century images composed of plasmonic nanoparticles and nanostructures. (a) Daguerreotype Ramesseum, Thebes, 1844. Girault de Prangey, The Metropolitan Museum of Art. Purchase, 2016. (b) Representative scanning electron microscope (SEM) image of Ag–Hg nanostructures deposited on Ag support film that constitutes the daguerreotype image. Reprinted from ref.2.

The formation of daguerreotype involves the nucleation and growth of Ag–Hg alloyed nanoparticles on an underlying Ag photographic plate. The size and density of the nanoparticles resulting from the development process differ depending upon illumination conditions, creating different areas of contrast that constitute the final image. The exquisite spatial resolution characteristic of daguerreotype images results from the nanoscale variations of the nanoparticles that constitute the developed image[3].

The issue now is more philosophical than technical. Actually, chemical methods of recording images have been surpassed by electronic ones; however, one may wonder if the development of photography would have followed a different path if the plasmonic effects underlying the daguerreotype had been unveiled earlier. The possible evolution of daguerreotypy can be only

speculated, nevertheless the recent developments of plasmonics move toward the integration with modern electronic image acquisition and storage techniques. In this regard active nanoscale antennas can be used to facilitate selective photodetection and image acquisition[4]. Plasmonics will further extend the sensitivity to regions of the spectrum beyond visible light[5]. In these cases, light interaction is controlled by the properties of the plasmonic nanostructures themselves and would allow the merger of the ancient method of image capture with future sensors and digital acquisition.

In this chapter I will present the main theoretical aspect of plasmonics and an overview of application together with some of the last advances in this field. Particular attention will be given to optical spectroscopies such as surface enhanced Raman scattering and surface enhanced fluorescence.

1.2 OPTICAL PROPERTIES OF METALS

Nobel metals such as gold (Au), silver (Ag), copper (Cu), or Aluminum (Al), have long been known for their optical properties different from standard dielectrics. These metals reflect light very efficiently in the visible, making them optimum materials for mirrors. These particular properties along with excellent electrical and heat conductivity have the same physical origin: the presence of free conduction electrons. In this context, while the conductivity is quite straightforward an intuitive to understand, the connection of the optical properties with free electrons may sometimes appear less trivial. Free electrons in metals move in a background of fixed positive ions that ensures the overall neutrality. This oscillation is by definition a plasma. In our case can be also called solid state plasma and it governs the optical properties of metals at least in the visible and near infrared (NIR) regime.

Several factors affect and contribute to the complexity of these free electron oscillation. The interaction of electrons with the underlying periodic structure ions, the electron-electron correlation, the interaction of electrons with impurities and phonons and last but not least the presence of surfaces. In the following paragraphs we will describe the basic concept underlying the relation of matter with electromagnetic (EM) waves. The emphasis will be on metals

rather than other materials, since the goal is primarily to understand why metals are so special for plasmonic applications.

1.2.1   Light – matter interaction

Light-matter interaction is one of the most interesting phenomena in nature and gives rise to a multitude of thermal, optical or electronical effects. Two important parameters describe the interaction between electromagnetic waves and materials: polarization and magnetization. Those phenomena are described by the following expressions:

$$P(E) = \varepsilon_0 \chi_e E \tag{1}$$

$$M(H) = \chi_m H \tag{2}$$

where ε_0 is the permittivity of the material in vacuum, χ_e, χ_m the electric and magnetic susceptibility, E and H are respectively the external electric and magnetic fields. The polarization describes the density of electric dipole moment induced by the external field. We could make similar assumption for magnetization but at optical frequencies this effect is negligible. However, in modern nano optics particular geometries could introduce a strong magnetization as in the case of some metamaterials and high dielectric nanostructures.[6,7] In this thesis we focus the study only on the electric aspects induced in the structure. The electrical polarization can be described by complex electrical permittivity of the material, or dielectric function $\varepsilon_{(\omega)}$.

$$\varepsilon_{(\omega)} = \varepsilon'_{(\omega)} + i\varepsilon''_{(\omega)} \tag{3}$$

This expression illustrates how that polarization response depends on the frequency of the external electromagnetic field. Moreover, the real part of the dielectric function (ε') describes the strength of the polarization induced by the external electric field and the imaginary part (ε'') describes the losses encountered in polarizing the material, so it gives a quantitative value of the attenuations of the field inside the material. When working at UV-Vis-NIR

frequencies loss mechanisms arise from phenomena related to conduction electrons (if any) and bound electrons (interband effects) .[8]

The dielectric function is a general expression that describes how any material from metals to semiconductors, interacts with EM waves. Figure 1.2 lists the values for metals, semiconductor and a dielectric (glass) at different frequencies.[9]

	Vis-NIR (400-800nm)	Infrared (0.8-30µm)	Radiofrequencies 1-10 GHz
Metals	$\varepsilon'<0$ $\varepsilon''\approx 0$	$\varepsilon'<-1$ $\varepsilon''>1$	$\varepsilon' \approx -\infty$ $\varepsilon'' \approx +\infty$
Semiconductors	$\varepsilon' \approx 10\text{-}16$ $\varepsilon''\approx 0\text{-}2$	$\varepsilon' \approx 11\text{-}16$ $\varepsilon'' \approx 0$	$\varepsilon' \approx 12\text{-}13$ $\varepsilon'' \approx 0.01\text{-}0.1$
Glass	$\varepsilon' \approx 2\text{-}2.3$ $\varepsilon''\approx 0$	$\varepsilon' \approx 2\text{-}2.3$ $\varepsilon'' \approx 0$	$\varepsilon' \approx 5\text{-}15$ $\varepsilon'' \approx 0$

Figure 1.2 Optical permittivity of different class of materials at different frequency ranges. Extracted from ref 9.

1.2.2 Materials for plasmonics

Metals are crystals and, in most of the cases, present a face centered cubic lattice with periodicity around 0.35-0.4 nm. This type of the lattice possesses one of the highest packing densities in nature and it explains why metals are so heavy. Metals are also good conductors; along bound electrons localized in the vicinity of atoms they also have free electrons the so-called free electron gas, that can propagate throughout the crystal. Usually each atom contributes with one electron but in some cases (Aluminum) can contribute with up to three electrons to the free electron gas. The response of metals to an external electromagnetic field is mainly defined by the electron gas density and it gives the main contribution to the permittivity. The Drude model is the simplest way to represent the free electron gas in a metal. However, it has several limitations based on the fact that electrons moving in a metal crystal lattice can dissipate energy upon collision with defects in the material. This effect is responsible for

the ohmic losses that are implemented into the Drude-Sommerfield model. It considers the permittivity as a complex function and is given by the following expression:

$$\varepsilon_{(\omega)} \approx \varepsilon_{\infty} - \frac{\omega_p^2}{\omega^2} + i\frac{\gamma_0 \omega_p^2}{\omega^3} \qquad (4)$$

where ε_{∞} accounts for the contribution of the bound electrons (interband transitions) and equals 1 when only free electrons from the conduction band contribute to the dielectric function, γ_0 is the inverse momentum relaxation time and is related to the collision rate, finally ω is the frequency of incident electromagnetic wave and $\omega_p = \sqrt{ne^2/\varepsilon_0 m_e}$ is the plasma frequency, n and m_e are the density and the effective mass of the conduction electrons respectively. It is interesting to note that the permittivity of the electron gas is a function of frequency and is completely defined by a single parameter, the plasma frequency.

If we neglect the contribution of bound electrons (that we will account for later) we can simplify both the real and imaginary part of the dielectric function and distinguish two cases: i) $\omega > \omega_P$ the dielectric function becomes positive and the refractive index of the material ($n = \sqrt{\varepsilon}$) assumes real values. Under this condition, the wave is allowed to propagate inside the medium. ii) $\omega < \omega_P$ the dielectric function turns negative and the related reflective index become complex. This means that the conduction electrons do not oscillate in phase with the external electromagnetic field leading to both high reflectivity and not negligible losses. Thus, from eq. (4) we have Re(ε)<0 and, if ω is not too small, the absorption, so the Im(ε), is also small in this region. Those latter situations are at the basis of interesting optical effects, including plasmon resonances. In general, these conditions in the visible and near infrared range are never fulfilled in standard dielectrics whose Re(ε) is typically between 1-10. For many metals, the plasma frequency falls in the UV region of the electromagnetic spectrum and the "allowed" frequencies are in visible (or close UV, near infrared, depending on the metal). Figure 1.3 summarizes the condition to achieve plasmonic effects:

$$\omega_p > \omega \qquad \omega \gg \gamma$$

$$\mathrm{Re}(\varepsilon) = 1 - \frac{\omega_p^2}{\omega^2} < 0 \qquad \mathrm{Im}(\varepsilon) \propto \frac{1}{\omega^3} \approx 0$$
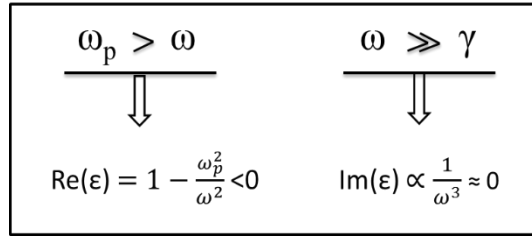
Figure 1.3. Conditions giving rise to plasmonic effects. The negative real part and small imaginary part of the permittivity is achieved when the operation frequency is both below the plasma frequency and large enough to dominate over collision frequency.

The plasma frequency and the damping term define a range of energies in which a material can be used for plasmonic applications. In the case of some noble metals such as Au and Cu the interband transition cannot be neglected in the visible since it induces further losses due to optical absorption and occurs when bound electrons absorb the photons energy and get excited to higher energy band. This effect limits the applications of materials to a specific frequency range and have to be taken into account when coming to the design of plasmonic devices. This loss manifests as an increase in the $\mathrm{Im}(\varepsilon)$ and is well described by the formalism of Lorentz oscillator model, or by more complex expression that takes into account the band-like nature of this transition.[10,11]

All these parameters contribute to define good candidates for plasmonic applications. In the next paragraph a brief survey of different noble metals will unveil the best materials to work at specific optical wavelengths.

1.2.3   Metals as plasmonic materials

At this point, we can highlight three main parameters: the damping rate (ohmic losses), the plasma frequency (electron cloud density), and the interband transition term (optical absorption). These parameters affect the optical properties of the metals and we need to find a material with low electromagnetic field penetration that neither dissipates energy in the form of heat nor absorbs photons for optical transition. These conditions are fulfilled by noble metals, such as Ag, Au or Cu. Each of them has a large negative real part of dielectric constant at optical wavelengths; however, they differ in the imaginary part.

- **Silver** has the smallest ohmic losses in the visible (due to small γ_0), and presents the first interband transition in the UV (above 3.1eV). It means that it is suitable for plasmonic applications in the higher energy part of the visible spectra.

- **Gold** is more chemically stable than silver but it presents higher losses (relatively higher γ_0) so the optimal frequency range shifts to the visible and near infrared. The interband transition at 2,3eV hinders the gold applicability below500nm(~2,3eV). This means that every plasmonic effect below this energy would be strongly damped. Regardless, gold is often used as plasmonic material in the VIS-NIR range.

- **Copper** shows an interband transition at ~2.1eV and cannot be used below 600nm. Considering the cost of silver and gold, copper would be a good and cheaper candidate for plasmonics if it was not for its low chemical stability against oxidation.

- **Aluminum** is an emerging material in optics and nanoplasmonics. As pointed out at the beginning of this chapter, aluminum atoms contribute to the free electron gas with three electrons per atoms leading to high electron density and consequently high plasma frequency. Because of this, the real part of the dielectric function is negative even at wavelengths smaller than 200nm where the losses are still relatively low. Thus, aluminum is a better plasmonic material that silver and gold in the blue and UV range, while in the visible and NIR range it is affected by the interband transition that falls at 1.4eV (~800nm). However, Al is prone to oxidation, affecting its optical properties.

Along with these considerations there are other very important practical issues such as the availability, easy of manipulation especially for nanofabrication, toxicity, durability, cost and finally chemical and physical stability. In this regards, Ag and Cu easily oxidize under ambient humidity condition, while Al passivates forming Al_2O_3 layers. These factors result in an increased imaginary part of the dielectric function and a concomitant increase of the optical losses. Gold instead is chemically stable against corrosion, and is easy to use in nanofabrication.

Silver and Gold are the most often used in plasmonic applications in the and VIS-NIR regions. Actually, the majority of high impact discoveries in plasmonics have been done using those noble metals. Silver and gold have been used to demonstrate negative refractive index materials in the visible and NIR[12,13], to improve photodetectors efficiency[14], to implement light-emitting diodes[15], to enhance optical spectroscopy and light emission[16,17] or to fabricate refractive index sensors.[18–20]

1.2.4 Plasmon resonance: the origin of light confinement

Modern plasmonics literature often refers to plasmon or plasmon resonances as follows: "*plasmon is a quantum quasi-particle representing the elementary excitation, or modes, of the charge density oscillations in a plasma*".[21] The analogy with photon and electromagnetic waves is quite straightforward however the main difference is the lossy behavior that affects plasmons. As a consequence, it means that if not maintained by an external source of energy, a plasmon will always decay because of various damping mechanisms. When an electromagnetic wave interacts with the free electron plasma the electron cloud gets excited and oscillates in response to the external electric field. The energy of such a wave is then shared between the external electromagnetic field oscillation and the internal excitation of electron cloud. Thus, the generated perturbation is no longer a photon nor a plasmon, rather it takes the names of plasmon-polariton.[22] These mixed photon-plasmon modes exist in a metal/dielectric interface. In plasmonics, the existence of surface plasmon polaritons gives rise to a plethora of effects studied in nanotechnology including all the exceptional light confinement mechanisms typical of plasmonic nano objects.

Surface plasmon polaritons can be divided into two types: localized surface plasmon-polaritons (LSPP) and Propagating surface plasmon-polaritons (PSPP). In both cases, at a specific resonance condition we can reach a maximum coupling between the incident electromagnetic wave and the free electron oscillation. There is a strict relation between the negative real part of the dielectric function with the existence of plasmon resonance. Let us consider

the simplest problem of a small metallic particle interacting with an electromagnetic field. If we keep the radius of the sphere much smaller than the incident wavelength, the spatial dependence of the electromagnetic field can be ignored; in other words we are in the quasi-static approximation regime.[23–25] A simple sketch of the possible regimes are represented in Figure 1.4.
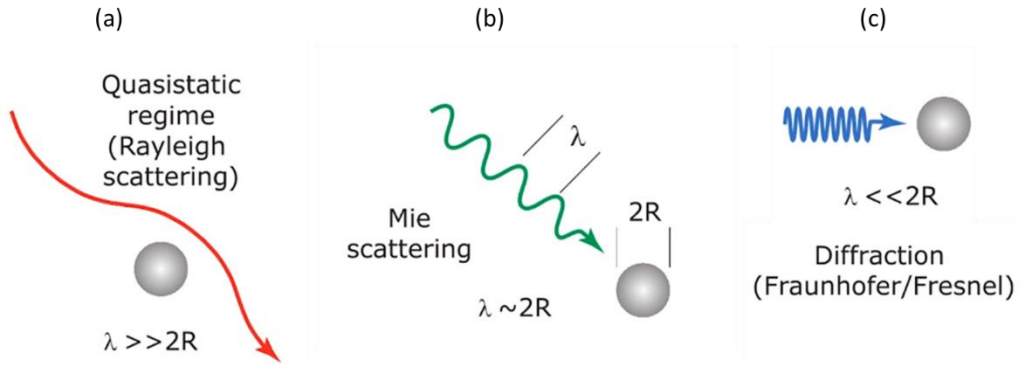
Figure 1.4. Simplified sketch of the three different regimes of interaction between nano objects and oscillating electromagnetic waves. a) quasistatic regime, the incident wavelength is much larger than the nanoparticles diameter. The whole is affected by the electric field oscillation and plasmonic effects arise. b) Mie scattering regime. The nanoparticle size is on the order of the incident wavelength only scattering of the incoming light is present. c) Diffraction regime. The wavelength is much smaller than the nanoparticles,

With this in mind the electric field inside the sphere can then be shown to be constant and proportional to the incident field E_0

$$E_{in} = \frac{3\varepsilon_m}{\varepsilon(\omega)+2\varepsilon_m} E_0 \qquad (5)$$

The important part in this expression is the denominator; as it comes to zero, the internal electric field becomes very large, even larger than the external field. While this condition is never fulfilled with standard dielectrics whose permittivity is comprised between 1 and 10, it is possible with metals in the visible and near infrared range where the absorption is small (Im(ε)≈0) and the electromagnetic wave is not allowed to propagate inside the material (Re(ε)<0). At these conditions the optical response is very large: this is a clear signature of a resonance. In general, the real part of the dielectric function determines the

resonance condition (wavelength) while the imaginary part limits how large and broad the resonance can be (intensity). Another important factor is the shape of the scatterers since different resonant conditions are a function of the geometry and configuration. This means that two objects made with the same metal but with different shape will have different resonance conditions.

In summary, we determined the conditions by which an external oscillating electric field can couple with surface plasmons in a metal. This resonant condition depends on the type of system that we are considering. In general, we refer to localized surface plasmon resonance (LSPR) when dealing with single nanoobjects, while the term propagating surface plasmon resonance (PSPR or simply SPR) is used to describe the propagating plasmon-polaritons existing in a planar metal/dielectric interface. In the following section we will briefly describe these two effects highlighting the coupling condition for SPR that will be used later in this thesis.

1.3 LOCALIZED SURFACE PLASMON RESONANCES

When an electromagnetic wave impinges on a nanometric metal object the electron cloud of the particle is entirely affected by the electric field. This implies the generation of a net charge separation that in turn creates a Coulombic restoring force as depicted in Figure 1.5; this implies an accumulation of charges alternately on opposite side of the particles, which induces an electric field with a $\pi/2$ phase lag compared to the excitation field. This phenomenon takes the name of Localized Surface Plasmon Resonance.[26,27]
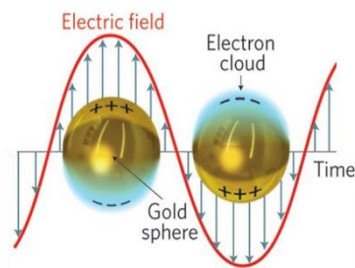
Figure 1.5 Schematic representation of the effect of an incoming electromagnetic wave on the electron cloud of spherical nanoparticles.

Localized surface plasmons can be defined as non-propagating excitation of the free electrons of metallic nanostructures coupled to the electromagnetic field. The optical response of these nanoparticles unveils a strong energy confinement. The energy involved in this process can both be dissipated in heat within the nanoparticles and/or re-irradiated into the free space. These two mechanisms describe the well-known optical features in a nanoparticle i.e. absorption and scattering. They describe LSPR from a more macroscopic point of view. Actually, its magnitude (experimentally or computationally estimated) gives us a tool to understand our plasmonic nanostructures.

Both scattering and absorption cross section σ_{scat} and σ_{abs} are determined by particle geometry and the intrinsic dielectric response of the metal.

$$\sigma_{abs} = kIm(\alpha) \quad \propto \quad 4\pi r Im\left(\frac{\varepsilon - \varepsilon_m}{\varepsilon + 2\varepsilon_m}\right) \qquad (6)$$

$$\sigma_{scat} = \frac{k^4}{6\pi}|\alpha^2| \quad \propto \quad \frac{8\pi}{3}r^4\left|\frac{\varepsilon - \varepsilon_m}{\varepsilon + 2\varepsilon_m}\right|^2 \qquad (7)$$

Where α is the polarizability, r the nanoparticle radius, ε and ε_m the metal and medium dielectric functions. Both σ_{abs} and σ_{scatt} depend on the particle size even though they scale differently. The contribution of scattering increases for larger particles, while for smaller particles the energy losses can be predominately ascribed to heat dissipation. In experimental optical characterization however is not trivial to separate these two contributions. The actual optical outcome from spectroscopic analysis is considered a sum of scattering and absorption cross section and is called extinction efficiency. For particles of larger dimension, the quasi static approximation breaks down due to retardation effects and the spatial variation of the exciting electromagnetic field can no longer be neglected. In this case, more rigorous approach is required and the solution of the scattering cross section is basically a power series expansion with higher order terms corresponding to the higher modes. Such multimodes (e.g. quadrupoles, octopoles) are always located at shorter wavelengths (higher energy) compared to the dipolar excitation.

Another key feature of localized surface plasmon polaritons is their dependence on the nanoparticle shape. A modification of the nanoparticle geometry has a significant impact on the spectral position of the plasmon resonance since it entails an adjustment of the denominator of the eq. (5), defining then different resonance conditions. Spherical nanoparticles with high symmetry only possess one dipolar resonance, but when the shape is modified and the particles become more asymmetric, multiple dipolar modes can arise which makes the optical response more complex[28]. For instance, elongated metal nanoparticles like nanorods display both a transverse and a longitudinal localized surface plasmon mode which gives rise to two distinct plasmon resonance peaks at different spectral positions. Several other geometrical features in addition to elongation, affect the actual plasmon frequency such as curvature, asymmetry and intracoupling[26,27]. Furthermore, higher-order plasmon modes can be created due to an inhomogeneous distribution of the surface charges in the nanoparticles[29]. Consequently, by varying the size and/or shape of the nanoparticles, plasmon peaks can be tuned over the entire visible and near-infrared region.

1.4 PROPAGATING SURFACE PLASMON RESONANCES.

Propagating Surface Plasmon Resonances (PSPR) are electromagnetic excitations of free electrons that propagate in a wave like fashion along the interface between a metal and dielectric. Its amplitude decays exponentially from the interface into both media and it is strictly correlated with the optical properties of the metal and the dielectric materials.[30] In order to understand how to excite these resonances it is useful to derive the dispersion relation between wave vectors and frequency that can be obtained by solving Maxwell's equation with the appropriate boundary conditions. This solution gives us the permitted wave vectors along the surface and can be written as follows:

$$k_{||} = k_0 \sqrt{\frac{\varepsilon_m \varepsilon_d}{\varepsilon_m + \varepsilon_d}} \qquad (8)$$

$$k_0 = \frac{2\pi}{\lambda_0} = \frac{\omega}{c} \qquad\qquad (9)$$

Where $k_{\parallel}$ is the momentum wavevector parallel to the surface and k_0 the one from photons in vacuum, at a given λ_0. In Figure 1.6 the red and blue lines show the solution of the dispersion relation at metal/dielectric interface.
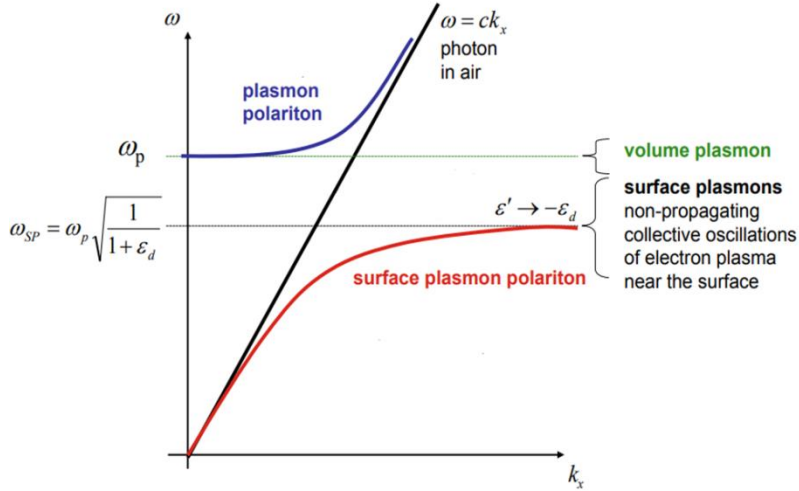
Figure 1.6 Dispersion relations of surface plasmon polaritons highlighting the both plasma and surface polaritons frequency. The dispersion in blue represent the Brewster condition while the red line is the dispersion of surface plasmon polaritons confined at the metal/dielectric interface.

The upper branch (blue line) does not correspond to a surface wave. In this part of the diagram there are only propagating waves inside both media without no exponential decays: it corresponds to a frequency higher than the plasma frequency of the metal ($Re(\varepsilon)>0$). The lower branch (red line) represents the dispersion of surface plasmon-polariton and corresponds to a bound surface wave with exponential decay inside both media. It is clear that this wave can propagate at arbitrary low energies so we can study it not only in the visible and near infrared region but also in the far infrared or even at terahertz frequencies. On the other hand, the dispersion relation shows that the wavevector of surface plasmon polaritons tends to infinite at some frequency and this frequency is called resonant frequency of surface plasmon-polariton. This condition is fulfilled when the denominator of the eq. 8 is equal to zero

namely when the sum of the permittivity of the metal and dielectric is equal to zero (in analogy with the condition described above for localized surface plasmon resonances). In between the two branches the parallel wavevector is pure imaginary. The corresponding surface wave does not propagate at all and dissipates into the two media and away from the surface.

Upon the excitation of surface plasmon polaritons, transverse and longitudinal electromagnetic field propagates along the plane and the maximum intensity is present at the interface. Beyond and away from it, the field exhibits near-field or evanescent behavior with exponential decay from the interface. Furthermore, depending at which wavelenghts we are exciting SPPs we can end-up with more propagating or more localized waves. At low frequency, the dispersion curve is quite close to the light line so the field penetrate inside the dilectric media much deeper than in the metal, and the localization of surface plasmon polaritons is consequently weak. On the other hand, in vicinity of the resonant frequency ω_{sp} the penetration depth inside the metal and dilectric becomes the same so our surface plasmon polaritons become more and more localized (Figure 1.7). In summary, the exitation of SPPs gives then the possibility to confine electromagnetic waves beyond diffraction limit and paves the way for litgh management at the nanoscale.
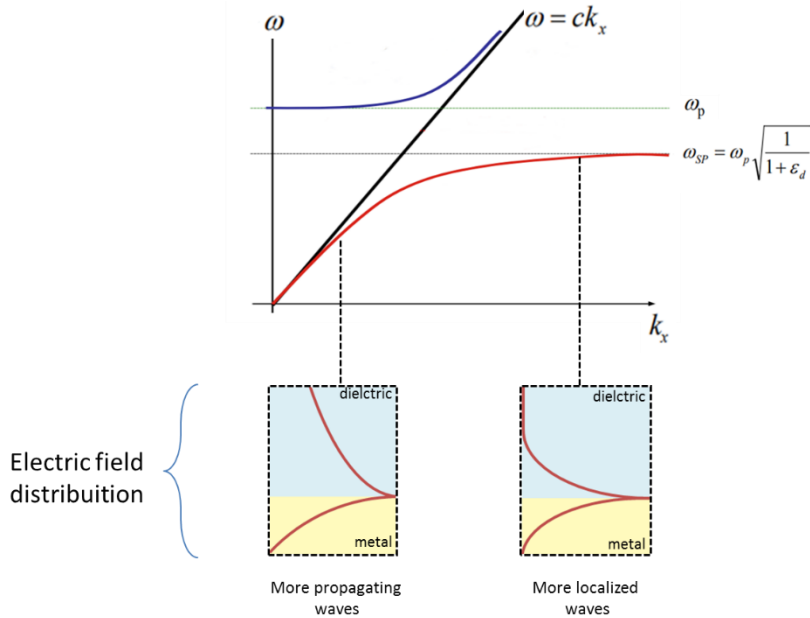
Figure 1.7 Dispersion relations of surface plasmon polaritons highlighting the electric field distribution of surface wave inside the dielectric and metals depending on the frequency and k.

Assuming the realistic scenario of a dielectric medium with a negligible absorption and a noble metal counterpart that has large negative real part of the dielectric constant, we thus obtain a good system that can sustain long lived SPP at optical wavelengths. This interesting feature could be used in sensing when we need to detect a very thin layer of analyte placed on the metal surface.

In the discussion above we determined the condition to achieve surface plasmon polaritons and demonstrate their bound nature at the interface. However, in this discussion we have neglected any associated losses. As thoroughly discussed in the previous paragraph, losses in metals are described by the imaginary part of the permittivity and determine the intensity of the resonance. When dealing with surface plasmon polaritons, every dissipating mechanism not only damps the oscillation but affects the propagation length of the electromagnetic wave along the surface.

The main consequence of not negligible absorption is that the dispersion relation no longer diverges for $\varepsilon_m = -\varepsilon_d$, and it is actually back bending in the

19

region of localized SPPs as depicted in Figure 1.8. This anomalous dispersion has been observed experimentally for the first time by Arakawa et.al.[31,32]
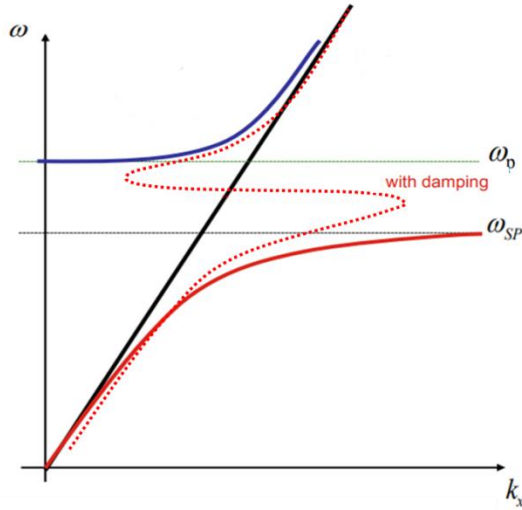
Figure 1.8 Dispersion relations of surface plasmon polaritons highlighting the out coupling with the free space possible due to losses of the material

When absorption is neglected, the surface wave associated with PSPP modes can propagate infinitely along the parallel direction, once losses are included ($Im(\varepsilon)>0$), the surface wave is damped by absorption in the metal and the field intensity decays exponentially. This defines a propagation length for surface plasmon polaritons that can be expressed as follows:

$$L_{SPP} = \frac{1}{2Im(k_{||})} \qquad (10)$$

This propagation length can be much larger than the wavelength if ε'' is sufficiently small and $|\varepsilon'(\omega)|$ is large, i.e. at longer wavelengths for metals. In the case of gold and silver they present similar values at λ>600nm, where the interband transitions no longer play a role. That length is in the order ~10-100µm for both silver and gold in the visible and can be as large as 0.3 mm in the near infrared (λ≈1.5µm).

In summary, the dispersion relation not only lets us to identify the conditions to achieve propagating SPPs but also gives insight on the bound nature of such

waves. These PSPP modes are therefore truly trapped electromagnetic surface wave that can be launched with incoming light.

- *Exciting surface plasmon polaritons*

We have described the dispersion relation of a SPP highlighting its frequency dependent properties. However a SPP wave vector is always larger than the wave vector of photons in air, resulting in a momentum mismatch that has to be overcome somehow.[33] In order to excite a surface plasmon polariton we need to provide an additional in plane momentum. Conversely is impossible to provide momentum conservation with light incident form the free space.

Many methods of SPPs excitation have been developed so far, the most commons are summarized in Figure 1.9 and can be sorted depending their mechanisms.[34]
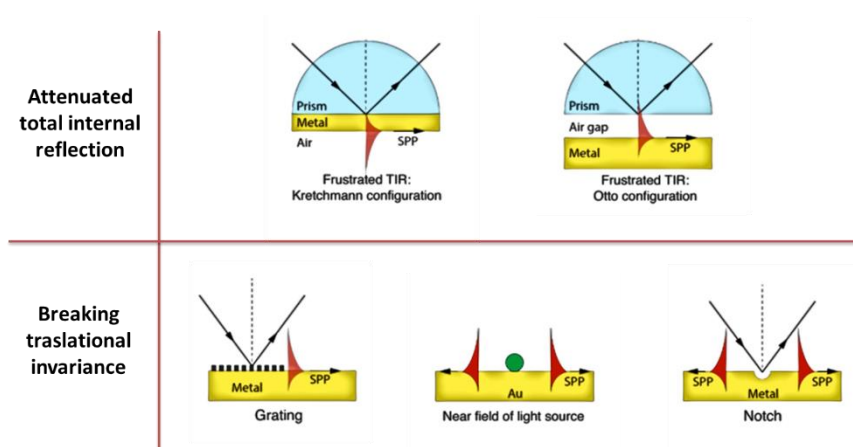
Figure 1.9. Sketch of different SPPs excitation setups based both in attenuated total reflection and on the breaking of translational invariance

Along all of them Kretschmann configuration system, whose setup and mechanism is illustrated in figure 1.10, is the most common ATR coupling method.[35] In this setup, a thin layer of metal is deposited on the surface of the prism and a light beam is shined thought the prism on the glass-metal interface. The greater refractive index of the prism provides an increased wavevector from light in air. A scheme of the mechanism of this method is illustrated in fugue 10.
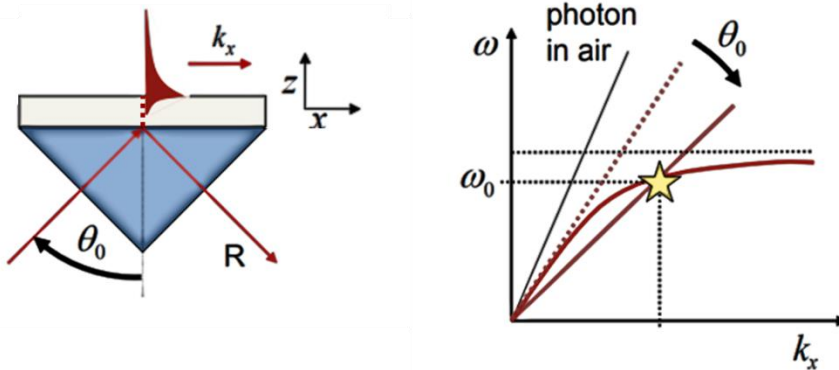
Figure 1.10 Kretschmann configuration for the excitation of surface plasmon polaritons, and (b) Dispersion relation of a surface plasmon and visualization of the momentum matching.

When the angles of the incident light are greater than the critical angle of total internal reflection, the photons can tunnel through the metal film and excite SPPs at the metal/air interface. One of the requirements for this method is that the thickness of metal layer must be thin enough to allow tunneling of photons. The key point of this method relies on the fact that the prism has a refractive index grater that the air, as a result the refracted light will have an extra momentum provided by the prism. Actually, a photon that propagates in a dielectric media at a frequency ω, will show increased wavevector than the same propagating in air. In this way we can reach condition where k of photons equals the k of surface plasmon with straightforward consequence of that the surface plasmon polaritons can be excited.

Even though the latter method is very efficient in coupling light with surface plasmon polaritons, it lacks of versatility. On the other hand, grating coupling methods present a good alternative. They allow good control over the properties of surface plasmon polaritons and broaden the possible applications that are no longer restricted to sensing.

1.5 PLASMONIC-PHOTONICS HYBRID MATERIALS

1.5.1 Insight on light confinement in photonic crystals

Photonic crystals (PC) are materials whose dielectric constant shows a periodical modulation in one, two or three dimensions.[36,37] If the lattice constant is in the order of the wavelength of the incident light, then the wave propagates into those crystals in the same way by which electrons move in the periodic potential of atoms in a lattice.[38]

In most cases, 2D photonic crystal slabs are used for the ease of fabrication and for the outstanding results that can be obtained in terms of light confinement and manipulation of guided modes.[39] 2D PCs slab are the most widespread configuration to confine electromagnetic field on a dielectric material. The system relies on the effect that such corrugation has onto the incoming wavevector. Actually, the periodic grating adds the extra momentum needed for the coupling between the light cone and guided modes by adding a reciprocal lattice vector to the incident wave-vector, as depicted in Figure 1.11.
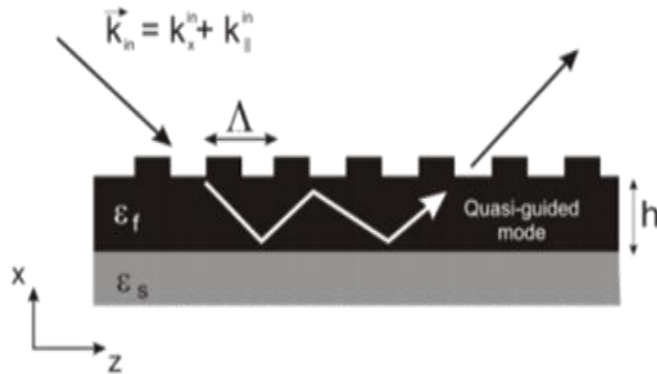
Figure 1.11 Diagram of guided mode coupling/decoupling in a grating topped slab waveguide.

We can express the coupling condition for a square grating of period coupled to the slab

$$k_{||} = k_{||}^{in} \pm m|G| \qquad (11)$$

where $k_{||}^{in}$ is the parallel component of the incident wavevector. G is the reciprocal lattice vector along the same direction as $k_{||}^{in}$ and takes values $|G| = 2\pi/d$ where d is the periodicity of the grating.[24] The direct consequence of this coupling is that the original guided modes are no longer totally confined but loose some energy through radiation to free space during the propagation. These new modes are called leaky modes or quasi-guided modes and present a finite lifetime that is determined by the efficiency of light coupling/decoupling by the periodic structure to the slab. The parameter that measures how long a mode propagates before leaking out the structure is the quality factor (Q). From the application point of view, a good quality factor is advantageous for strong light matter interactions that will be useful in many applications such solid state lasing.[40] In other cases, the efficient out coupling will help to radiate to the free space emitted light form molecular dyes or enhance the intensity of light scattered from a molecule (e.g. Raman scattering)

1.5.2   Plasmonic crystal structures to excite SPP

We now come to unveil the mechanism of coupling of surface plasmon polaritons with light from the free space using photonic crystals.

Photonic crystals can serve to efficiently couple the incident light to surface plasmon polaritons. The key concept of this effect is the same of wave guided modes coupling through grating periodicity described before. The difference in this case is that the added extra momentum leads to the excitation of propagating coherent electron oscillation on the interface of a metal and a dielectric. The coupling condition depends on the grating constant (L) but now involves the dispersion relation of surface plasmon polaritons. Equation 12 shows the momentum matching condition that must be satisfied to efficiently launch an in-plane surface plasmon-polariton.

$$K_{SPP} = \frac{\omega}{c}\sqrt{\frac{\varepsilon_m \varepsilon_d}{\varepsilon_m + \varepsilon_d}} = k_0 sin\theta_{SPR} \pm m\frac{2\pi}{L} \qquad (12)$$

Let us consider an incident wave at angle θ on the metallic grating where $k_0 sin\theta_{SPR}$ is the in-plane wave vector of the incident beam. The grating provides an additional in plane momentum to the incident photons which is equal to the integer number of the reciprocal lattice vector ±m(2π/L), (Figure 1.12).
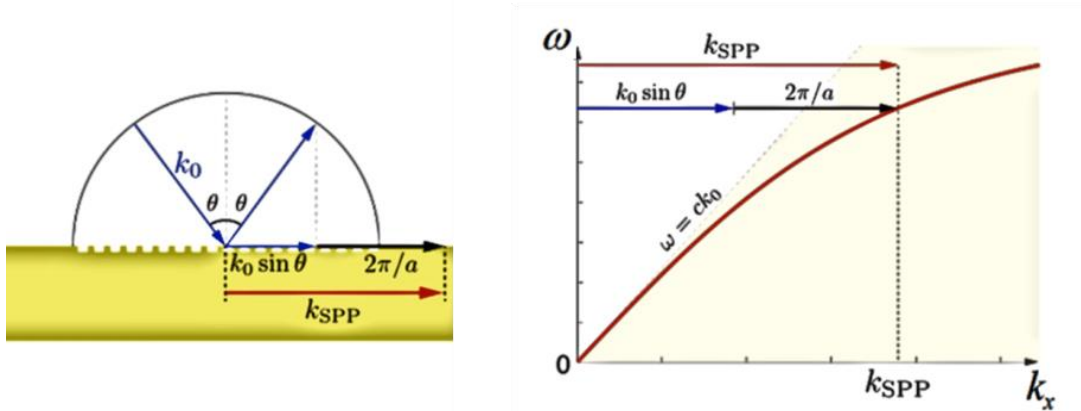
Figure 1.12. Excitation of SPP with a grating. Surface plasmon polaritons can be excited though interaction with diffracted light form the grating. This can be visually appreciated on the dispersion relation as an increment of the parallel wavevector that reaches the surface plasmon polariton curve.

The excitation of an SPP on a metallic grating manifests itsefg as dip in the reflection spectra. This was first observed by Wood in 1902 and were commonly referred as wood's anomalies.[1] In 1941 when Ugo Fano gave the first theoretical demonstration of this phenomenon.[41]

As a better understanding of SPR was obtained, several application of this light confinement method emerged. In the following chapters we present the state of the art of plasmonic system highlighting the exciting versatility of these systems.

1.6   APPLICATION OF PLASMONICS AND HYBRID SYSTEMS

The manipulation of light at nanoscale volumes leads to a large number of applications ranging from light generation, light harvesting[42], data storage[43] as well as environmental and medical sensing.[44] In this framework, hybrid

plasmonic-photonic nanostructures take advantage of the combination of the locally enhanced electromagnetic fields and the engineered diffractive effects for periodic lattice geometries. This combination enables the reduction of ohmic and radiative loss of plasmon antennas that hybridize to form surface lattice resonances.[45] It is actually this merger between subwavelength confinement of electric field and high quality factor of lattice resonances that makes these architectures a fundamental tool in plasmonics for applications ranging from refractive index sensing,[46,47] to Raman spectroscopy,[48] to fluorescence enhancement in solid state lighting context[49] or collective strong coupling.[28] Furthermore, the intrinsically two-dimensional nature of SPPs provides a significant flexibility in the engineering SPP based all-optical integrated circuits used in optical communication and computing.[50,51]

1.6.1 State of the art: from energy to medicine

Custom-designed nanostructures induce strong modification of light emission kinetics in luminescent materials. The light emission can be suitably controlled for increased emission efficiency, spatial manipulation (for localization), angular distribution (for directionality), polarization (for anisotropy), spectral linewidth (for quality), etc. In this context emission kinetics can be modified by exciton-plasmon coupling where metallic nanostructures provide localized plasmons with resonances determined by the material shape and size and act as optical nanoantennas in close proximity of the emitters. Thus, strongly coupled exciton-photon systems can radically change the emission properties.[52,53] Within the current nanofabrication techniques various coupled nanosystems have been demonstrated where the emitter decay rate has increased over 20 times, the intensity enhanced up to 1000 times and the emission directed into narrow cones.[54]

Nanostructured surfaces are equally good for efficient light trapping. In photovoltaics, the light shall be absorbed in the active layer and then converted into electrical current. In these systems a thin active layer is preferred to achieve better charge separation; however, the light harvesting efficiency drops dramatically. Plasmonic nanostructures offer a good way to increase the

absorbance, especially in thin film solar cells. For example nanoparticles can act as sub-wavelength scatterers or resonant antennas to trap and couple the incident light to the thin photovoltaic layer.[55] Alternatively a nanocorrugated metallic film at the back surface of solar cell can effectively convert light into surface plasmons coupled to the photovoltaic layer.[56] Furthermore it is interesting to highlight that metallic nanostructures can also be used as electrodes to collect photocurrent.[42] The application of metallic plasmonic structures in solar cells has developed at a tremendously high pace, especially because it allows to shrink down the active layer below 100nm, providing physically thin but optically thick photovoltaic absorbers.[57] However, important aspects such as finding the optimal geometry using inexpensive metals and issues with large-scale fabrication have hindered the potential commercial applications. Along with photovoltaics, photo catalysis and sensing grew exponentially in the last decades exploiting this merger of plasmonics with chemistry as well as with biology and medicine.[58]

The rich pool of plasmon modes further opens the way for applications in SERS spectroscopy,[59,60] spontaneous emission and photoluminescence enhancement,[61] as well as in photocatalysis and nanochemistry.[62] However has to been pointed out that while most of the studies rely on plasmonic nanocavities formed by single nanoparticles coupled to a film, the studies about complex nanostructures such as dimers, trimers and array of particles are currently under investigation because they are expected to offer richer resonances and more freedoms to tailor their optical properties.[63,64]

In this work, we will fabricate and characterize such complex structures applying their unique optical properties in SERS sensing and photoluminescence enhancement. In short, these two techniques consist in using the large local field enhancement that can exist at metallic surfaces to boost the Raman scattering or fluorescence of molecules placed at (or close to) the surface. From both a fundamental and an applied point of view, one of the most important aspects of the technique is to know by how much the signal can be boosted, in other words to quantify the enhancement factor (EF) and unveil its physical origin.

In the rest of this chapter both surface enhanced fluorescence and surface enhanced Raman scattering are introduced and the basic mechanism of the plasmonic enhancement will be discussed.

1.6.2   Surface enhanced fluorescence

The term fluorescence refers to the emission of electromagnetic radiation produced by the excitation of electrons in a material reemited almost immediately, (within about 10^{-8} seconds). The initial excitation is usually caused by absorption of incident radiation. The fluorescence reemission occurs so quickly that it stops as soon as the exciting source is removed, unlike phosphorescence, which persists for a longer time.[65] Figure 1.13 describe the energy transitions involved in fluorescence by Jablonsky diagrams.[66]
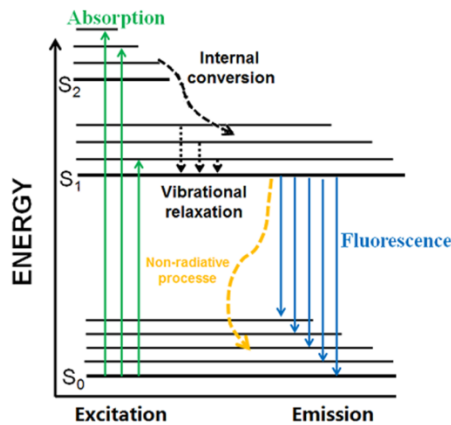
Figure 1.13 Jablonski diagram for typical excitation, emission and thermal relaxation in a quantum system. Adapted from ref. 66.

The efficiency of a fluorophore to convert energy into photons instead of relaxing by non-radiative processes is quantified by the quantum efficiency (*QE*). It represents a fundamental parameter used to characterize those systems and reflects the quality of a fluorophore.

$$QE = \frac{\Gamma_{EM}}{\Gamma_{EM} + \Gamma_{NR}} = \frac{\tau}{\tau_{EM}} \qquad (13)$$

Where Γ_{EM} represents all the relaxation processes and Γ_{NR} is related to non-radiative processes, normally induced by direct molecular interaction (collisions), in general energy is dissipated to the surrounding media in the form of heat. Fluorescence is a spontaneous emission process and its relaxation rate is determined by its electromagnetic environment. For a two-level system, at the transition frequency ω, the spontaneous emission rate ($\Gamma_{(r)}$) is proportional to number of available final photon states (DOS) and to the type of electronic transitions. The emission rate is governed by the Fermi golden rule and is expressed as follows:

$$\Gamma_{(\omega)} = \frac{2\pi}{\hbar}\left|M_{if}\right|^2 \rho(\omega) \qquad (14)$$

$\rho(\omega)$ is the density of states and M_{if} the matrix interaction. The density of states describes the number of states that are available to be occupied by the system at each level of energy while the matrix interaction defines the strength of a quantum transition which depends on the systems selection rules. These two terms respectively determine the energy and the intensity of emitted photons.

Surface enhanced fluorescence relies on the coupling of a fluorophore with the highly confined field of surface plasmon polaritons. This interaction can be engineered to enhance the emitted light enabling improved detection limits and shorter analysis time. The coupling between plasmon and fluorophores can happen at its absorption and/or emission wavelengths; thus altering the transitions between the ground state and the higher exited states and vice versa.[67]

The fluorophores have long lived exited states in the order of nanoseconds and radiate strongly after thermal relaxation, while the plasmon relaxes almost instantaneously. The energy transfer between plasmon and fluorophores is dominated by dipole-dipole interactions and is determined by their separation distance. When the separation is below 10 nm, the non-radiative field of the dipole can excite the surrounding ones, a phenomenon that is known as Föster Resonance Energy Transfer, and has an efficiency given by:

$$Eff_{FRET} = \frac{1}{1+\left(\frac{R}{R_0}\right)^6} \qquad (15)$$

Where R is the separation distance and R_0 a factor that depends on the spectral overlap between the donor's excited state and the acceptor's ground state absorption.

The second possibility is to alter the emission rate through the Purcell effect[68]. If a radiative dipole is placed within a resonant cavity, the emission intensity is amplified on-resonance and quenched off-resonance because the cavity modifies the density of state (DOS). Furthermore, the available resonant modes have to be weighted by how well the dipole orientation and position of the emitter match to the one of the cavity resonances. Thus, it is important to introduce a more precise definition of density of states taking into account its spatially dependent behavior. In this case we use the local radiative density of states (LDOS) that is expressed as follows:

$$\rho_{LODS}(\omega) \sim |E_{loc}(\omega)|^2 \qquad (16)$$

where $|E_{loc}(\omega)|^2$ is the local electric field of the cavity normalized to the incoming intensity. The overlap between the plasmon and the fluorophore optical properties determines which of the two effects is actually predominant and whether it leads to enhancement or quenching of the signal.

In this thesis we use periodic metal nanostructures, plasmonic crystals, which induce strong spatial variation of EM field and allow the control of optical modes and consequent modification of the local radiative density of states. The emitter can couple with propagating surface plasmon polaritons at the resonant frequency through near-field coupling which provide wavevector large enough to excite SPPs. The energy flows from the emitters to the surface plasmon generating surface waves (PSPP) that are strictly bound to the metal-dielectric interface and hence are usually non-radiative. Intuitively this process decrees the efficiency of the radiative emission. However, the not negligible diffraction at the operation wavelength provides a channel to fold back the surface plasmon dispersion into the free space in the same way it helps to perform the

opposite process of coupling of light into surface plasmon as seen in previous discussions. In this way we do not only recover part of the emitted light that would have never reached the far field but also impose directionality thanks to the geometrical configuration of our plasmonic crystals.

In this thesis, Chapter 3 will be devoted on the description of a new class of asymmetric plasmonic crystals fabricated with unconventional nanolithography. Along with the polarization dependent optical properties and multiple possible application of the above mentioned plasmonic crystals, special attention will be given to nanogaps arrays and their potential as surface enhanced fluoresce systems. Intense fluorescence spectral shaping and enhancement will be demonstrated highlighting the possibility to control polarization of emitted light.

1.6.3   Surface enhanced Raman spectroscopy

- *Introduction to Raman scattering*

Raman spectroscopy is an inelastic light scattering technique that provides a vibrational fingerprint of molecules. It was first observed in 1928 by C.V. Raman who demonstrated that when photons collide with a molecule, two types of scattering occur: elastic scattering known as Rayleigh scattering and inelastic scattering known as Raman scattering. The inelastic scattering provides information about the molecular structure thanks to the interaction with vibrational modes of the molecules. When an electromagnetic wave interacts with the electron cloud of a molecule it can induce a dipole moment. The dipole moment intensity is ruled by the polarizability,[69] that can be considered as the "deformability" of the electron cloud when an external electric field is applied,[70]

The mechanism of Raman scattering can be easily visualized using Jablonski diagrams, which are depicted in Figure 1.14. Raman signals derive from an inelastic scattering phenomenon; therefore the scattered photons can have lower or higher energies compared the incident ones, giving rise to Stokes and anti-Stokes Raman signals, respectively.[71] The information that emerges from

the Raman signal is directly related with vibrational, rotational and other low frequency modes exhibited by a molecule. Raman scattering is defined as a form of molecular spectroscopy, predominately depicting molecule vibration therefore providing a molecular fingerprint. It is important to remark that this technique is different from standard infrared (IR) spectroscopy where the outcome is given by the absorption and not by scattering, i.e. the selection rules of the two techniques are different, meaning that an IR-allowed transition is not necessarily allowed in Raman.[72]
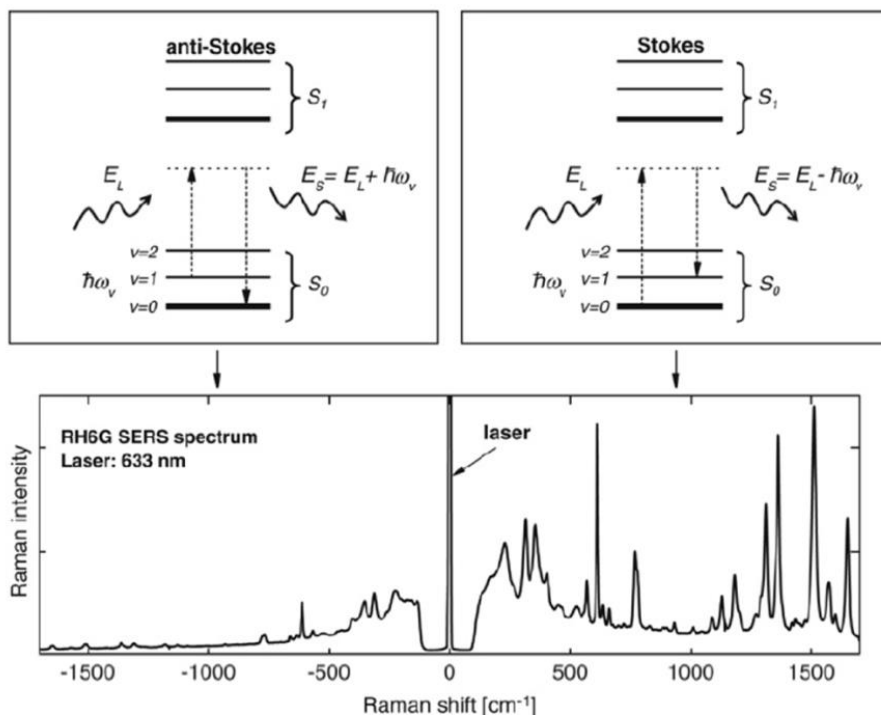
Figure 1.14 Simplified Jablonski diagrams of anti-Stokes (a) and Stokes (b) Raman processes. The Stokes process starts with the molecule in v= 0 vibrational ground state of S0 and ends in v =1, thus producing a scattered photon with a lower energy than the incoming one; on the other hand anti-Stokes scattering starts with the molecule already in the v = 1 vibrational excited state of S0 and ends in v = 0, thus producing a scattered photon with an energy larger than the incoming one. c) A typical Raman (in fact SERS here) spectrum for rhodamine 6G with several Raman scattering peaks on the Stokes side and their (weaker) anti-Stokes counterparts. Reprinted from ref 55.

- *Boosting the Raman signal*

The issues with Raman scattering and the reason why it remained in the shadow for roughly fifty years after its discovery in 1921, is due to the low probability of inelastic scattering, to give the idea, the general cross-section (i.e., the area of the incident beam over which incident photons are effectively converted into Raman signal) for this technique is between 10^{-31} and 10^{-29} cm^2/molecule which is 12-14 orders of magnitude below fluorescence cross sections. This cross section can be enhanced if more photons hit the molecules, hence, the higher number of collisions increases the scattered photons so the signal intensity. The first report on what years later would have become one of the most used analytical techniques is dated back to 1974, when Fleischmann and co-workers accidentally discovered the increased Raman scattering of pyridine absorbed on rough silver electrode. They reported Raman signal values orders of magnitude higher than those reported in liquid.[73] They initially explained the enhancement as a surface-area effect, while only three years later, Creighton and Albrecht clarified the degree of Raman signal enhancement in the pyridine-on-silver system and proposed an enhancement mechanism based on the chemical nature of the analyte. The acronym Surface Enhanced Raman Scattering (SERS) were coined on November 1977 by Richard van Duyne. He proposed a first and still recognized electromagnetic enhancement mechanism which add to the chemical mechanism. The connection of SERS effect with the enhanced electric fields arising from localized surface plasmons in nanostructured metals was demonstrated[74] one year later by Moskovits who paved the way for modern plasmonic device developments.

In summary the SERS enhancement can be separated into two main multiplicative contributions i.e. the electromagnetic enhancement and the chemical enhancement.

- The chemical mechanism is responsible for Raman signal enhancement up to 10^{3}.[75] It is defined as the effect due to the modification of Raman polarizability tensor upon adsorption of the molecule onto the surface.[71] This effect arises from two contributions: intrinsic properties of the molecule, and/or the interaction of the molecule with the substrate. In the first case the probed analyte shows by itself a higher Raman cross-section; these are the

so-called Raman dyes, typically molecules characterized by extended conjugation of π electrons. The second case occurs through a charge-transfer mechanism that can follow two main mechanisms. i) Metal in close proximity to the molecule causes a mild change of the molecule's electronic structure; thus, affecting its polarizability ii) The molecule forms of a new surface complex with the metal which alters its original polarizability. When the chemical enhancement contributes significantly to the final SERS intensity (typically with an extra EF of 10^1 - 10^3), we speak about SERRS, that stands for Surface Enhanced Resonant Raman Scattering.[76]

- The electromagnetic mechanism is responsible for Raman signal enhancement up to 10^8. This enhancement relies on the interaction on analytes with plasmon resonances in metal nanoparticles which concentrate and increase the electric field intensity of an incoming electromagnetic wave. When the resonant conditions are fulfilled (the denominator of the eq.5 is close to zero) the induced electric field will be much larger than the exciting one.[77] This means physically that a molecule located in the proximity of a plasmonic nanoparticle whose plasmon is being excited, experiences a much higher electric field, which is translated into a higher Raman scattering signal. In particular, SERS intensity can be written as

$$I_{SERS} = \alpha^2 \, |E_{in}(\omega_{in})|^2 \, |E_{out}(\omega_{in} - \omega_{vib})|^2 \qquad (17)$$

where α is the molecule polarizability, $|E_{in}(\omega_{in})|^2$ is the incoming electric filed intensity at the exiting energy ω_{in} while $|E_{out}(\omega_{in} - \omega_{vib})|^2$ is the scattered electric field intensity generated by the interaction with the molecule. Since the frequencies of the two electromagnetic waves are more or less the same (unless in the NIR and IR region) this formula can be approximated as follows:

$$I_{SERS} = \alpha^2 \, |E_{in}(\omega_{in})|^4 \qquad (18)$$

It means that if we have a 100-fold plasmonic electric field enhancement it will translate to a 10^8 time enhancement of the Raman scattering signal. The SERS

enhancement factor (EF) is the main figure of merit that quantify this enhancement and is expressed as follows:

$$EF = \frac{\frac{I_{SERS}}{N_{SERS}}}{\frac{I_{Raman}}{N_{Raman}}}$$

Where I_{SERS} and I_{Raman} are the integrated intensities of the SERS and normal Raman scattering spectra respectively: N_{SERS} and N_{Raman} are the number of probed molecules in SERS and normal Raman experiments, respectively. It should be stressed that a precise evaluation of the EF is extremely difficult for SERS substrates since a detailed estimation should involve a reliable count of the number of molecules adsorbed on the surface within the area probed. Another not negligible restriction is imposed by the nature of surface plasmon that is an electromagnetic oscillation strictly bounded to the metal/dielectric interface that decay exponentially away from the surface (Figure 1.7). It means that only the fraction of molecules bound or in close vicinity to the metal surface will contribute to the enhancement factor. The impressive field enhancement due to plasmon resonance can leads to EF large as ~10^5–10^8.[78,79]

- *Plasmonic hot spots in SERS*

The electromagnetic enhancement achieved with plasmonic nanostructures can be further improved through plasmon coupling. When two particles are sufficiently close to each other, their plasmon modes can interfere and create hybrid resonances along with an extreme EM field enhancement localized in the gap between the nanoparticles. This gap takes the name of hotspot and is demonstrated to be crucial to achieve maximum SERS enhancements.[80] The plasmonic absorption for dimers exhibits a new band at longer wavelength (red shift) due to interparticle plasmonic coupling.[81] This effect have been experimentally demonstrated decreasing the nanoparticles distance from 2.5 to 0.5 nm. For smaller gaps the maximum field enhancement in the gap becomes nearly 10 times larger and aggregation causes a large red shift of the Raman signal of more than 200 nm. Classical electrodynamics provides a good description of hotspots when the NP distance do not go below 1nm, after this limit, quantum and non-local effects are no longer negligible. In principle, EM

field intensity continues to increase until the distance between two metal surfaces becomes small enough that electrons spill-out, leading to electronic tunneling.[82]

The enhancements however will be highly localized in the gap. This means that only the portion of molecules placed in the hotspot will take advantage of the high EM field enhancement. Remarkably, it has been demonstrated experimentally that 63 out of 1 million molecules located in the hot-spots contribute to 24% of the overall SERS signal, while 61% of the 1 million molecules that are located in low electric field positions contribute just 4%.[83] Overall, metal plasmonic substrates can provide SERS EFs in the range of 10^3 - 10^8 and up to $10^{10} – 10^{11}$ for hot spots.[71]

1.7   CONCLUSIONS

Along this chapter, a short introduction on the physics behind the optical response of plasmonic nanostructures has been given. We have provided to the reader the basic principle to understand the phenomena treated in this thesis and the reason why metals and theirs nanostructuration is important for the development of novel plasmonics-photonic hybrid system.

The application and state of the art is described focusing the attention toward to new spectroscopic techniques used in this work namely Surface enhanced Raman scattering and surface enhanced fluorescence.

In the next chapter we explore the world of nanofabrication unveiling how novel approaches will enable the large scale and high throughput fabrication of plasmonic devices.

1.8   REFERENCES

(1)   Wood, R. W. On a Remarkable Case of Uneven Distribution of Light in a Diffraction Grating Spectrum. *London, Edinburgh, Dublin Philos. Mag. J. Sci.* **1902**, *4*, 396–402.

(2)   Schlather, A. E.; Gieri, P.; Robinson, M.; Centeno, S. A.; Manjavacas, A. Nineteenth-Century Nanotechnology: The Plasmonic Properties of Daguerreotypes. *Proc. Natl. Acad. Sci. U. S. A.* **2019**, *116*, 13791–13798.

(3)   Halas, N. J. Plasmonics Sheds Light on the Nanotechnology of Daguerreotypes. *Proc. Natl. Acad. Sci. U. S. A.* **2019**, *116*, 13724–13726.

(4)   Burgos, S. P.; Yokogawa, S.; Atwater, H. A. Color Imaging *via* Nearest Neighbor Hole Coupling in Plasmonic Color Filters Integrated onto a Complementary Metal-Oxide Semiconductor Image Sensor. *ACS Nano* **2013**, *7*, 10038–10047.

(5)   Aubry, A.; Lei, D. Y.; Fernández-Domínguez, A. I.; Sonnefraud, Y.; Maier, S. A.; Pendry, J. B. Plasmonic Light-Harvesting Devices over the Whole Visible Spectrum. *Nano Lett.* **2010**, *10*, 2574–2579.

(6)   Papadakis, G. T.; Fleischman, D.; Davoyan, A.; Yeh, P.; Atwater, H. A. Optical Magnetism in Planar Metamaterial Heterostructures. *Nat. Commun.* **2018**, *9*, 296.

(7)   Ginn, J. C.; Brener, I.; Peters, D. W.; Wendt, J. R.; Stevens, J. O.; Hines, P. F.; Basilio, L. I.; Warne, L. K.; Ihlefeld, J. F.; Clem, P. G.; Sinclair, M. B. Realizing Optical Magnetism from Dielectric Metamaterials. *Phys. Rev. Lett.* **2012**, *108*, 097402.

(8)   Drachev, V. P.; Chettiar, U. K.; Kildishev, A. V.; Yuan, H.-K.; Cai, W.; Shalaev, V. M. The Ag Dielectric Function in Plasmonic Metamaterials. *Opt. Express* **2008**, *16*, 1186.

(9)   William J. Tropf, Michael E. Thomas, and T. J. H. *Handbooks of Optics*; McGRAW-HILL , INC.

(10)   Martin Dressel, G. G. *Electrodynamics of Solids*, first.; Cambrige university press, Ed.; 2002.

(11)   Rakić, A. D.; Djurišić, A. B.; Elazar, J. M.; Majewski, M. L. Optical Properties of Metallic Films for Vertical-Cavity Optoelectronic Devices. *Appl. Opt.* **1998**, *37*, 5271.

(12)   Shalaev, V. M. Optical Negative-Index Metamaterials. *Nat. Photonics* **2007**, *1*, 41–48.

(13)   Gómez-Castaño, M.; Zheng, H.; García-Pomar, J. L.; Vallée, R.; Mihi, A.; Ravaine, S. Tunable Index Metamaterials Made by Bottom-up Approaches. *Nanoscale Adv.* **2019**, *1*,

1070–1076.

(14) Hetterich, J.; Bastian, G.; Gippius, N. A.; Tikhodeev, S. G.; von Plessen, G.; Lemmer, U. Optimized Design of Plasmonic MSM Photodetector. *IEEE J. Quantum Electron.* **2007**, *43*, 855–859.

(15) Shen, K.-C.; Chen, C.-Y.; Chen, H.-L.; Huang, C.-F.; Kiang, Y.-W.; Yang, C. C.; Yang, Y.-J. Enhanced and Partially Polarized Output of a Light-Emitting Diode with Its InGaN/GaN Quantum Well Coupled with Surface Plasmons on a Metal Grating. *Appl. Phys. Lett.* **2008**, *93*, 231111.

(16) Shiohara, A.; Wang, Y.; Liz-Marzán, L. M. Recent Approaches toward Creation of Hot Spots for SERS Detection. *J. Photochem. Photobiol. C Photochem. Rev.* **2014**, *21*, 2–25.

(17) Deng, W.; Xie, F.; Baltar, H. T. M. C. M.; Goldys, E. M. Metal-Enhanced Fluorescence in the Life Sciences: Here, Now and Beyond. *Phys. Chem. Chem. Phys.* **2013**, *15*, 15695.

(18) Wu, X.; Zhang, J.; Chen, J.; Zhao, C.; Gong, Q. Refractive Index Sensor Based on Surface-Plasmon Interference. *Opt. Lett.* **2009**, *34*, 392.

(19) Baryshev, A.; Merzlikin, A. Plasmonic Photonic-Crystal Slabs: Visualization of the Bloch Surface Wave Resonance for an Ultrasensitive, Robust and Reusable Optical Biosensor. *Crystals* **2014**, *4*, 498–508.

(20) Homola, J.; Yee, S. S.; Gauglitz, G. Surface Plasmon Resonance Sensors: Review. *Sensors Actuators B Chem.* **1999**, *54*, 3–15.

(21) Pines, D. Collective Energy Losses in Solids. *Rev. Mod. Phys.* **1956**, *28*, 184–198.

(22) Cardona, M.; Güntherodt, G. Light Scattering in Solids IV. **1984**, *54*, 1210–1210.

(23) Kociak, M.; Stéphan, O. Mapping Plasmons at the Nanometer Scale in an Electron Microscope. *Chem. Soc. Rev.* **2014**, *43*, 3865.

(24) Novotny, L.; Hecht, B. *Principles of Nano-Optics*; Cambridge University Press, 2006.

(25) Bohren, C. F.; Huffman, D. R. *Absorption and Scattering of Light by Small Particles*; Wiley, 1983.

(26) Louis, C.; Pluchery, O. *Gold Nanoparticles for Physics, Chemistry and Biology*; IMPERIAL COLLEGE PRESS, 2012.

(27) Kreibig, U.; Vollmer, M. *Optical Properties of Metal Clusters*; Springer Series in Materials Science; Springer Berlin Heidelberg: Berlin, Heidelberg, 1995; Vol. 25.

(28)   Wang, W.; Ramezani, M.; Väkeväinen, A. I.; Törmä, P.; Gómez Rivas, J.; Odom, T. W. The Rich Photonic World of Plasmonic Nanoparticle Arrays. **2017**.

(29)   Kim, J.-Y.; Han, M.-G.; Lien, M.-B.; Magonov, S.; Zhu, Y.; George, H.; Norris, T. B.; Kotov, N. A. Dipole-like Electrostatic Asymmetry of Gold Nanorods. *Sci. Adv.* **2018**, *4*, e1700682.

(30)   Raether, H. Surface Plasmons on Smooth Surfaces; springer-verlag, Ed.; 1988; pp 4–39.

(31)   Arakawa, E. T.; Williams, M. W.; Hamm, R. N.; Ritchie, R. H. Effect of Damping on Surface Plasmon Dispersion. *Phys. Rev. Lett.* **1973**, *31*, 1127–1129.

(32)   Alexander, R. W.; Kovener, G. S.; Bell, R. J. Dispersion Curves for Surface Electromagnetic Waves with Damping. *Phys. Rev. Lett.* **1974**, *32*, 154–157.

(33)   Zhang, J.; Zhang, L.; Xu, W. Surface Plasmon Polaritons: Physics and Applications. *J. Phys. D. Appl. Phys.* **2012**, *45*, 113001.

(34)   Maier, S. A. *Plasmonics : Fundamentals and Applications*; Springer, 2007.

(35)   Kretschmann, E.; Raether, H. Radiative Decay of Non Radiative Surface Plasmons Excited by Light. *Zeitschrift für Naturforsch. A* **1968**, *23*, 2135–2136.

(36)   Yablonovitch, E. Inhibited Spontaneous Emission in Solid-State Physics and Electronics. *Phys. Rev. Lett.* **1987**, *58*, 2059–2062.

(37)   John, S.; Wang, J. Quantum Electrodynamics near a Photonic Band Gap: Photon Bound States and Dressed Atoms. *Phys. Rev. Lett.* **1990**, *64*, 2418–2421.

(38)   Kittel, C. *Introduction to Solid State Physics.*; Wiley, 1971.

(39)   Wang, K. X.; Yu, Z.; Liu, V.; Raman, A.; Cui, Y.; Fan, S. Light Trapping in Photonic Crystals. *Energy Environ. Sci.* **2014**, *7*, 2725.

(40)   Yang, A.; Hoang, T. B.; Dridi, M.; Deeb, C.; Mikkelsen, M. H.; Schatz, G. C.; Odom, T. W. Real-Time Tunable Lasing from Plasmonic Nanocavity Arrays. *Nat. Commun.* **2015**, *6*.

(41)   Fano, U. The Theory of Anomalous Diffraction Gratings and of Quasi-Stationary Waves on Metallic Surfaces (Sommerfeld's Waves). *J. Opt. Soc. Am.* **1941**, *31*, 213.

(42)   García de Arquer, F. P.; Mihi, A.; Konstantatos, G. Large-Area Plasmonic-Crystal–Hot-Electron-Based Photodetectors. *ACS Photonics* **2015**, *2*, 950–957.

(43)   Li, J.; Kamin, S.; Zheng, G.; Neubrech, F.; Zhang, S.; Liu, N. Addressable Metasurfaces

for Dynamic Holography and Optical Information Encryption. *Sci. Adv.* **2018**, *4*, eaar6768.

(44)   Krupin, O.; Berini, P.; Krupin, O.; Berini, P. Long-Range Surface Plasmon-Polariton Waveguide Biosensors for Human Cardiac Troponin I Detection. *Sensors* **2019**, *19*, 631.

(45)   Koenderink, A. F. Plasmon Nanocavity Array Lasers: Cooperating over Losses and Competing for Gain. *ACS Nano* **2019**, *13*, 7377–7382.

(46)   Han, X.; Liu, K.; Sun, C. Materials Plasmonics for Biosensing. **2017**.

(47)   Wang, H. Plasmonic Refractive Index Sensing Using Strongly Coupled Metal Nanoantennas: Nonlocal Limitations. *Sci. Rep.* **2018**, *8*, 9589.

(48)   Langer, J.; Novikov, S. M.; Liz-Marzán, L. M. Sensing Using Plasmonic Nanostructures and Nanoparticles. *Nanotechnology* **2015**, *26*, 322001.

(49)   Ramezani, M.; Lozano, G.; Verschuuren, M. A.; Gómez-Rivas, J. Modified Emission of Extended Light Emitting Layers by Selective Coupling to Collective Lattice Resonances. *Phys. Rev. B* **2016**, *94*, 125406.

(50)   Zhang, J.; Zhang, L.; Xu, W.; Zayats, A. V; Smolyaninov, I. I. *Near-Field Photonics: Surface Plasmon Polaritons and Localized Surface Plasmons Related Content Radiation Guiding with Surface Plasmon Polaritons Zhanghua Han and Sergey I Bozhevolnyi-Surface Plasmon Polaritons: Physics and Applications Near-Field Photonics: Surface Plasmon Polaritons and Localized Surface Plasmons*; 2003.

(51)   Kou, S. S.; Yuan, G.; Wang, Q.; Du, L.; Balaur, E.; Zhang, D.; Tang, D.; Abbey, B.; Yuan, X.-C.; Lin, J. On-Chip Photonic Fourier Transform with Surface Plasmon Polaritons. *Light Sci. Appl.* **2016**, *5*, e16034–e16034.

(52)   Kasprzak, J.; Richard, M.; Kundermann, S.; Baas, A.; Jeambrun, P.; Keeling, J. M. J.; Marchetti, F. M.; Szymańska, M. H.; André, R.; Staehli, J. L.; Savona, V.; Littlewood, P. B.; Deveaud, B.; Dang, L. S. Bose–Einstein Condensation of Exciton Polaritons. *Nature* **2006**, *443*, 409–414.

(53)   Baumberg, J. J.; Kavokin, A. V.; Christopoulos, S.; Grundy, A. J. D.; Butté, R.; Christmann, G.; Solnyshkov, D. D.; Malpuech, G.; Baldassarri Höger von Högersthal, G.; Feltin, E.; Carlin, J.-F.; Grandjean, N. Spontaneous Polarization Buildup in a Room-Temperature Polariton Laser. *Phys. Rev. Lett.* **2008**, *101*, 136409.

(54)   Kühn, S.; Håkanson, U.; Rogobete, L.; Sandoghdar, V. Enhancement of Single-

Molecule Fluorescence Using a Gold Nanoparticle as an Optical Nanoantenna. *Phys. Rev. Lett.* **2006**, *97*, 017402.

(55)   Wang, J.; Jia, S.; Cao, Y.; Wang, W.; Yu, P. Design Principles for Nanoparticle Plasmon-Enhanced Organic Solar Cells. *Nanoscale Res. Lett.* **2018**, *13*, 211.

(56)   Baek, S.; Molet, P.; Choi, M.; Biondi, M.; Ouellette, O.; Fan, J.; Hoogland, S.; García de Arquer, F. P.; Mihi, A.; Sargent, E. H. Nanostructured Back Reflectors for Efficient Colloidal Quantum-Dot Infrared Optoelectronics. *Adv. Mater.* **2019**, *31*, 1901745.

(57)   Atwater, H. A.; Polman, A. Plasmonics for Improved Photovoltaic Devices. *Nat. Mater.* **2010**, *9*, 205–213.

(58)   Agrawal, A.; Gupta, N.; Das, A.; Ahmed, K.; Dhawan, A. Nanostructured Plasmonic Gold Films for Enhanced Sensitivity of SPR Biological Sensing and Imaging. In *Plasmonics in Biology and Medicine XVI*; Vo-Dinh, T., Ho, H.-P. A., Ray, K., Eds.; SPIE, 2019; Vol. 10894, p 21.

(59)   Moskovits, M. Surface-Enhanced Raman Spectroscopy: A Brief Perspective. In *Surface-Enhanced Raman Scattering*; Springer Berlin Heidelberg; pp 1–17.

(60)   Du, L.; Lei, D. Y.; Yuan, G.; Fang, H.; Zhang, X.; Wang, Q.; Tang, D.; Min, C.; Maier, S. A.; Yuan, X. Mapping Plasmonic Near-Field Profiles and Interferences by Surface-Enhanced Raman Scattering. *Sci. Rep.* **2013**, *3*, 3064.

(61)   Hoang, T. B.; Akselrod, G. M.; Mikkelsen, M. H. Ultrafast Room-Temperature Single Photon Emission from Quantum Dots Coupled to Plasmonic Nanocavities. *Nano Lett.* **2016**, *16*, 270–275.

(62)   de Nijs, B.; Benz, F.; Barrow, S. J.; Sigle, D. O.; Chikkaraddy, R.; Palma, A.; Carnegie, C.; Kamp, M.; Sundararaman, R.; Narang, P.; Scherman, O. A.; Baumberg, J. J. Plasmonic Tunnel Junctions for Single-Molecule Redox Chemistry. *Nat. Commun.* **2017**, *8*, 994.

(63)   Nordlander, P.; Oubre, C.; Prodan, E.; Li, K.; Stockman, M. I. Plasmon Hybridization in Nanoparticle Dimers. *Nano Lett.* **2004**, *4*, 899–903.

(64)   Li, G.-C.; Zhang, Y.-L.; Jiang, J.; Luo, Y.; Lei, D. Y. Metal-Substrate-Mediated Plasmon Hybridization in a Nanoparticle Dimer for Photoluminescence Line-Width Shrinking and Intensity Enhancement. *ACS Nano* **2017**, *11*, 3067–3080.

(65)   Ralph Sherman Becker. *Theory and Interpretation of Fluorescence and*

Phosphorescence ; 1969.

(66)   Lichtman, J. W.; Conchello, J.-A. Fluorescence Microscopy. **2005**.

(67)   Bauch, M.; Toma, K.; Toma, M.; Zhang, Q.; Dostalek, J. Plasmon-Enhanced Fluorescence Biosensors: A Review. *Plasmonics* **2014**, *9*, 781–799.

(68)   Purcell, E. M. Spontaneous Emission Probabilities at Radio Frequencies; Springer, Boston, MA, 1995; pp 839–839.

(69)   Kneipp, K.; Kneipp, H.; Itzkan, I.; Dasari, R. R.; Feld, M. S. Surface-Enhanced Raman Scattering and Biophysics. *J. Phys. Condens. Matter* **2002**, *14*, 202.

(70)   Larkin, P. (Peter J. . *Infrared and Raman Spectroscopy : Principles and Spectral Interpretation*; Elsevier, 2011.

(71)   Le Ru, E.; Etchegoin, P. Principles of Surface Enhanced Raman Spectroscopy and Related Plasmonic Effets. *Elsevier* **2009**, *1*, 1–663.

(72)   William G. Fateley, Francis R. Dollish, N. T. M. und F. F. B. Infrared and Raman Selection Rules for Molecular and Lattice Vibrations. *Berichte der Bunsengesellschaft für Phys. Chemie* **1974**, *78*, 212–212.

(73)   Fleischmann, M.; Hendra, P. J.; McQuillan, A. J. Raman Spectra of Pyridine Adsorbed at a Silver Electrode. *Chem. Phys. Lett.* **1974**, *26*, 163–166.

(74)   Moskovits, M. Surface Roughness and the Enhanced Intensity of Raman Scattering by Molecules Adsorbed on Metals. *J. Chem. Phys* **1978**, *69*, 4159.

(75)   Stiles, P. L.; Dieringer, J. A.; Shah, N. C.; Van Duyne, R. P. Surface-Enhanced Raman Spectroscopy. *Annu. Rev. Anal. Chem.* **2008**, *1*, 601–626.

(76)   Aroca, R. Vibrational Spectroscopy (SERS and SERRS). *J. Mol. Struct.* **1993**, *292*, 17–27.

(77)   Pluchery, O.; Humbert, C.; Valamanesh, M.; Lacaze, E.; Busson, B. Enhanced Detection of Thiophenol Adsorbed on Gold Nanoparticles by SFG and DFG Nonlinear Optical Spectroscopy. *Phys. Chem. Chem. Phys.* **2009**, *11*, 7729.

(78)   Solís, D. M.; Taboada, J. M.; Obelleiro, F.; Liz-Marzán, L. M.; García de Abajo, F. J. Optimization of Nanoparticle-Based SERS Substrates through Large-Scale Realistic Simulations. *ACS photonics* **2017**, *4*, 329–337.

(79)   Xu, H.; Bjerneld, E. J.; Käll, M.; Börjesson, L. Spectroscopy of Single Hemoglobin Molecules by Surface Enhanced Raman Scattering. *Phys. Rev. Lett.* **1999**, *83*, 4357–

4360.

(80)   Wustholz, K. L.; Henry, A.-I.; McMahon, J. M.; Freeman, R. G.; Valley, N.; Piotti, M. E.; Natan, M. J.; Schatz, G. C.; Van Duyne, R. P. Structure−Activity Relationships in Gold Nanoparticle Dimers and Trimers for Surface-Enhanced Raman Spectroscopy. *J. Am. Chem. Soc.* **2010**, *132*, 10903–10910.

(81)   Tserkezis, C.; Taylor, R. W.; Beitner, J.; Esteban, R.; Baumberg, J. J.; Aizpurua, J. Optical Response of Metallic Nanoparticle Heteroaggregates with Subnanometric Gaps. *Part. Part. Syst. Charact.* **2014**, *31*, 152–160.

(82)   Savage, K. J.; Hawkeye, M. M.; Esteban, R.; Borisov, A. G.; Aizpurua, J.; Baumberg, J. J. Revealing the Quantum Regime in Tunnelling Plasmonics. *Nature* **2012**, *491*, 574–577.

(83)   Fang, Y.; Seong, N.-H.; Dlott, D. D. Measurement of the Distribution of Site Enhancements in Surface-Enhanced Raman Scattering. *Science (80-.).* **2008**, *321*, 388–392.

FABRICATION AND CHARACTERIZATION OF NANOSTRUCTURES

Nanotechnology is getting into our daily life; we are constantly using micro and nano devices that help us to communicate and navigate on the web. They measure our health parameters such as blood pressure and glucose level, monitor and control automotive safety parameters such as airbags and tire pressure, enable us to enjoy realistic augmented reality and video gaming.

Nowadays the only industry where nanoscale manufacturing technologies are employed on a large scale is the semiconductor industry, where device structures have reached the single nanometers scale. However, in the last decades we have experienced an important revolution were many efforts have spent to expand the impact of nanotechnology in field such as medicine, energy harvesting, or computing. Here the importance of advanced and non-conventional nanofabrication techniques that allows unprecedented flexibility for several applications.

In the first part of this chapter we introduce the state-of-the-art of nanofabrication classifying each technique by their approach into top-down or bottom-up. Furthermore, new methods were developed from the merger of these two latter approaches in order to overcome some of their intrinsic drawback. In the second part of this chapter we look at the main characterization techniques that aid the study plasmonic device both form the morphological and optical point of view.

~ ● ~

2.1 NANOFABRICATION TECHNOLOGY

Nanofabrication has received intensive attention in the scientific community. Interestingly, when scaling down to nano we enter to another level of complexity with a multitude of new phenomena in optics, electronic, chemistry, biology and many other fields that are no longer ruled by classical physics but better respond to quantum mechanics. One of the main issues however is still the fabrication of nanometer scale structures. In this regard, science and technology have tried to tackle the problem of building nano objects developing specific and advanced techniques. We can classify them into two main approaches: i) top-down, that relies on the fabrication of smaller devices by extruding nanometer object from a bulk material; ii) bottom-up, that relies in the physical and chemical interactions between molecule or atoms as well as nanoparticles that are programmed to assemble together into a more complex system.

In this chapter we will introduce some of the most advanced technique that have been using during the last decades driving the development of new materials.

2.2 TOP-DOWN APPROACHES

Top down nanofabrication refers to those techniques in which a bulk material is sliced down or eroded to form nanometric structures, or a desired nanopattern. Nanotechnology techniques for top down fabrication can be split into mechanical and chemical fabrication techniques depending on the process used to chip away the bulk material.

The most common and used top down fabrication technique is nanolithography. In this process, a material is protected by a mask that imposes a pattern on the target. Depending on the level of resolution required in the final product, etching of the base material can be done chemically using acids or mechanically electron or ion beams. The latter case is the technique applied to the manufacture of integrated circuits, CPUs, as well as sensors and next generation displays.

2.2.1 Photolithography

- *Interference lithography*

Interference lithography is a lithographic technique well established in semiconductor industry that uses the interference of two or more coherent beams that form an interference pattern on the material. This interference pattern is transferred to a photoresist and further application of dry etching techniques transfers the pattern on the substrate, typically silicon (Figure 2.1a).
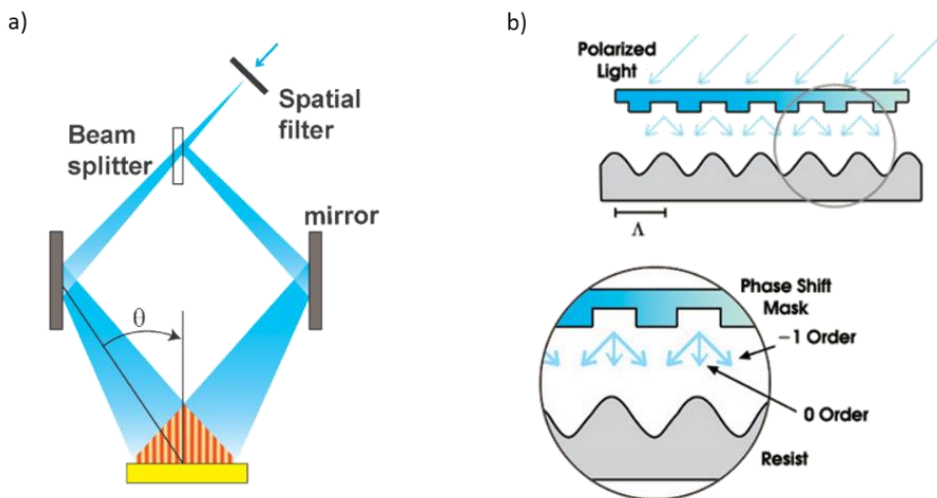
Figure 2.1 Simple sketch of (a) interference lithography setup, (b) holographic lithography setup

- *Near field holographic*

Near field holographic lithography, (Figure 2.1b) is very similar to interference lithography. It uses a phase mask near the substrate to divide one beam into two diffracted beams propagating at different angles. These two beams interfere and generate diffraction patterns in the photoresist. Afterwards, etching techniques are applied similarly as the previous technique.

Both methods (IL and NFH) can produce patterns over large areas, but the resolution is limited by the laser wavelength.

2.2.2 Charged particles lithography

These techniques use charged particles instead of photons to create patterns. The use of charged particles such as electrons, ions, or protons allows both patterning and imaging the sample. In contrast with most common photolithographic techniques, the absence of a mask allows the designs of a multitude of shapes that are generated on computer software and written with the particle beam onto a substrate. The accelerated particles are focused on the surface of the sensitive material allowing the direct exposure point by point at a time. A small beam size, down to 1-2 nm, can be achieved and due to the nature of charged particles, unlike photolithography, diffraction does not interfere with patterning thus yielding sub-10 nm size features.

The most extensively used charged particle techniques are electron beam lithography and focused ion beam lithography.

- *Electron beam lithography*

Electron beam lithography (EBL), uses high energy electrons finely focused on a surface coated with an electron sensitive resist. This technique is classified as a resist-based lithography where the resin materials are specially formulated to undergo chemical reactions once they are exposed to the appropriate energy. In negative resist the electron beam cross-links the molecular bonds thus smaller precursors form larger and insoluble chain of polymer. In the other hand, positive resist, such Poly(methyl methacrylate) (PMMA) consists in small molecules that cross-link by the action of the electrons leading to larger polymer chain with reduced solubility. The change in solubility is essential to reveal the structure once the substrate is washed and rinsed with a solvent called developer. The resulting patterns can be transferred in the substrate using etching or lift off processes. Note that PMMA is commonly used as a positive resist but can also be used in a negative manner with exposure at higher dose levels.[1]

- *Focused ion beam lithography*

Focused ion beam lithography (FIB) uses high-energy ions, charged particles heavier than electrons that can effectively mill substrates like germanium (Ge)

or silicon (Si), carving the desired shapes and patterns. For this reason, this technique does not require a resist. However, objects with high density, narrow linewidth and challenging pattern geometry significantly increase writing times that can exceed a week for few micrometer square patterns. This drawback drastically reduces the viability for large scale and volume fabrication. Along with the latter concern, another important factor is the need of a fast and extremely accurate mechanical stage that, even in high-end systems, makes writing of a single wafer time consuming. These features make this method one of the most expensive techniques.

Despite their low throughput, the multiple design possibilities of FIB allow the fabrication of complex proof of concept nanostructures. However, the need to bring nanotechnology to large scale manufacturing prompts the development of non-conventional lithography which allow to overcome their main drawback.

2.2.3   Nanoimprint lithography

The term nanoimprint lithography was coined in the scientific literature in 1996 when Stephen Chou et. Al. published a work about high-throughput, low-cost, nonconventional lithographic method.[2] From then this technique have been growing exponentially thanks to its versatility and the possibility to achieve high resolution beyond the limit set by diffraction. In addition, the high throughputs compared with e-beam lithography paves the way for future scale-up of nanostructured systems. Nanoimprint lithography uses a mold to produce nanoscale deformation of a resist, which is then cured either by heat or UV application. Once the resist is cured the mold is removed and the patterned resist can be treated through wet or dry etching. In this thesis the reactive ion etching technique have been used in combination with NIL to transfer patterns on silicon or to tune the depth of the nanostructures. In RIE chemically reactive ions and high energy electrons are excited by a RF field and accelerated by an electric field towards a the target substrate.[37] This etching process ends up with different nanostructure's depth depending on the exposure time. Although this

process is expensive and time consuming, it has to be performed only once and the master can be reused hundreds of times.

The imprinted structures can also be directly used as a substrate for metal deposition and other standard lithographic techniques to generate either a final device or a new mold for further processing. Contrary to the EBL or FIB this approach take advantage of the possibility to pattern a wide range of materials from biopolymers like cellulose, to nanoparticles as well as common resist as PMMA or SU8. [3–5]

Structuring polymeric materials down to the single nanometer level has already been reported.[6] The example in Figure 2.2 depicts how a 2D photonic-crystal laser can be prepared by direct thermal nanoimprint lithography by simply spin-coating layer of a methyl-ammonium lead iodide perovskite and performing thermal imprint, at a temperature as low as 100 °C.[7] The nanopattern of the stamp has been shown to be efficiently transferred via recrystallization of the perovskite. Organo-lead halide perovskites combine optoelectronic properties known from the crystalline inorganic semiconductors with the photonic effect coming from the pattern.

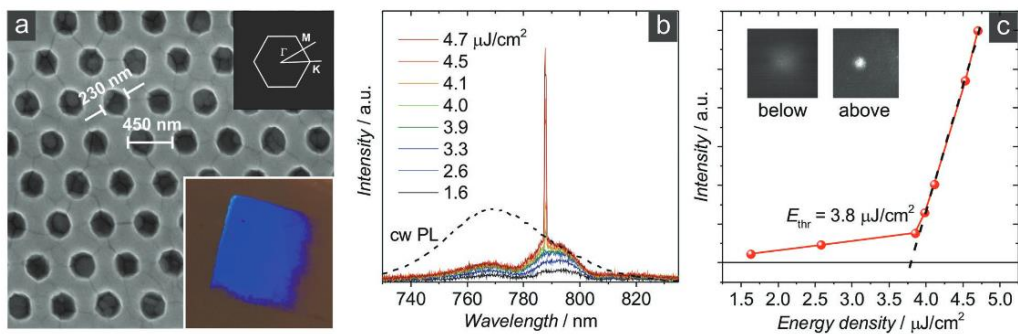*Figure 2.2 2D photonic crystal imprinted on lead iodide perovskite leads to low threshold laser. Reprinted from ref.69*

Although the excellent outlook of photonic or plasmonic optoelectronic devices based on semiconductors, the most recent application and breakthrough of NIL is the development of flexible organic electronics. In these areas the development of sensors,[8–10] actuators,[11,12] displays,[13] lenses[14] and artificial

skin[15,16] have been extensive exploited due to the innovative outlooks that these devices have in field like medicine, robotics, an energy conversion.

We can divide NIL into two main categories depending on the protocol used to transfer the patter i.e. thermal and ultraviolet NIL.

- *Thermal NIL*

Thermal NIL (T-NIL) also known as hot embossing process is the earliest type of NIL which involves imprinting onto a thermally softened thermoplastic resist. It provides tools to pattern wide variety of materials even though the best candidates for this technique are materials whose glass transition temperature (Tg) is around 100ºC (Figure 2.3). These are typically polymers but also epoxy resin or biomolecules.[17]
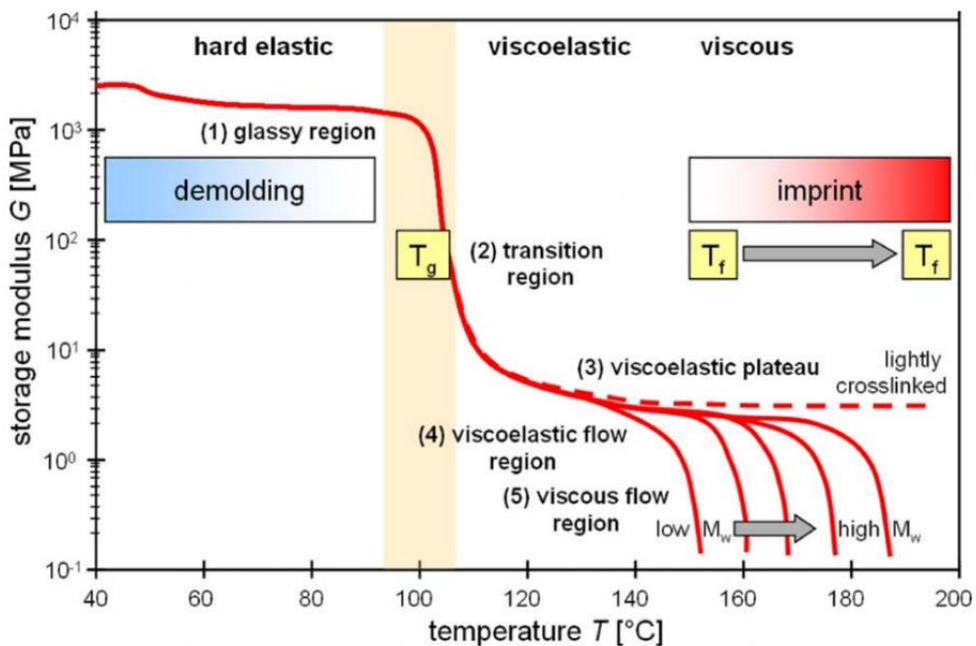
Figure 2.3. Scheme of the mechanical properties for polymers with a glass transition temperature T_g around 100ºC for a normal process condition showing the effect of different molecular weights M_w. Notice the drop of the storage modulus G at T_g (thermomechanical properties between stamp and polymer become sufficiently different for repeated molding) and T_f (temperature at which viscosity drops to the needed values for imprint). Reprinted from ref. 17

T-NIL process follows four main steps:

i) Heating up. The target resist is first heated up above its glass transition temperature (Tg). This step softens the resin making possible the following imprinting.

ii) Imprint. The mold is pressed on hot the resist layer which easily flows in the pattern reliefs;

iii) Cooling down. The temperature is lowered below the Tg and the resist solidifies;

iv) Lift-Off. The mold is lifted leaving its negative image on the resist;

- *UV NIL*

In UV-NIL, a UV-curable monomer or oligomer is spin coated or drop dispensed on a substrate. Imprinting is carried out with a transparent template (quartz, glass or soft stamps) and the imprinted structures are cured by UV-light exposure which cross-links the resist. Subsequently the template is released from the imprinted substrate. The UV-NIL process has several prominent advantages over the thermal NIL process. The capability to be conducted at room temperature helps to eliminate issues resulting from different thermal expansion between the mold, substrate, and resist. In addition, the imprinting process involves a less viscous liquid photo-resist, hence allows the use of lower imprint pressures compared to T-NIL.

Hard mold, soft-mold, and hybrid molds nanoimprint

Nanoimprint lithography can be divided into three different techniques depending on the stiffness of the molds, i.e. hard mold, soft-mold, and hybrid molds nanoimprint.

- *Hard nanoimprint*

Hard nanoimprint lithography employs a mold made of a rigid material such as silicon or quartz, Chou et. al. relied on direct mechanical deformation of the resist material under a rigid silicon mold, enabling the support of fine features as small as 1 nm.[6] This high resolution comes at the cost of higher defect rates caused mainly by inflexibility of the molds, which creates "air bubbles" between the mold and the resist coated substrates. In our work we took

advantage of this technique to fabricate working master from the original silicon wafer. We use an optimized protocol to reduce the defects yielding homogenous and high-resolution replicas.

OrmoStamp® fabrication

This resin has been extensively used in this work to fabricate working masters. In particular it helps to obtain a reliable and nearly defect-free negative image of the original nanostructures fabricated on silicon though E-beam lithography of interference lithography. This material is a photocurable polydimethylsiloxane with high young modulus (650MPa) suitable to replicate fine structures with high aspect ratio (e.g. high pillars array) avoiding collapse. The resin is used as purchased. We place a drop on a silanized silicon master then a UVO treated glass slide is placed on top to spread the drop onto the patterned area. This modified protocol allows the replication of defect free nanostructures patterns. The resin is then activated and baked under UV light and post baked for 30min at 130°C to help the release. Working Ormostamp Masters have been used in this thesis to fabricate soft molds for template assisted self-assembly which will be discussed in chapter 4.

- *Soft nanoimprint*

The rigid molds used in hard NIL lead to defects that can be reduced by conformal contact between the mold and the substrate. In order to address this challenge, the concept of soft lithography was extended to nanoimprint lithography through the use of molds composed of elastomeric material such as Poly(dimethylsiloxane) (PDMS), polyimides and polyurethanes, although PDMS is by far the most common material.[18] These techniques rely in the conformal contact between a stamp, usually a soft polymer, and a target material.[17] Elastomeric materials can either be used as a freestanding mold for applications on curved or rough surfaces. Soft nanoimprint lithography has been further extended to roll-to-roll nanoimprint lithography for extremely high volume, low cost applications.[19]

Soft PDMS molds fabrication

Poly(dimethylsiloxanes) is a composed by dimethylsiloxanes monomers that condensate to form a crosslinked structure whose mechanical properties changes with the number of links between siloxane chains.

In this work we used the standard mixture 1:10 curing agent/Prepolymer (CA/P) which leads flexible molds with young module of ~1MPa that displays good mechanical properties along with high nanometric resolution (200nm). For higher CA/P ration we obtain stiffer and brittle PDMS. On the other hand, for lower ratio the resulting mold will be softer and more stretchable, useful for applications in stretchable nanostructured devices.

- *Hybrid mold nanoimprint*

Hybrid mold nanoimprint lithography has been introduced in order to solve the issues arising from the conventional soft-mold nanoimprint lithography that uses deformable polymer as a mold for patterning. The resolution and surface chemistry totally depended upon the chemical structure of the polymer used for the mold that often compromises the resolution and scalability of NIL. The use of hybrid molds completely resolves this problem taking advantage that even the harder material becomes flexible when it is extremely thin. Thus, by reducing the thickness of stiff polymer we retain its high young modulus and mechanical strength but make them flexible and suitable for nanoimprint lithography. The thin hard material is used with a soft backbone (usually soft PDMS) to form the hybrid mold. This technique has potential for industrial nanoscale fabrication since provides high throughput, large scale and low-cost patterning with no losses in nanostructures resolution.

Hard/Soft PDMS molds Fabrication

This material has a number of desirable properties such as mechanical rigidity (>9Mpa), flexibility, small shrinkage, and light transmittance to UV. The procedure follows an optimized protocol which involves a first hard PDMS fabrication followed by a backbone insertion. Prior to apply hard PDMS on the master, the mixture containing prepolymer, catalyzer, retardant and curing agent, is diluted in toluene which decrees its viscosity and enhance the percolation into small features (<10nm). Once spread over the master, the hard

layer is backed at 60°C for 1h and then a 1:10 mixture of soft PDMS is poured on top. The resulting hybrid mold is used in this thesis for the fabrication of holes array described in chapter 3.

2.3   BOTTOM-UP APPROACHES

Bottom-up approaches use chemical and physical forces at the nanoscale level to assemble simple units into larger structures.

The bottom-up approach has a better chance of producing nanostructures that have fewer defects and better chemical composition than they would with the top-down methods, as well as having a more homogenous chemical composition and better short- and long-range ordering. There are numerous techniques that can be used for bottom-up fabrication, and these include vapor-phase deposition, colloidal synthesis, and molecular or colloidal self-assembly.

2.3.1   Vapor phase depositions

These techniques are the cheapest for mass production of nanostructures of metal and oxides. They offer the advantage of synthesizing different types of materials using simple and cost-effective setups. Depending on the way the vapor is formed they can be classified into chemical vapor deposition (CVD) of physical vapor deposition (PVD). In this thesis thermal evaporation (a PVD method) has been used to fabricate metallic thin film on top of ordered arrays. Thermal evaporation is carried on inside a vacuum chamber (10-7bar) where the metal is placed in a boat and heated to its melting point. The substrate is placed facing the source. During the evaporation a current flowing through the boat heats it up and causes the evaporation. A crystal monitor is mounted close to the substrates which provide an estimate evaporation rate value. In chapter 3, silver nanostructures will be fabricated through thermal evaporation demonstrating the possibility to use this method for large scale and reliable plasmonic devices.

2.3.2 Colloidal synthesis

An opposite approach is to synthesize the material from atomic or molecular species via chemical reactions, allowing for the precursor particles to grow in size toward different possible shapes. Colloidal methods are simple and well-established wet chemistry precipitation processes in which solutions of the different ions are mixed under controlled temperature and concentration to form nanometric colloids. This allow the full control over shape and size, leading to highly monodisperse colloids. In chapter 4 I will present optimized methods for nanoparticles fabrications as a demonstration of the potential of this technique to build reliable colloids with uniform shape and size.

2.3.3 Self-assembly

Self-assembly both at molecular and at the mesoscale level is a process that gets closer to biological system where discrete components are driven to organize spontaneously into well-defined geometries by specific interactions. These interactions may arise due to the intrinsic properties of the individual elements composing the system or by the influence of applied external stimuli. Self-assembly of colloidal suspensions, molecular species, and biological systems relies in achieving a perfect balance between these forces. In this framework chemistry helps us to understand these attractive and repulsive interactions and give us tools to design systems which evolve toward a well-defined self-assembled architectures.[20]

The assembly of nanoscale colloids into macroscopic hierarchical structures depends on the manipulation of interparticle interactions such as Van der Waals interaction, Electrostatic Forces and Depletion forces. However, the nature of the dominant driving force depends also on a number of other parameters, including, but not limited to the relative and total concentrations of the constituents, the separation distances between them, their relative and actual size, solvent composition, temperature and other environmental conditions.

Several examples can be taken from literature. Figure 2.4a-d shows how DNA can drive the assembly on nanoparticles into glassy, crystalline or chiral nanostructures taking advantage of the specific interaction that occurs between double stranded DNA filaments.[21,22] This approach is extensively studied in biology and biomedicine for disease diagnostic and therapy. Similarly, to the latter, self-assembly under confinement is exploited more in material science optics and sensing. On the other hand, Figure 2.4b, c shows how the precise placement of nanoparticles driven by soft templates leads to highly ordered patterns.[23,24]
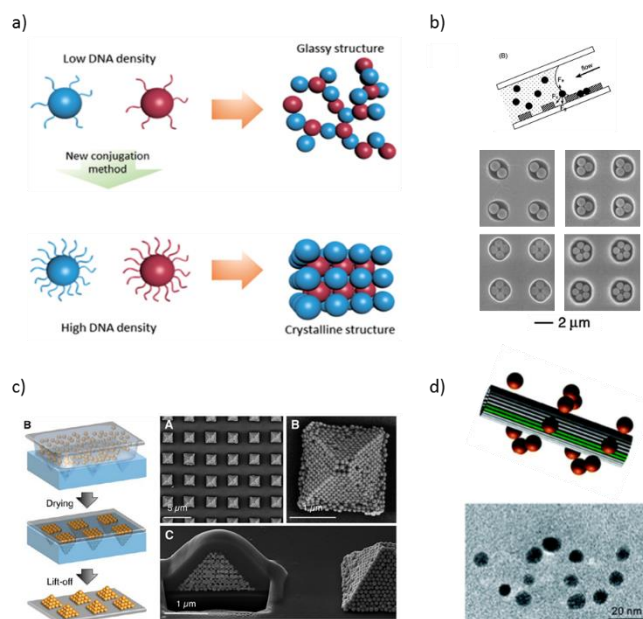

Figure 2.4 different examples of nanoparticle self-assembly for fabrication of functional materials. Reprinted from ref 56-59.

2.4   MERGER OF TOP-DOWN AND BOTTOM-UP APPROACHES

While top-down techniques offer unprecedented control over achievable geometries, by trend they suffer from being limited to planar and periodic structures. In contrast, materials fabricated with bottom-up techniques do not suffer from such disadvantages but, unfortunately, they offer only little control on achievable geometries. To overcome these limitations, hybrid top-down and

bottom-up process, can combine the best aspects of both and allow the integration of heterogeneous nano-components into higher-order structures and devices.

The possibility to impose fixed geometries and grow or assembly smaller component accordingly paves the way toward the development of new nanomaterial. This technology allows the development of reproducible substrates with controlled features like controllable sub micrometer gaps between plasmonic nanostructures combining NIL and atomic layer deposition (ALD). Another example is the fabrication of a large number of densely packed and randomly arranged metal-insulator-metal nanoparticles with a tailored optical response.[25] This process combines the patterning efficiency of electron-beam lithography and thermal evaporation an Au- SiO2-Au layer stack (Figure 2.5).
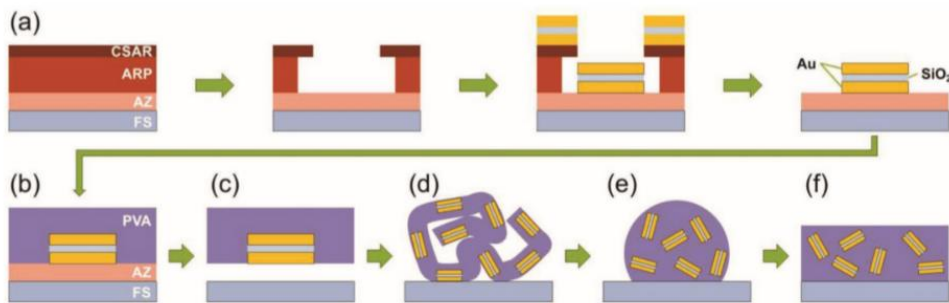

Figure 2.5. Schematic sketch of the applied process chain for a) realizing the deterministic meta-atoms and b–f) reorienting and rearranging the meta-atoms toward an artificial 3D photonic nanomaterial. Reprinted from ref.107.

2.5   CHARACTERIZATION OF PLASMONIC NANOSTRUCTURES

Plasmonic nanostructures are characterized both optically and morphologically. The structural characterization is often performed by using techniques that allow nanometer resolution imaging such as scanning electron microscopy (SEM), atomic force microscopy (AFM) and transmission electron microscopy (TEM). On the other hand, the optical properties tell us how our

plasmonic nanostructures interact with light and are as important as the structural ones. In this work the main technique used if the FTIR microspectroscopy but also Raman spectroscopy and photoluminescence spectroscopy.

2.5.1 Far-field characterization

Traditional techniques based on far field configuration consist in analyzing the absorption and extinction that the sample cause in the incident beam by collecting either the transmitted or reflected light

When standard bright field microscope is used to study nanometer-sized particles, the signal change from the original beam is to small even if we employ the most modern detectors or light sources. In order to improve this contrast, scattered light is usually studied with different set-ups designed to get rid of the incident light.

- *FTIR microspectroscopy*

Fourier Transform Infrared (FTIR) spectroscopy is based on the use of a Michelson interferometer in which the coherent incident beam is split into two equal parts by a beam splitter. One half is reflected to a fixed mirror and the other half is transmitted to a movable mirror. The beams are lateral recombined after introducing a small difference in their optical path to create an interference pattern (Figure 2.6). the resulting signal is called interferogram and contains information coded at each frequency, meaning that the whole range of frequencies is analyzed at once, resulting in a really fast measurement which allows for repeated measurements and a better signal to noise ration.

An incident light beam is impinging on the sample and the transmitted (or reflected) light is collected by an optical microscope coupled to a Fourier transform spectrometer that analyzes the difference in intensity as a function of the mirror position (i.e. the optical path difference). Thus, the transmission or reflection spectra normalized to a reference measurement which is usually taken from a bare transparent substrate (e.g. glass) background for transmission, and a mirror (Ag or Au) for reflection, are obtained through the

Fourier transform of the interferogram. The spectral resolution is determined by the retardation of the moving mirror within the Michelson interferometer: to double the resolution, the mirror need to be moved twice the original distance
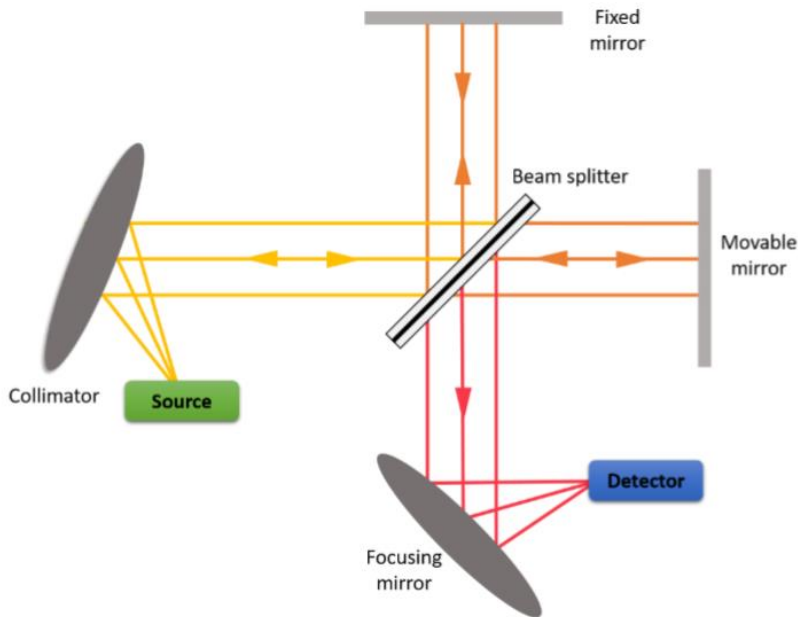

Figure 2.6. schematic sketch of a Michelson interferometer in a FT Vis/IR microscope

One of the advantages that FTIR presents is its multiplex character: each sampling contains information from all wavelength of the incoming light as compared to traditional dispersive instruments where each measurement point corresponds to a single wavelength. Besides, the absence of slits in the optical path allows more light to reach the detector improving the signal intensity.

- *Photoluminescence microspectroscopy*

Micro-photoluminescence spectroscopy is a powerful tool for investigating the optical and electronic properties of single nanostructures. The specimen is illuminated with light at specific wavelength which is absorbed by the fluorophores, causing them to emit light of longer wavelengths (i.e., of a different color than the absorbed light). The illumination light is separated from the much weaker emitted fluorescence through the use of a spectral emission

filter. Typical components of a fluorescence microscope are a light source, the excitation filter, the dichroic mirror, and the emission filter (Figure 2.7).
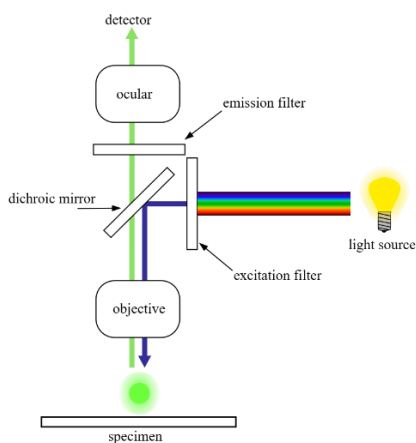
Figure 2.7 Simplified sketch of a fluorescence microscope. Note that the source can also be replaced with a monochromatic laser.

The filters and the dichroic beam splitter are chosen to match the spectral excitation and emission characteristics of the fluorophore used to label the specimen. In this manner, the distribution of a single fluorophore is imaged at a time.

- *Raman microspectroscopy*

The Raman microscope begins with a standard optical microscope, and adds an excitation laser, laser rejection filters, a spectrometer or monochromator, and an optical sensitive detector such as a charge-coupled device (CCD), or photomultiplier tube (Figure 2.8).

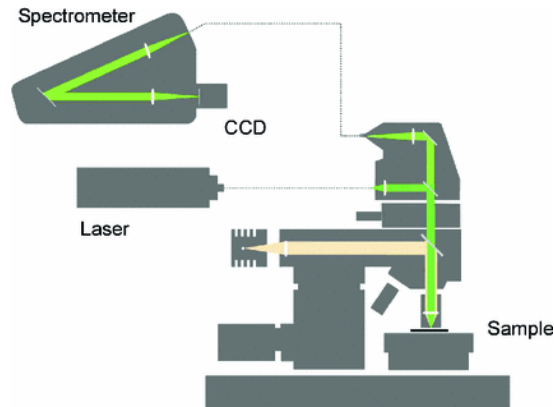*Figure 2.8 Simplified sketch of a Raman microscope*

Traditionally Raman microscopy was used to measure the Raman spectrum of a point on a sample, more recently the technique has been extended to implement Raman spectroscopy for direct chemical imaging over the whole field of view on a 3D sample.

2.6   CONCLUSION

As several exotic and different nanostructures can be fabricated by top down techniques, the fundamental research has already a tool to design complicated geometries. However, nowadays, the issue of building plasmonic nanostructures is shifting to the application point of view and many works are dealing with large area, scalable and high throughput requirements. Furthermore the inclusion of photonic architectures into the field of plasmonic is driving the fabrication and characterization to another level of complexity.

From the fabrication point of view, even though bottom up approaches are more process friendly, a non-trivial control over the whole possible parameter is required to extend this technique to commercial and industrial use. In this regards surface and colloidal chemistry helps us to play with nanoparticles and molecular system in order to engineer and program system able to self-assemble in the desired structure.

In this thesis we will merge bottom up and top down approaches to address the complex fabrication of plasmonic-photonic hybrid nanostructures. We will take

advance of the strength of the two techniques to engineer intense concentration of light at the nanoscale to enhance the light-matter interaction. In the following section two works carried out during my thesis will be presented. We present two generalized hybrid nanofabrication approach combining top-down (NIL) and bottom-up (thermal evaporation and colloidal self-assembly) fabrication techniques for the development of novel plasmonic platforms for sensing.

In the first one, nanoimprint lithography combined with glancing angle thermal evaporation of silver will be used to achieve the nanofabrication of large area asymmetric plasmonic nanostructures. The polarization dependent optical properties will be tuned as wanted to mold the interaction of hybrid plasmonic photonic modes with molecular dyes. Selective enhancement of photoluminescence will be then reported and demonstrated to be due to the intrinsic asymmetry of the nanostructures.

The second part will deal with template nanoparticles ensembles. Bridging the nanoscale level of probe (nanogaps) fabrication and the macroscale dimensions of sensor systems is one of the greatest challenges in the development of large-area plasmonic sensing platforms. SERS substrates take advantage of the intense EM filed enhancement with the gaps self-assembled hexagonally packed supercrystals but the novelty is not the assembly itself but its mesoscale organization. Actually, by simply organizing nanoparticle clusters in an ordered array whose constant is in the same length of the visible wavelength we can tune the plasmonic resonances, matching the laser excitation wavelength thus increasing the electric filed intensity responsible of surface enhanced Raman scattering.

2.7 REFERENCES

(1)   Hoole, A. C. F.; Welland, M. E.; Broers, A. N. Negative PMMA as a High-Resolution Resist - the Limits and Possibilities. *Semicond. Sci. Technol.* **1997**, *12*, 1166–1170.

(2)   Chou, S. Y.; Krauss, P. R.; Renstrom, P. J. *Nanoimprint Lithography*; 1996.

(3)   Dore, C.; Osmond, J.; Mihi, A. A Water-Processable Cellulose-Based Resist for Advanced Nanofabrication. *Nanoscale* **2018**, *10*, 17884–17892.

(4)   Matricardi, C.; Hanske, C.; Garcia-Pomar, J. L.; Langer, J.; Mihi, A.; Liz-Marzán, L. M. Gold Nanoparticle Plasmonic Superlattices as Surface-Enhanced Raman Spectroscopy Substrates. *ACS Nano* **2018**, *12*, 8531–8539.

(5)   García de Arquer, F. P.; Mihi, A.; Konstantatos, G. Large-Area Plasmonic-Crystal–Hot-Electron-Based Photodetectors. *ACS Photonics* **2015**, *2*, 950–957.

(6)   Rawlings, C. D.; Kulmala, T. S.; Spieser, M.; Holzner, F.; Glinsner, T.; Schleunitz, A.; Bullerjahn, F. Single-Nanometer Accurate 3D Nanoimprint Lithography with Master Templates Fabricated by NanoFrazor Lithography. In *Novel Patterning Technologies 2018*; Panning, E. M., Sanchez, M. I., Eds.; SPIE, 2018; Vol. 10584, p 37.

(7)   Pourdavoud, N.; Wang, S.; Mayer, A.; Hu, T.; Chen, Y.; Marianovich, A.; Kowalsky, W.; Heiderhoff, R.; Scheer, H.-C.; Riedl, T.; Pourdavoud, N.; Hu, T.; Heiderhoff, R.; Riedl, T.; Wang, S.; Mayer, A.; Scheer, H.; Chen, Y.; Marianovich, A.; et al. Photonic Nanostructures Patterned by Thermal Nanoimprint Directly into Organo-Metal Halide Perovskites. **2017**.

(8)   Kang, S.-K.; Murphy, R. K. J.; Hwang, S.-W.; Lee, S. M.; Harburg, D. V.; Krueger, N. A.; Shin, J.; Gamble, P.; Cheng, H.; Yu, S.; Liu, Z.; McCall, J. G.; Stephen, M.; Ying, H.; Kim, J.; Park, G.; Webb, R. C.; Lee, C. H.; Chung, S.; et al. Bioresorbable Silicon Electronic Sensors for the Brain. *Nature* **2016**, *530*, 71–76.

(9)   Boutry, C. M.; Beker, L.; Kaizawa, Y.; Vassos, C.; Tran, H.; Hinckley, A. C.; Pfattner, R.; Niu, S.; Li, J.; Claverie, J.; Wang, Z.; Chang, J.; Fox, P. M.; Bao, Z. Biodegradable and Flexible Arterial-Pulse Sensor for the Wireless Monitoring of Blood Flow. *Nat. Biomed. Eng.* **2019**, *3*, 47–57.

(10)   Choong, C.-L.; Shim, M.-B.; Lee, B.-S.; Jeon, S.; Ko, D.-S.; Kang, T.-H.; Bae, J.; Lee, S. H.; Byun, K.-E.; Im, J.; Jeong, Y. J.; Park, C. E.; Park, J.-J.; Chung, U.-I. Highly Stretchable Resistive Pressure Sensors Using a Conductive Elastomeric Composite on a Micropyramid Array. *Adv. Mater.* **2014**, *26*, 3451–3458.

(11)   Ouyang, H.; Tian, J.; Sun, G.; Zou, Y.; Liu, Z.; Li, H.; Zhao, L.; Shi, B.; Fan, Y.; Fan, Y.; Wang, Z. L.; Li, Z. Self-Powered Pulse Sensor for Antidiastole of Cardiovascular Disease. *Adv. Mater.* **2017**, *29*, 1703456.

(12)   Gong, S.; Schwalb, W.; Wang, Y.; Chen, Y.; Tang, Y.; Si, J.; Shirinzadeh, B.; Cheng, W. A Wearable and Highly Sensitive Pressure Sensor with Ultrathin Gold Nanowires. *Nat. Commun.* **2014**, *5*, 3132.

(13)   Liu, Y.-F.; Feng, J.; Bi, Y.-G.; Yin, D.; Sun, H.-B. Recent Developments in Flexible Organic Light-Emitting Devices. *Adv. Mater. Technol.* **2019**, *4*, 1800371.

(14)   Chang, C.-Y.; Yang, S.-Y.; Huang, L.-S.; Hsieh, K.-H.; Daly, R. D. F.; Stevens, M. C.; Hutley, N. *Fabrication of Polymer Microlens Arrays Using Capillary Forming with a Soft Mold of Micro-Holes Array and UV-Curable Polymer References and Links*; 2006.

(15)   Wang, X.; Dong, L.; Zhang, H.; Yu, R.; Pan, C.; Wang, Z. L. Recent Progress in Electronic Skin. *Adv. Sci.* **2015**, *2*, 1500169.

(16)   Liu, Y.; Pharr, M.; Salvatore, G. A. Lab-on-Skin: A Review of Flexible and Stretchable Electronics for Wearable Health Monitoring. **2017**.

(17)   Schift, H. Nanoimprint Lithography: An Old Story in Modern Times? A Review. *J. Vac. Sci. Technol. B Microelectron. Nanom. Struct.* **2008**, *26*, 458.

(18)   Whitesides, G. M.; Grzybowski, B. Self-Assembly at All Scales. *Science* **2002**, *295*,

2418–2421.

(19)   Ahn, H.; Guo, L. J. High-Speed Roll-to-Roll Nanoimprint Lithography on Flexible Plastic Substrates**.

(20)   Lee, Y. S. (Yoon S. *Self-Assembly and Nanotechnology : A Force Balance Approach*; John Wiley & Sons, 2008.

(21)   Shen, X.; Song, C.; Wang, J.; Shi, D.; Wang, Z.; Liu, N.; Ding, B. Rolling Up Gold Nanoparticle-Dressed DNA Origami into Three-Dimensional Plasmonic Chiral Nanostructures. *J. Am. Chem. Soc.* **2012**, *134*, 146–149.

(22)   Macromol. Macromolecular Research Review DNA-Coated Microspheres and Their Colloidal Superstructures. **2018**, *26*, 1085–1094.

(23)   Hanske, C.; González-Rubio, G.; Hamon, C.; Formentín, P.; Modin, E.; Chuvilin, A.; Guerrero-Martínez, A.; Marsal, L. F.; Liz-Marzán, L. M. Large-Scale Plasmonic Pyramidal Supercrystals via Templated Self-Assembly of Monodisperse Gold Nanospheres. *J. Phys. Chem. C* **2017**, *121*, 10899–10906.

(24)   Yadong Yin, §; Yu Lu, §; Byron Gates, † and; Younan Xia†, *. Template-Assisted Self-Assembly: A Practical Route to Complex Aggregates of Monodispersed Colloids with Well-Defined Sizes, Shapes, and Structures. **2001**.

(25)   Dietrich, K.; Zilk, M.; Steglich, M.; Siefke, T.; Hübner, U.; Pertsch, T.; Rockstuhl, C.; Tünnermann, A.; Kley, E. Merging Top-Down and Bottom-Up Approaches to Fabricate Artificial Photonic Nanomaterials with a Deterministic Electric and Magnetic Response. *Adv. Funct. Mater.* **2019**, 1905722.

(1)   Hoole, A. C. F.; Welland, M. E.; Broers, A. N. Negative PMMA as a High-Resolution Resist - the Limits and Possibilities. *Semicond. Sci. Technol.* **1997**, *12*, 1166–1170.

(2)   Chou, S. Y.; Krauss, P. R.; Renstrom, P. J. *Nanoimprint Lithography*; 1996.

(3)   Dore, C.; Osmond, J.; Mihi, A. A Water-Processable Cellulose-Based Resist for Advanced Nanofabrication. *Nanoscale* **2018**, *10*, 17884–17892.

(4)   Matricardi, C.; Hanske, C.; Garcia-Pomar, J. L.; Langer, J.; Mihi, A.; Liz-Marzán, L. M. Gold Nanoparticle Plasmonic Superlattices as Surface-Enhanced Raman Spectroscopy Substrates. *ACS Nano* **2018**, *12*, 8531–8539.

(5)   García de Arquer, F. P.; Mihi, A.; Konstantatos, G. Large-Area Plasmonic-Crystal–Hot-Electron-Based Photodetectors. *ACS Photonics* **2015**, *2*, 950–957.

(6)   Rawlings, C. D.; Kulmala, T. S.; Spieser, M.; Holzner, F.; Glinsner, T.; Schleunitz, A.; Bullerjahn, F. Single-Nanometer Accurate 3D Nanoimprint Lithography with Master Templates Fabricated by NanoFrazor Lithography. In *Novel Patterning Technologies 2018*; Panning, E. M., Sanchez, M. I., Eds.; SPIE, 2018; Vol. 10584, p 37.

(7)   Pourdavoud, N.; Wang, S.; Mayer, A.; Hu, T.; Chen, Y.; Marianovich, A.; Kowalsky, W.; Heiderhoff, R.; Scheer, H.-C.; Riedl, T.; Pourdavoud, N.; Hu, T.; Heiderhoff, R.; Riedl, T.; Wang, S.; Mayer, A.; Scheer, H.; Chen, Y.; Marianovich, A.; et al. Photonic Nanostructures Patterned by Thermal Nanoimprint Directly into Organo-Metal Halide Perovskites. **2017**.

(8)   Kang, S.-K.; Murphy, R. K. J.; Hwang, S.-W.; Lee, S. M.; Harburg, D. V.; Krueger, N. A.; Shin, J.; Gamble, P.; Cheng, H.; Yu, S.; Liu, Z.; McCall, J. G.; Stephen, M.; Ying, H.; Kim, J.; Park, G.; Webb, R. C.; Lee, C. H.; Chung, S.; et al. Bioresorbable Silicon Electronic Sensors for the Brain. *Nature* **2016**, *530*, 71–76.

(9)   Boutry, C. M.; Beker, L.; Kaizawa, Y.; Vassos, C.; Tran, H.; Hinckley, A. C.; Pfattner, R.; Niu, S.; Li, J.; Claverie, J.; Wang, Z.; Chang, J.; Fox, P. M.; Bao, Z. Biodegradable and Flexible Arterial-Pulse Sensor for the Wireless Monitoring of Blood Flow. *Nat. Biomed. Eng.* **2019**, *3*, 47–57.

(10)   Choong, C.-L.; Shim, M.-B.; Lee, B.-S.; Jeon, S.; Ko, D.-S.; Kang, T.-H.; Bae, J.; Lee, S. H.; Byun, K.-E.; Im, J.; Jeong, Y. J.; Park, C. E.; Park, J.-J.; Chung, U.-I. Highly Stretchable Resistive Pressure Sensors Using a Conductive Elastomeric Composite on a Micropyramid Array. *Adv. Mater.* **2014**, *26*, 3451–3458.

(11)   Ouyang, H.; Tian, J.; Sun, G.; Zou, Y.; Liu, Z.; Li, H.; Zhao, L.; Shi, B.; Fan, Y.; Fan, Y.; Wang, Z. L.; Li, Z. Self-Powered Pulse Sensor for Antidiastole of Cardiovascular Disease. *Adv. Mater.* **2017**, *29*, 1703456.

(12)   Gong, S.; Schwalb, W.; Wang, Y.; Chen, Y.; Tang, Y.; Si, J.; Shirinzadeh, B.; Cheng, W. A Wearable and Highly Sensitive Pressure Sensor with Ultrathin Gold Nanowires. *Nat. Commun.* **2014**, *5*, 3132.

(13)   Liu, Y.-F.; Feng, J.; Bi, Y.-G.; Yin, D.; Sun, H.-B. Recent Developments in Flexible Organic Light-Emitting Devices. *Adv. Mater. Technol.* **2019**, *4*, 1800371.

(14)   Chang, C.-Y.; Yang, S.-Y.; Huang, L.-S.; Hsieh, K.-H.; Daly, R. D. F.; Stevens, M. C.; Hutley, N. *Fabrication of Polymer Microlens Arrays Using Capillary Forming with a Soft Mold of Micro-Holes Array and UV-Curable Polymer References and Links*; 2006.

(15)   Wang, X.; Dong, L.; Zhang, H.; Yu, R.; Pan, C.; Wang, Z. L. Recent Progress in Electronic Skin. *Adv. Sci.* **2015**, *2*, 1500169.

(16)   Liu, Y.; Pharr, M.; Salvatore, G. A. Lab-on-Skin: A Review of Flexible and Stretchable Electronics for Wearable Health Monitoring. **2017**.

(17)   Schift, H. Nanoimprint Lithography: An Old Story in Modern Times? A Review. *J. Vac. Sci. Technol. B Microelectron. Nanom. Struct.* **2008**, *26*, 458.

(18)   Whitesides, G. M.; Grzybowski, B. Self-Assembly at All Scales. *Science* **2002**, *295*, 2418–2421.

(19)   Ahn, H.; Guo, L. J. High-Speed Roll-to-Roll Nanoimprint Lithography on Flexible Plastic Substrates**.

(20)   Lee, Y. S. (Yoon S. *Self-Assembly and Nanotechnology : A Force Balance Approach*; John Wiley & Sons, 2008.

(21)   Shen, X.; Song, C.; Wang, J.; Shi, D.; Wang, Z.; Liu, N.; Ding, B. Rolling Up Gold Nanoparticle-Dressed DNA Origami into Three-Dimensional Plasmonic Chiral Nanostructures. *J. Am. Chem. Soc.* **2012**, *134*, 146–149.

(22)   Macromol. Macromolecular Research Review DNA-Coated Microspheres and Their Colloidal Superstructures. **2018**, *26*, 1085–1094.

(23)   Hanske, C.; González-Rubio, G.; Hamon, C.; Formentín, P.; Modin, E.; Chuvilin, A.; Guerrero-Martínez, A.; Marsal, L. F.; Liz-Marzán, L. M. Large-Scale Plasmonic Pyramidal Supercrystals via Templated Self-Assembly of Monodisperse Gold Nanospheres. *J. Phys. Chem. C* **2017**, *121*, 10899–10906.

(24)   Yadong Yin, §; Yu Lu, §; Byron Gates, † and; Younan Xia†, *. Template-Assisted Self-Assembly: A Practical Route to Complex Aggregates of Monodispersed Colloids with Well-Defined Sizes, Shapes, and Structures. **2001**.

(25)   Dietrich, K.; Zilk, M.; Steglich, M.; Siefke, T.; Hübner, U.; Pertsch, T.; Rockstuhl, C.; Tünnermann, A.; Kley, E. Merging Top-Down and Bottom-Up Approaches to Fabricate Artificial Photonic Nanomaterials with a Deterministic Electric and Magnetic Response. *Adv. Funct. Mater.* **2019**, 1905722.

SECTION II

ASYMMETRIC PLASMONIC NANOSTRUCTURES

ASYMMETRIC PLASMONIC CRYSTALS WITH TUNABLE OPTICAL PROPERTIES

The capability to manage light at the nanoscale offered by metal nanostructures brought new opportunities for imaging, biomedicine, sensing, light absorption and emission. Plasmonic materials enhance several hundreds of times the intensity of the incoming electric field confining light at the nanoscale. However, an enhanced light matter interaction could imply the capability to exert control over the properties of confined electromagnetic wave, namely their phase, intensity, direction and polarization. In this context, recent plasmonic devices enable the control of different properties of electromagnetic waves squeezed down to the nanoscale, namely their phase, intensity direction and polarization. The optical response of the metallic nanostructures can be engineered to exhibit exciting phenomena such as negative refractive index, optical chirality, subwavelength imaging and more. As the optical properties increase in complexity, the nanostructures become more demanding in terms of nanofabrication and hence less scalable. This work presents a straightforward method to produce large area asymmetric plasmonic nanostructures with sub-micrometer periodicity by combining nanoimprint lithography and oblique angle metal evaporation. The combination of scalable top down and bottom up approaches results in a variety of asymmetric plasmonic crystals whose final optical response can be tuned by the geometry of the original nanoimprinted structure and the tilting angle at which the metal is evaporated. We have fabricated ordered arrays of asymmetric wedges, nanogaps and chiral nanostructures, achieving polarization sensitive optical properties and selective enhanced light emission over large areas.

~ ● ~

3.1 INTRODUCTION

Metal nanostructures can be engineered to sustain a wide variety of resonances. From the simplest localized surface plasmon resonance observed in metal colloids[1], until the more complex magnetic and electric resonances sustained by metamaterials.[2,3] The diverse optical properties sustained by nanostructured metal architectures have led to advances in biosensing[4], photovoltaics[5,6], imaging[7], and lighting[8]. However, the fabrication of plasmonic architectures sustaining complex optical responses becomes more cumbersome and therefore, less scalable. A particular example is that of plasmonic asymmetric nanostructures. These can exhibit many interesting properties, such as trapped-mode resonances,[9] which are originated by a planar metamaterial composed of asymmetrically split rings and they exhibit unusually strong high-Q resonances. These architectures have shown multiple uses in sensing[10], lasing[11,12] and induced transparency.[13,14] They can also present chiral behavior, which is of great interest for enantiomer separation[15] and polarization sensitive photocatalysis.[16] Furthermore, asymmetric plasmonic arrays embedding low symmetry nanocavities can be used to tailor the lasing behavior of a dye by simply changing the pump polarization achieving a double wavelength laser in one device.[17,18] Thus, asymmetry gives rise to complex optical properties which open to the possibility to control phase, intensity, direction and polarization of light, and leads to the development of plasmonic systems which are at the forefront of recent scientific breakthroughs[19].

Despite all these exciting applications, photonic architectures with broken symmetry are still challenging to use at visible frequencies, especially in a scalable fashion. In fact, all these structures depend heavily on nanoscale engineering in order to achieve high homogeneity over large areas making possible their implementation into real devices. In general, the fabrication process of most of the current plasmonic architectures relies on electron beam lithography or other low throughput techniques hindering the use of these plasmonic systems in many applications, hence the great interest in scalable nanofabrication techniques. Some of the most popular techniques to produce

large area photonic nanostructures are; nanospheres lithography (NSL),[20] interference lithography (IL)[21] and nanoimprinting lithography (NIL).[22] These lithography, however, tend to produce symmetric periodic nanostructures which limit the number of optical properties accessible. The symmetry of the original array can be broken at the metallization stage, for instance by recurring to the oblique angle deposition (OAD) of metals, opening up a plethora of possibilities. The combination of NSL with OAD has led to asymmetric plasmonic nanostructures[23,24], split ring resonators,[25] chiral nanostructures[26,27] and more.[28,29] However, in the case of NSL, this technique produces only hexagonal arrays whose large scale homogeneity is severely affected by the presence of cracks and defects of the final assembly, which in turn deteriorates the overall optical response and broadens the plasmonic resonances. Alternatively, NIL is the technique of preference for the up scaling of nanostructures with excellent quality, because it is roll to roll compatible and it has an excellent resolution without requiring complex optical set ups.[30,31] NIL utilizes pre-patterned elastomeric molds as printing stamps, in which the geometry, feature depth and lattice parameter can be varied by changing the original master.

The use of a mixed top down/bottom up approach, respectively NIL and OAD, has many advantages for instance, the great variety of nanoimprinted structures available, from hole arrays to pillar or pyramids, arranged into squared, triangular or other geometries,[21] together with the possibility to break the symmetry that allows the fabrication of half metallic pillars, nanowedges or nanogaps arrays. However, the versatility and potential of this approach has only been hinted by a few reports in the literature, leading to chiral structures and SERS substrates.[32,33]

In this chapter, I will present a complete description of the fabrication process, highlighting the key steps to achieve reproducibility and reliability of asymmetric plasmonic structures as well as the parameters which allow tuning the optical response achieving homogeneous polarization sensitive optical response over 1 cm^2 area. A complete case of study of the different fabrication

parameter will highlight the best condition to achieve intense optical anisotropy both with linear and circular polarized light.

We use these architectures to produce surface enhanced fluorescence whose signal corroborate the control over the polarization of the light at the nanoscale. In particular, we tested metallic nanogaps arrays where both the magnitude of enhancement and large scale signal homogeneity paves the way towards the implementation of these nanostructures into real devices. Furthermore this study opens the possibility to further tailor the system exploiting the possibility to control the concentration of light not only by its frequency but also by its polarization.

3.2 FABRICATION

Asymmetric nanostructures were fabricated following a tunable and cheap method that yields high throughput and allows wide variety of geometries with different aspect ratio and tunable crystal lattice. The process involves a merger of bottom up and top down approaches and is comprised by three main steps: i) Molds fabrication; ii) Nanoimprint; iii) Oblique angle metal deposition.

- *Molds fabrication*

The mold fabrication is the first most crucial step of the entire process; it imposes and defines the nanostructure geometry and is responsible of the homogeneity of the crystal structure. We took advantage of hybrid molds that, as explained in 2.2.3, allow achieving good resolution thanks to a thick soft PDMS attached over a thin layer of hard PDMS.

The one centimeter square patterns have been purchased from Naitec© and replicated after a silanization step that provide an anti-sticking layer and ensure the correct demolding of the PDMS. Part of the work involves the tuning of the features depth of the holes arrays so we fabricated a new batch of silicon masters with progressively decreasing depth. We used NIL followed by reactive ion etching (RIE). Briefly, the SU8 2000.5 (Microchem) photoresist was spin coated to achieve a layer thickness about 350-400 nm and imprinted using a hot embossing technique. Later, a two-step Reactive Ion Etching (RIE) process

was used to transfer the pattern to the silicon substrate: first, a O2 descumming treatment is used to etch the residual 50-100 nm layer of resist under the imprinted holes (O2 40 sccm, pressure 25 mTorr, RIE power 50 W, ICP power 1500 W and etching rate ~800 nm/min), and second, the exposed Si is etched with CHF3 and SF6 (CHF3 50 sccm, SF6 15 sccm, pressure 12 mTorr, RIE power 150 W, ICP power 0 W, and etching rate 60 nm/min). The Si processing time was varied to achieve masters with hole depths of 120 nm, 80 nm, 60 nm. A final descumming step was used to remove entirely the remains of resist.

- *Automatized Nanoimprint process*

We choose the SU8 2000.5 photoresist as a substrate for our final device. SU8 have excellent chemical and thermal stability as well as the easy and fast thermal nanoimprinting process provide high throughput. After the deposition of a 600 nm thick layer of SU8 on a silicon or glass substrate we load the semi-automatic imprinting device with the system depicted in Figure 3.1. The CNI nanoimprinting tool gives us the possibility to adjust pressure and temperature over the whole process as show in Figure 3.2. These controlled protocols lead to a reliable hot embossing process with high inter batch homogeneity. Briefly, we heat the sample above the glass transition temperature of the photo resist and then slowly apply pressure giving time to the resist to flow inside the structures leading to a homogeneous centimeter scale imprinting. The substrate is then cooled down to 40°C and the PDMS stamp is slowly demolded in order to do not damage the pattern.
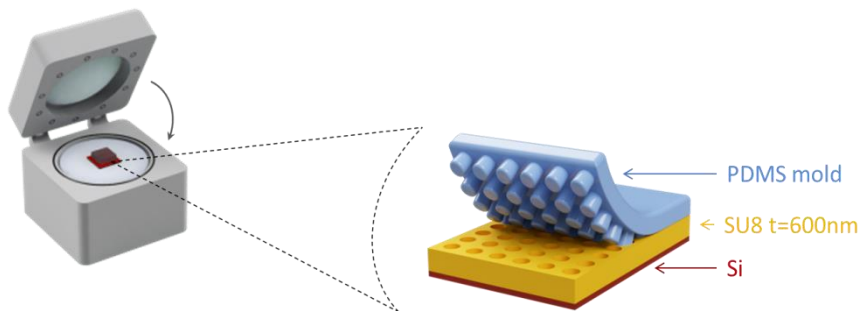

Figure 3.1 Schematic of the imprinting machine and soft nanoimprinting lithography which lead to holes array. The inset show the system loaded on the imprinting machine.

The nanostructures samples are then exposed to UV light and baked at 150°C for 30 min. This process leads to hard nanostructures featuring either holes or pillar arrays.
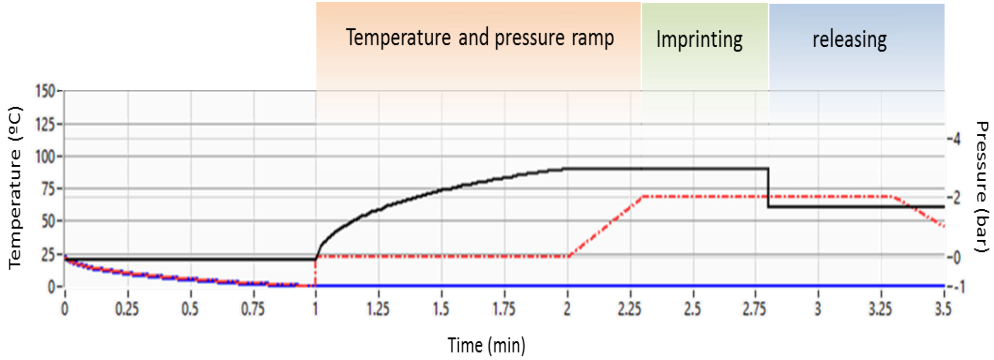

Figure 3.2. Nanoimprint setups with controlled pressure and temperature. A first heating steps followed by a pressure ramp. The pressure is applied slowly in order to do not move the stamp during the process. Subsequently pressure is maintained to assure the complete filling of the PDMS stamp features. The releasing step brings the temperature back to the ambient value and lift-off is then performed manually.

- *Oblique angle metal deposition*

Deposition of metals by thermal evaporation is a well know technique to create metallic or oxide films and provides a non-conformal deposition over large area (Figure 3.3).
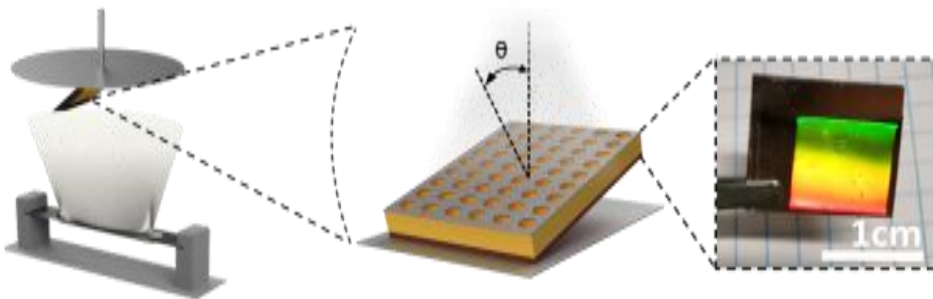

Figure 3.3 Schematic of the Evaporation setup. The inset photography shows a real image of the as prepared plasmonic crystals highlighting the homogeneity over large area.

The 2D photonic crystals were mounted on a custom-made tilted holder to achieve progressive breaking of symmetry during the evaporation of silver. Thus, a tilt of the substrate holder will introduce a shadowed region in respect to flat configuration. The tilted metal evaporation results in asymmetric nanostructures that vary in shape and dimension as the azimuthal angles of the sample increase as depicted in Figure 3.4a-c.
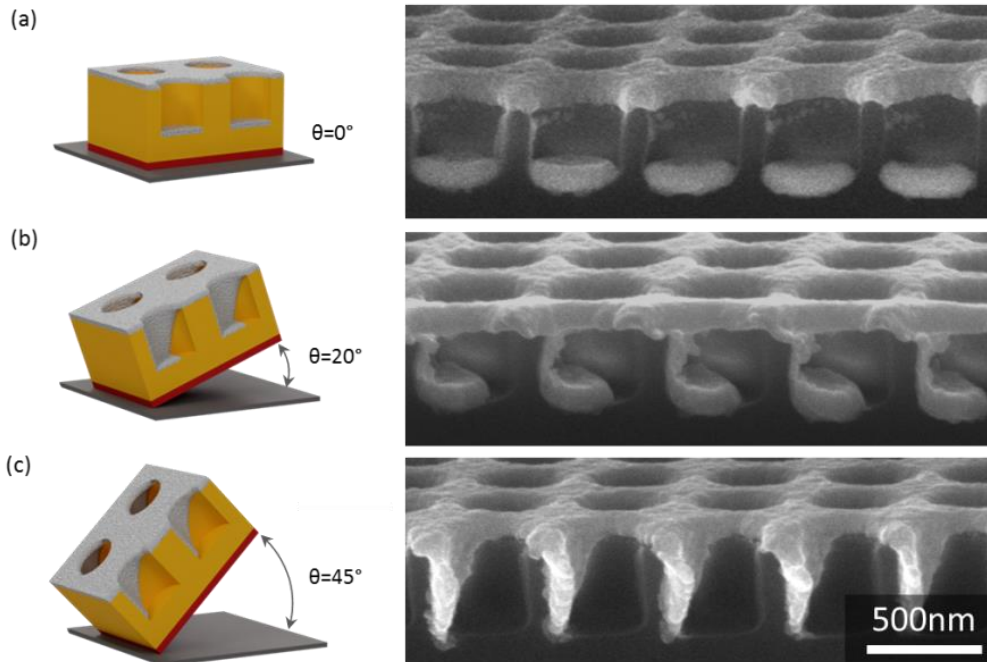

Figure 3.4 a-c) Effect of the subsequent symmetry breaking via tilted evaporation. 3D sketch of the tilted sample holder (left), SEM micrograph cross section of the relative structures (right).

The evaporation setup influences the final structure and its optical response. Thus, in order to achieve sharp and reproducible nanostructures it has to be finely optimized. The alignment of the substrates to the metal source avoids the extra tilt given by the azimuthal angle of the evaporation cone (Figure 3.5a). Moreover, while standard evaporation protocols involve rotating the sample holder, in our case the holder has to be kept still in order to do not modify the angle of incidence obtaining sharper features. The optical properties along with the overall roughness are affected by the deposition setup. Concretely the reflection profiles depicted in Figure 3.5b-d show different shapes where a

sharpening of the wedges is accompanied by the arising of new resonances between 800 and 900 nm together with an overall increase of resonances intensity.
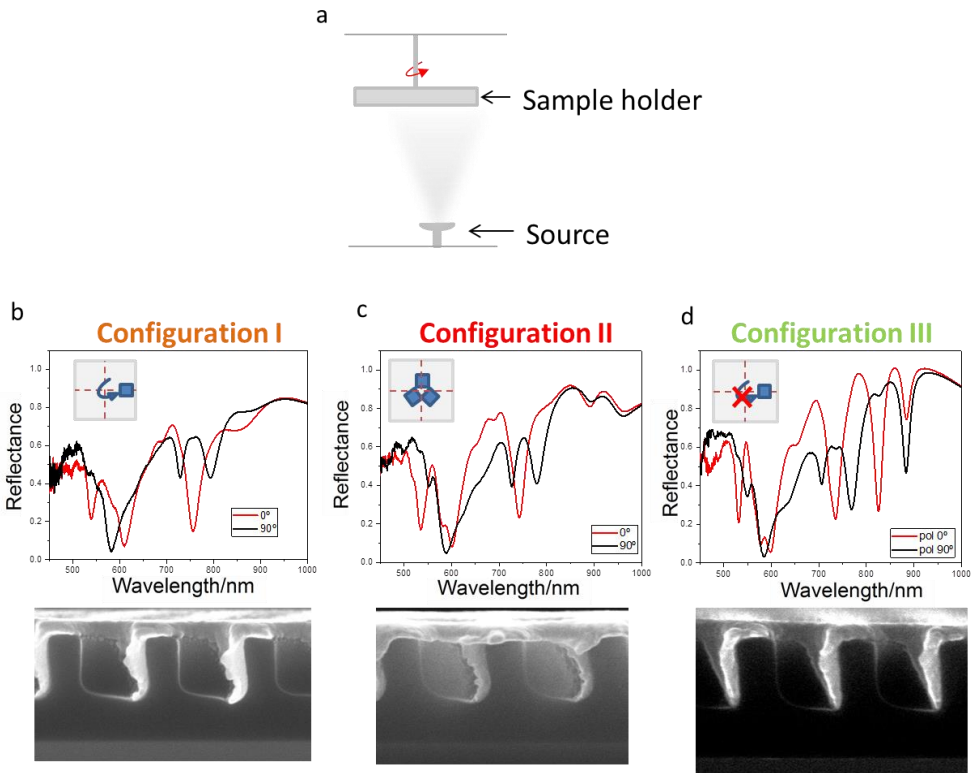

Figure 3.5. Optical and morphological properties of nanoholes arrays coated with 75 nm of silver evaporated at 45° respect to the source under three configurations. Configuration (I) samples are placed 2.5 cm from the center of the evaporation holder 15 cm diameter under a rotation of 20 rpm. Configuration (II) samples are placed at the center of the evaporator holder with a rotation of 20 rpm active. Configuration (III) samples are placed directly over the source, at 4cm from the center of the holder plate without rotation. This latter configuration led to the sharpest features and is the one used throughout this work.

Concretely the reflection profiles depicted in Figure 3.5b-d show different shapes where a sharpening of the wedges is accompanied by the arising of new resonances between 800 and 900 nm together with an overall increase of resonances intensity. This can be attributed to the dependence of plasmon to surface roughness which broad and damp surface plasmon resonances.[34,35]

3.3   TUNING THE OPTICAL RESPONSE

This fabrication process allows the easy control over several parameters both during the NIL process and the metallization stage. This study investigates how the asymmetry generated during oblique angle deposition affect the overall optical response. At the end of this discussion we come up with several plasmonic crystals that can be used in enhanced spectroscopy in the visible and NIR range.

3.3.1   Holes array

The first geometry we will study is the square array of 300 nm holes. We will determine the influence of the fabrication parameter on morphology and optical properties.

- *Influence of tilt angle during metal evaporation*

The first parameter is the tilting of the sample. Figure 3.6 shows SEM images and reflection profiles of the plasmonic crystals fabricated under normal evaporation conditions (0º tilt angle). The reflectance in both linear polarizations shows only slight differences accounting for the inherent asymmetries of the thermal evaporation set up. However, as we increase the tilting angle there is a degeneracy breaking of the resonances for each linear polarization, evidenced as we increase the tilt angle from 0 º to 20º and even more in the case of 45º.

Tilted evaporation on the photonic crystals results in strong dips in reflection that follow the loss of symmetry of the unit cell. Through this fabrication method we can control resonances degeneration while introducing a polarization sensitive response. The possibility to further increase the modes tunability were explored by studying the influence of lattice parameter, keeping the tilt angle fixed.
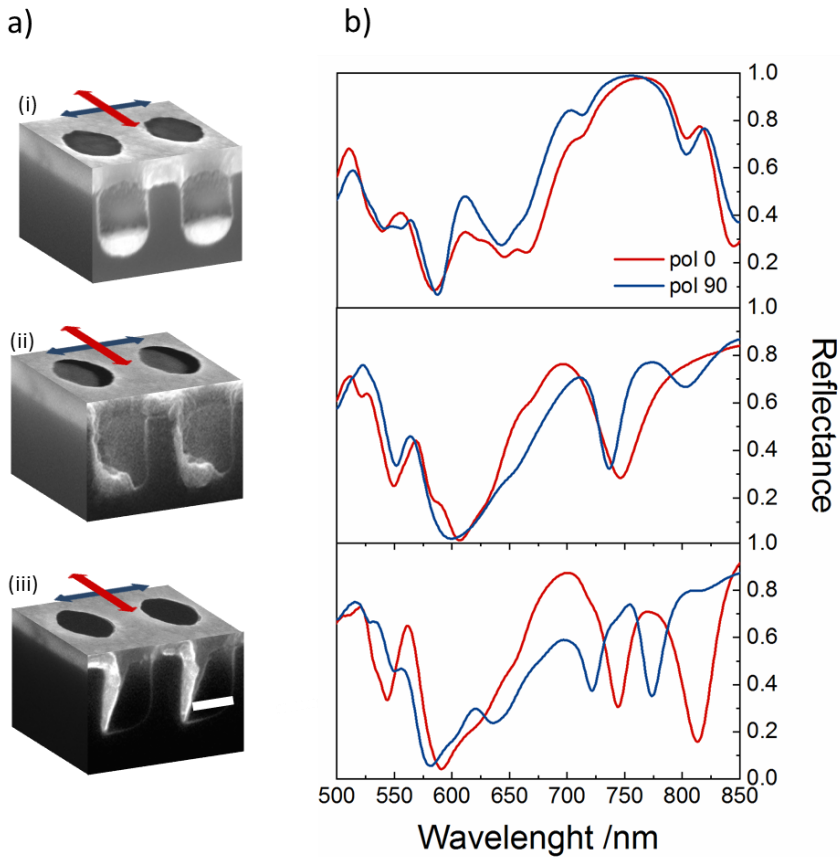
Figure 3.6 Optical characterization of asymmetric plasmonic crystals (Square array of holes with diameter 300 nm and depth 350 nm) with lattice parameter 500 nm, for three different tilt angles (0º, 20º and 45º) of Ag evaporation (75 nm). The linearly polarized reflectance spectra were taken along the two main crystal directions of the nanostructure through a 4X objective, averaging an area of 900 x 900 μm². The samples were coated with 75 nm of Ag and showed negligible transmission. The right column (a) illustrates the plasmonic crystal geometry inspected in each case and the orientation of the electric field. Scale bar 250 nm.

- *Influence of the lattice parameter*

The second parameter is the lattice geometry, in particular we wanted to study how the lattice parameter affects the mode splitting and in which way it can be used to tune the optical response. The tilt was fixed at 45 degree for each sample since this condition ensures a strong mode splitting. In principle, by changing lattice constant we modify the diffraction condition which could affect the resonances in our plasmonic crystal. This effect is visible in Figure 3.7, where a sweep of lattice parameters produces changes in the reflection

response. The lattice parameter of the fabricated photonic crystal determines the spectral position of the shifted resonances, in the studied cases being at 550 - 700 nm range for L= 400 nm (Figure 3.7d), at the 700 – 850 nm range for L= 500 nm samples (Figure 3.7e) and at the 800-900 nm range for L=600nm samples (Figure 3.7f). Therefore, our system also allows an easy tuning of the spectral position of the resonances by changing its geometrical parameters.
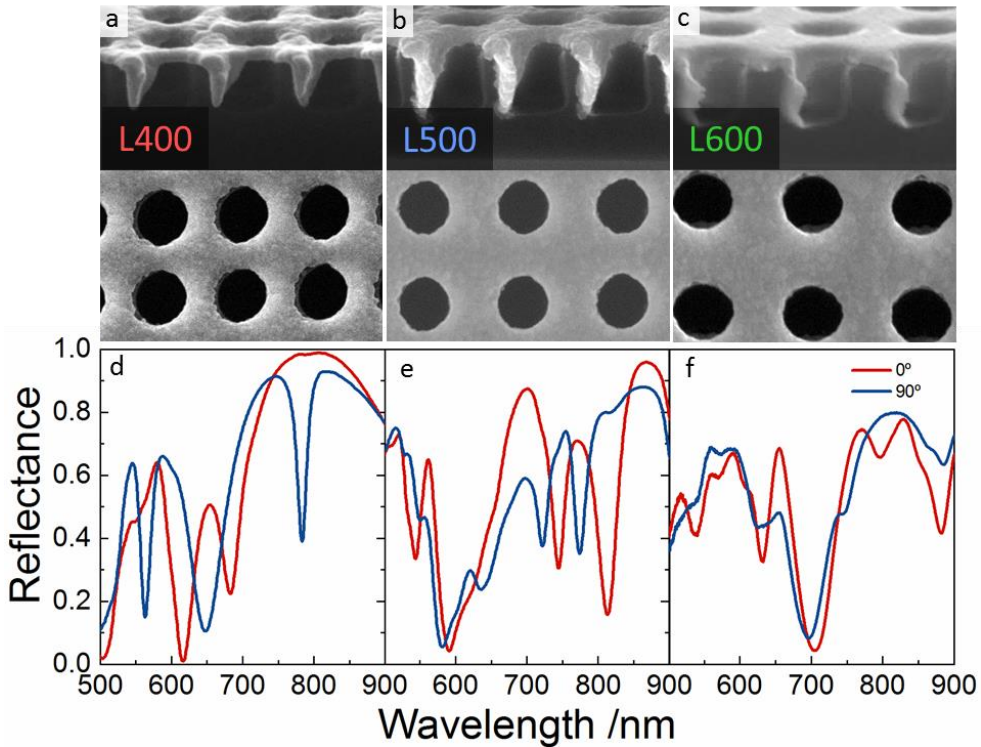

Figure 3.7 SEM images and optical properties of samples covered with 50nm of silver. The lattice parameter is tuned from 400 nm to 600 nm (a-c). The optical properties show the loss of degeneracy for sample L=400 nm and L=500 nm (d,e) while the further increase of the lattice (f) do not create an intense polarization sensitive optical response in the visible.

These results give useful insights on how the geometry of the photonic crystal influences the modes splitting. Concretely if we look at the visible range, we note that for the sample L600 the loss of degeneration is not as evident as in the two other cases (Figure 3.7f). This could be ascribed to the effect of the lattice parameter that shifts the resonances toward the near infrared. Instead the L=500 nm and L=400nm sample gives resonances in the visible.

- *Influence of the feature depth*

Combined NIL/OAD approach enabled the fabrication of nanogaps or nanoapertures in metals thus creating intense electromagnetic field localization. In the literature, nanometric gaps between metallic particles and antennas resulted in strong field confinement with great relevance for photoluminescence enhancement.[36–38] Scaling up this geometry for its implementation in optoelectronic devices is quite challenging since it requires both great precision and uniformity over large areas in order to obtain a homogeneous response over the entire device. To produce an array of nanogaps fulfilling these requirements, we employed the same recipe as before, but using PDMS stamps with shallower holes of 120 nm, 80 nm and 60 nm and lattice of 500nm.
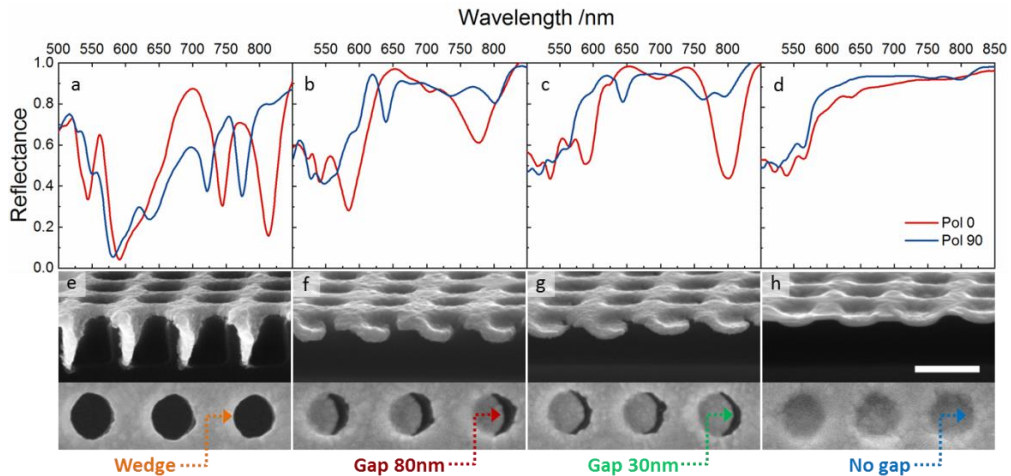

Figure 3.8 Evolution of the optical properties and SEM micrographs of plasmonic structures fabricated by tilted metal evaporation on NIL samples with decreasing feature depth. The rest of the structural parameters are fixed at 500 nm lattice parameter, 45º tilt angle, and 75 nm thickness of Ag. Polarization resolved reflectance of wedges array (a), 80nm nanogaps array (b), 30nm nanogaps array (c), square array of holes (d). Bottom images, SEM micrograph showing the decrease of the structure tuning. The depth of the holes is 350 nm (e), 120 nm (f), 80 nm (g) and 60 nm (h). Scale bar is500 nm.

These structures render arrays of nanogaps once coated with 75 nm of silver at a tilt angle of 45º (Figure 3.8). While the samples with the original hole depth (350 nm) only present a wedge of silver (Figure 3.8e), samples with 120 and 80

nm deep holes present homogeneous nanogaps arrays of 80 and 30 nm, respectively (Figure 3.8f, g). Finally, in the 60 nm hole depth samples, no gaps are appreciated (Figure 3.8h). In the two geometries with the nanogaps a resonance at 775 nm appears when impinging with a 90º linearly polarized light. This resonance is not present in the structure with no openings; therefore, we attribute it to the silver nanogaps (Figure 3.8a-d).

- *Multiple depositions*

The degree of asymmetry can be increased by subsequent evaporations and can lead to more complex nanostructure with more polarization selective optical properties.

Double deposition

The single wedge array produces a resonance splitting and induces optical anisotropy. This latter behavior can be enhanced by increasing the asymmetry; hence a wedge-like array with lattice of 500nm and deposited at 45° has been chosen to perform a second round of evaporation with the same tilt angle but rotating the axis normal of its surfaces by 180˚. This process leads to the fabrication of double wedges arrays. Figure 3.9a show a side view of those nanostructures revealing how this double deposition created two asymmetric wedges while from the top view in the inset in Figure 3.9c-d is clear that the rounded shape of the initial imprinting is lost giving space to eye like ovoid shapes. In the sought of asymmetric optical response those nanostructures revealed strong polarization dependent reflection which is attributed to the asymmetric wedges. On the one hand, when impinging with linearly polarized light parallel to the wedges (red lines), the fields likely do not see any feature and the sample act as a mirror. In the other hand the perpendicular polarized light (black lines) can excite electron oscillation that can extend down to the wedge's tips leading to a drastic reduction of the reflected light though coupling with plasmonic modes of the substrate Figure 3.9b. This architecture also shows a polarization dependent structural color. Optical microscope photographs of the samples under normal incidence clearly show the change from green to orange, as the polarization changes from parallel to normal to the wedge (Figure 3.9c-d).
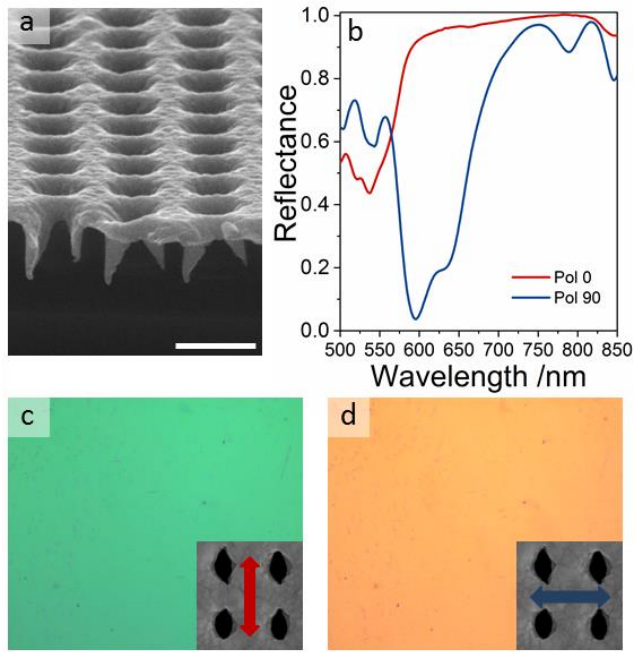
Figure 3.9 Asymmetric plasmonic crystal achieved after two consecutive 45º tilt metal evaporation. a) SEM cross sectional image from the architecture, scale bar 500 nm. b) Linearly polarized reflectance spectra were taken along the two main crystal directions of the nanostructure through a 4X objective, averaging an area of 900 x 900 μm². c-d) Photographs of the sample under orthogonal linear polarizations obtained with an optical microscope. The insets illustrate the plasmonic crystal geometry inspected in each case.

Triple deposition

The maximum asymmetry is achieved with three subsequent OAD processes. In this case, we end up with no mirror planes inside the unit cell introducing chiral information in the structure. This process involves three subsequent metal evaporations where the tilt angle was fixed at 45° but the rotation of the axis normal to the sample surface is 0° for the first round, 45° for the second round and finally 90° for the last round of metallization. The rotation sense (left handed or right handed) during the evaporation process define the enantiomer direction. Figure 3.10d-e shows the geometrical asymmetry of the two enantiomers highlighting the chiral shape of the asymmetric wedges. The samples were fabricated on glass substrate and the final silver thickness was kept below 45nm in order to do not loss signal in transmission.
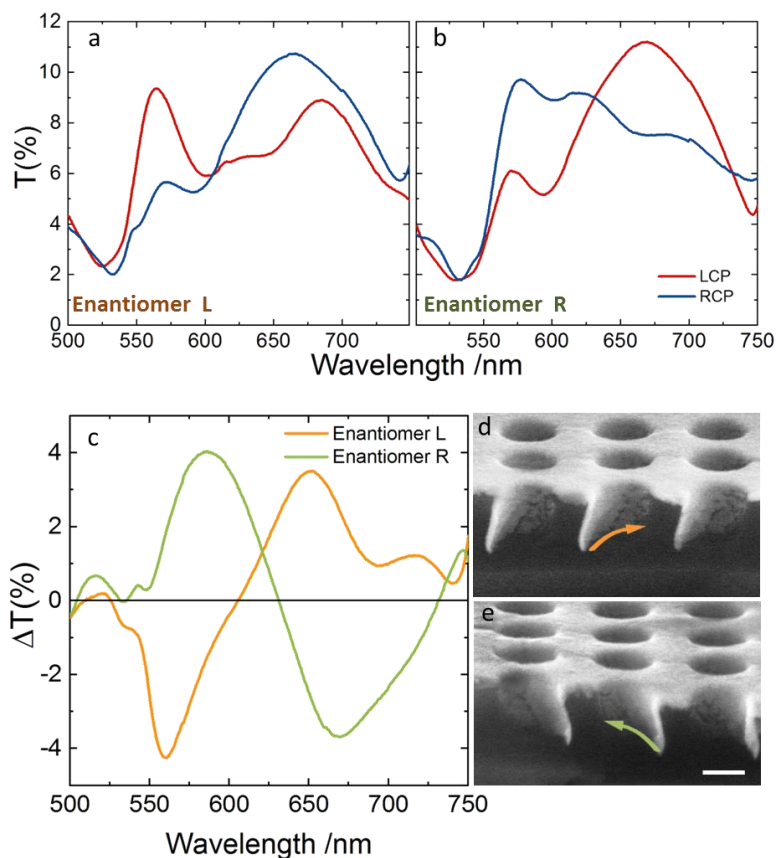
Figure 3.10 SEM images and optical characterization of opposite plasmonic enantiomers fabricated by NIL and OAD. a-b) Transmission spectra of enantiomer R and L. c) Transmission dichroism for each samples. D-e) SEM images of both L and R enantiomer highlighting the wedge directions. Scale bar 200nm.

These samples were characterized by a lab made CD micro spectrometer where the circular polarization is induced by a quarter wave plate.

3.3.2 Pillars arrays

In this section, I illustrate how this technique can also be applied to geometries such as pillars. However, this avenue was not fully explored due to the lack of intense polarization depend optical response. Figure 3.11a-c shows pillars arrays lattice parameter of 500 nm mounted respectively on a 0º, 20º and 45º tilted sample holders and covered with 50 nm of silver. This setup leads to half metallic pillars intercalated with lines and are expected to show polarization

dependent optical properties as the holes samples. However, even though the tilted evaporation induces geometric anisotropy, the plasmonic structures do not show intense and relevant resonance splitting as it was observed before with holes samples (Figure 3.11d-f). Furthermore, the differences in optical properties for parallel and perpendicular polarization are not pronounced for each of the samples studied.
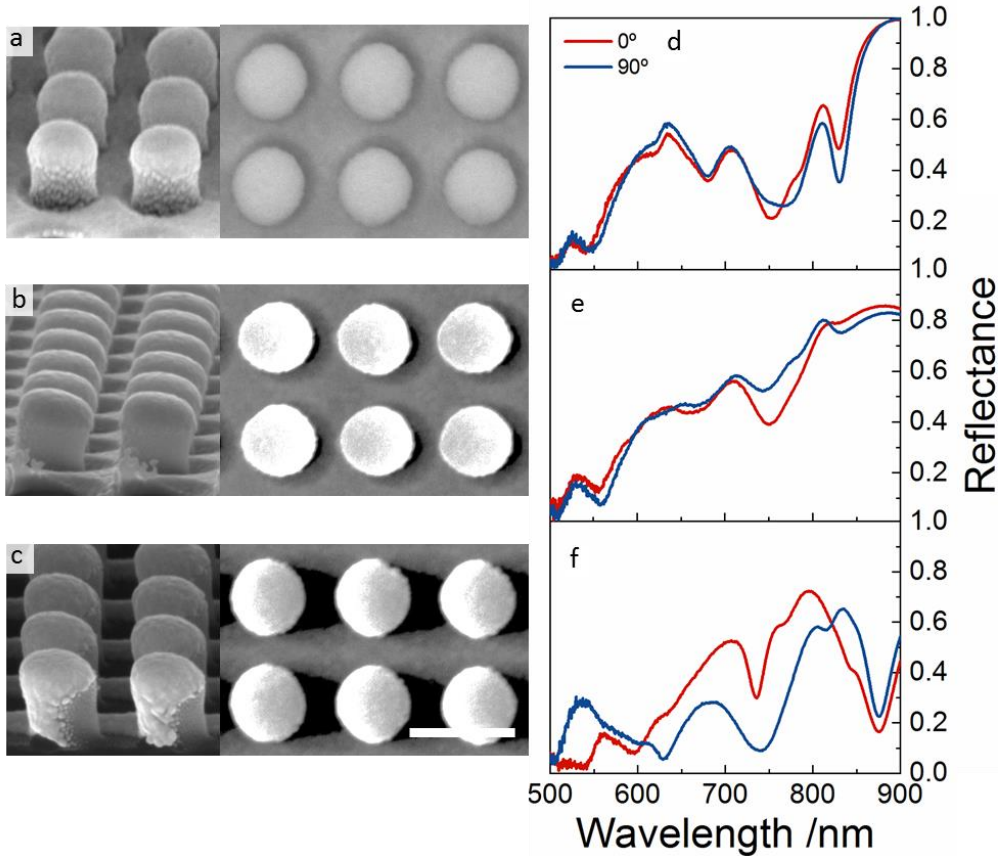

Figure 3.11. SEM micrograph of pillars array with lattice parameter of 500nm and different tilt angle evaporation, (a) 0º (b) 20º (c) 45º. The half metallic pillar shape is clearly visible for the maximum tilt along with metallic stripes in between the array. d-e) Polarization resolved reflection of the samples that unveil the poor degeneration loss along the increased asymmetry. Scale bar 500nm.

In conclusion this final result stresses the importance of the nanostructure design since not every asymmetric plasmonic object show intense polarization

dependent optical properties in the far field so extensive efforts shall be spent to engineer and seek the correct design.

3.4   APPLICATION: ENHANCED LIGHT MATTER INTERACTION

In what follow the application of asymmetric plasmonic crystals will be discussed studying the selective enhancement of photoluminescence. The experimental characterization along with theoretical simulations will unveil the effect of the lattice geometry and asymmetric unit cell on the emission enhancement.

3.4.1   Polarization selective fluorescence enhancement

Previous studies demonstrated that surface plasmon resonances can both enhance and/or shape the emission form dyes. Furthermore, in the peculiar case of plasmonic crystals the emission direction can be easily controlled by engineering the nanostructure.[39] In some cases, the angularly resolved photoluminescence signal strictly follows the Rayleigh anomalies typical in plasmonic and photonic nanostructures.[40,41]

Our goal in this work is to match the emitted light with a plasmonic resonances leading to enhanced fluorescence. Furthermore, since the structures fabricated with NIL/OAD show polarization sensitive optical properties the final target will be to add control over polarization of the emitted light extending the enhancement concept from the increase of the intensity of emitted light to the control over its properties.

For surface enhanced fluorescence experiments we will use nanogaps arrays introduced in Figure 3.8 since nanometric gaps lead to a strong field confinement useful for emission enhancement.

- *Dye-coated plasmonic crystals*

Surface enhanced florescence (SEF) relies on the interaction of plasmonic resonances with molecular dyes. Other factors such as the vicinity to metal surface, the spectral matching of the emission with the cavity frequency, and

the dispersing media contribute to the overall emission enhancement or even quenching.

In order to study how our asymmetric plasmonic crystals can enhance the photoluminescence, we chose to coat the samples with an organic dye embedded in a polymer matrix. A mixture of Atto 655 dye ($3 \bullet 10^{-5}$ M) and polyvinyl alcohol (PVA) was diluted in DMSO and spin coated on top of the samples producing a homogenous film of 250 nm thickness. Embedding the molecular dye in a polymer matrix we increase its stability while decreasing the intermolecular quenching.[42]

In this study, the range of interest is comprised between 680 and 800 since the ATTO 655 emission has its main peak at 677 nm and shows a long tail up to 800 nm (Figure 3.12).
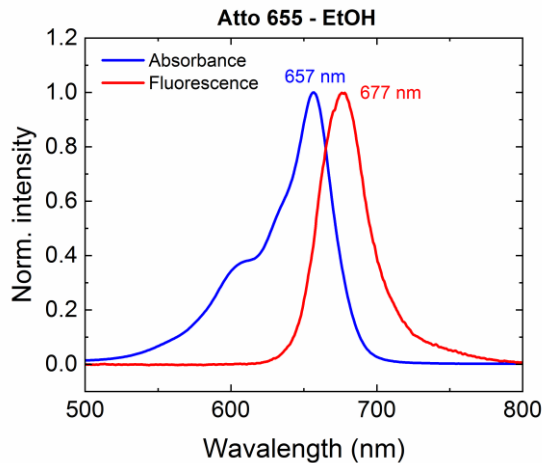

Figure 3.12. Absorbance and emission profile of Atto 655 in ethanol solution

One important factor is the refractive index of the system ones covered with the polymer. The dilectric enviroment of our plasmonic structures changes, causing a shift of the plasmonic resonances. Thus, further optical charaterization of the coated structures is necessary to detect the resonace mode that could affect the emission process.

- *Optical properties of dye coated plasmonic crystals*

The refractive index increases from 1 (air) to 1.47 (PVA) leading to a significant red shift of the resonances. We used plasmonic crystal with lattice 500 nm and 120 nm, 85 nm depth that led to nanogaps array of 80 nm 30 nm. The shallow features allow conformal coating of the polymer/dye while intense electromagnetic field localization can be achieved within the nanogaps. Figure 3.13 shows the optical properties of a 30nm gap sample with and without the PVA layer. The optical properties of coated structures are perfectly tailored to interact with the dye emission.
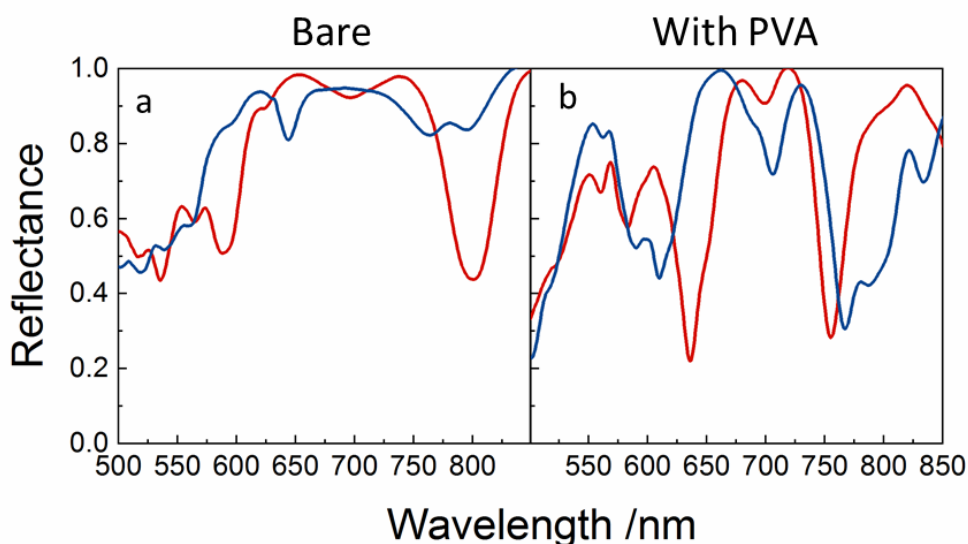

Figure 3.13. The optical properties of bare 30nm gaps array on the left and coated samples on the right.

- *Photoluminescence microspectroscopy setup*

The general setup used in this experiment is described por encima de I, however in order to perform polarization resolved measurements the setup was slightly modified. In order to be consistent with the setup used for the optical characterization, we carried out measurements with the same objective whose numerical aperture is 0.1. This setup avoids the angular dispersion of lattice modes which introduces a resonance broadening.[35] The optical path comprised a polarizer ($\lambda/2$) and an analyzer, both fixed at the same orientation

(Figure 3.14) in order to get rid of the different sensibility of the filters and gratings to the polarization. The polarization resolved PL spectroscopy was performed rotating the sample.
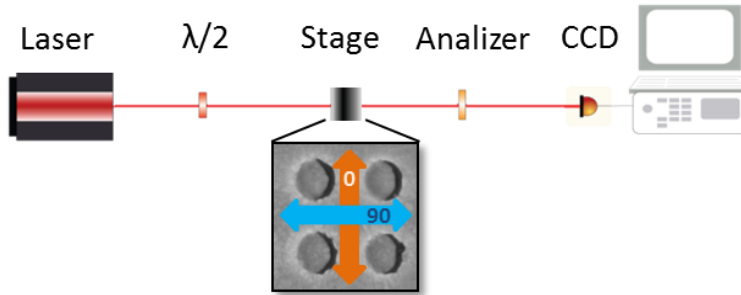

Figure 3.14 Measurement setup comprising a laser source followed by a polarizer, a rotatory stage holder and a polarization analyzer. The incident linear polarization is maintained throughout the experiment and the measurements are taken with the sample aligned at 0 or 90º. The signal was collected through a 4X objective with NA 0.1 and averaged over a 3x3 mm² area.

Upon excitation with a 633 nm linearly polarized laser light, the averaged PL spectra for each linear polarization are shown in Figure 3.15 where the spectra of asymmetric nanostructures (solid lines) are compared with the signal acquired from a flat reference (dashed lines).
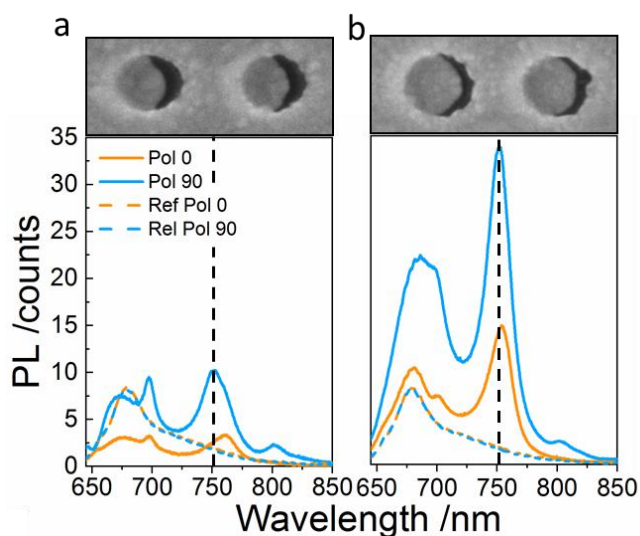
Figure 3.15 Integrated PL intensity for asymmetric samples with 80 nm gap (e) and 30 nm gap (f). Dashed lines correspond to the PL measured for the flat reference. Inset SEM images of the corresponding geometry inspected.

In addition to the main emission peak of the dye at 685 nm, an intense emission peak at 750 nm appears for both samples with nanogaps, being more intense in the case of the 30 nm gap array (Figure 3.15b). The different PL intensity of the emitted light for both polarizations together with the important shaping of the spectral profile suggest a polarization selective interaction between the localized electric field in the plasmonic crystal structure and the emitted light.

The signal was found homogeneous throughout the inspected areas with a higher signal for the samples with the 30 nm gap. Figure 3.16 show PL map of the 3x3 mm² inspected area at λ = 750 nm ± 20 nm highlighting the high homogeneity over large area. In the first instance the increase of intensity from flat to nanogaps structures can be ascribed to the complex nanostructuration and is can be easily explained by the fact that corrugated surfaces supports localized plasmon resonances that enhance the fluoresce signal.[43] Further studies unveil the origin of this enhancement highlighting the importance of the nanogaps array. To do so a careful comparison of the optical properties with the PL enhancement will be carried out.
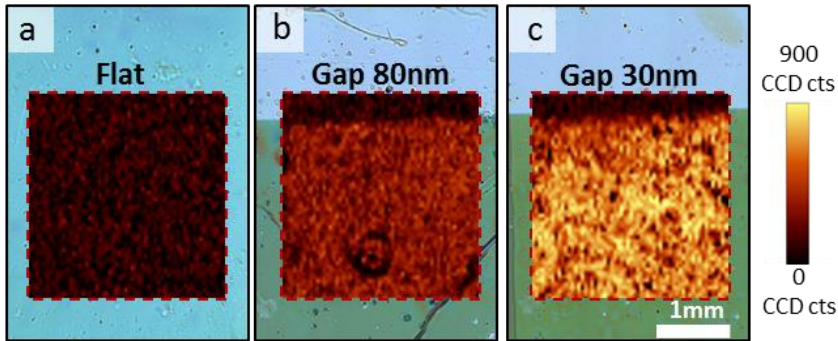
Figure 3.16. PL images of the inspected area for the three different samples. a) flat silver reference b) holes array with nanogaps of 80nm and lattice 500nm, c) holes array with nanogaps of 30nm and lattice 500nm

- *Photoluminescence enhancement: Experimental results*

The emission enhancement can be due to both increased absorptions, often related to FRET mechanisms, and increased emission, where the electromagnetic environment shapes the density of states inducing a higher probability of emission.

In order to highlight the shaping of the emission induced by polarization sensitive plasmonic resonances, we calculate the PL enhancement defined as the ratio between the signal measured from the plasmonic structure and that from a flat silver reference. Figure 3.17, shows the reflectance of the nanostructures (30nm gaps array) covered with a 250nm thick layer of PVA versus the respective PL enhancement of the same sample. More than a 20-fold enhancement in photoluminescence, homogeneous over the entire scanned area of the sample, was found for the polarization orthogonal to the gap (Figure 3.17b).
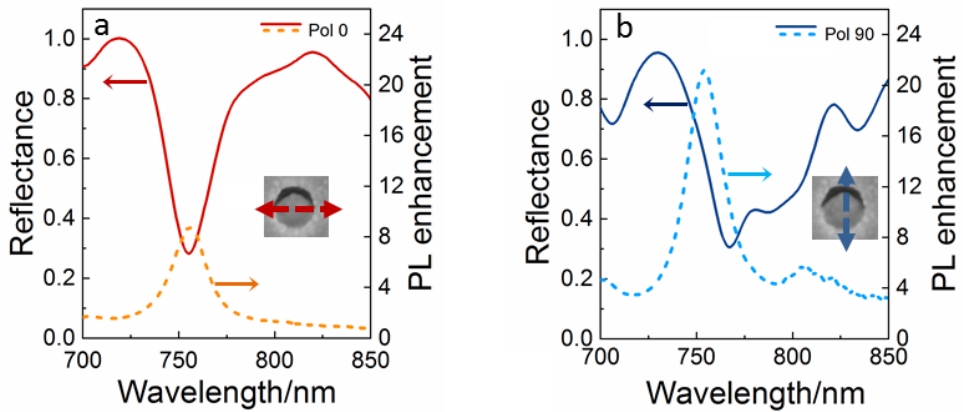
Figure 3.17 Reflectance and photoluminescence enhancement observed in a plasmonic crystal with 30 nm gaps. Reflection (solid) and PL enhancement (dashed) profile for polarization (a) 0° and (b) 90º. The inset shows the orientation of electric field.

In Figure 3.17 the zero order of diffraction for square arrays can be qualitatively identified knowing the media refractive index and the lattice constants. For a square array it can be calculated by the formula $\lambda_{max} \sim n \cdot L$ with n the refractive index of the environment and L the lattice parameter. In this case, the refractive index of PVA in the considered range of wavelength is 1.48.[44] Thus using a square array with lattice parameter of 500 nm the results show good agreement with the experimental data showing an intense dip at 750 nm. This explains the appearance of reflectance minimum at 750 nm for both polarizations since the square array equivalent for both perpendicular and parallel orientation. Interestingly this dip correlates to a peak in the PL enhancement (dashed lines). This suggest that the intense PL enhancement is due to the coupling of plasmonic resonances with the emitted light, but do not clarifies the different magnitudes of emission at 750 nm with the two opposite polarizations.

- *Photoluminescence enhancement: FDTD simulation*

In order to gain insight in the physics behind the selective enhancement, we reproduced the experimental reflectance spectra of the 30 nm nanogaps samples for both polarizations using the finite difference time domain (FDTD)

method (Simulation performed by Dr Garcia Pomar). As expected, the lattice plasmon resonance enhances the electric field around 750 nm (Figure 3.18).
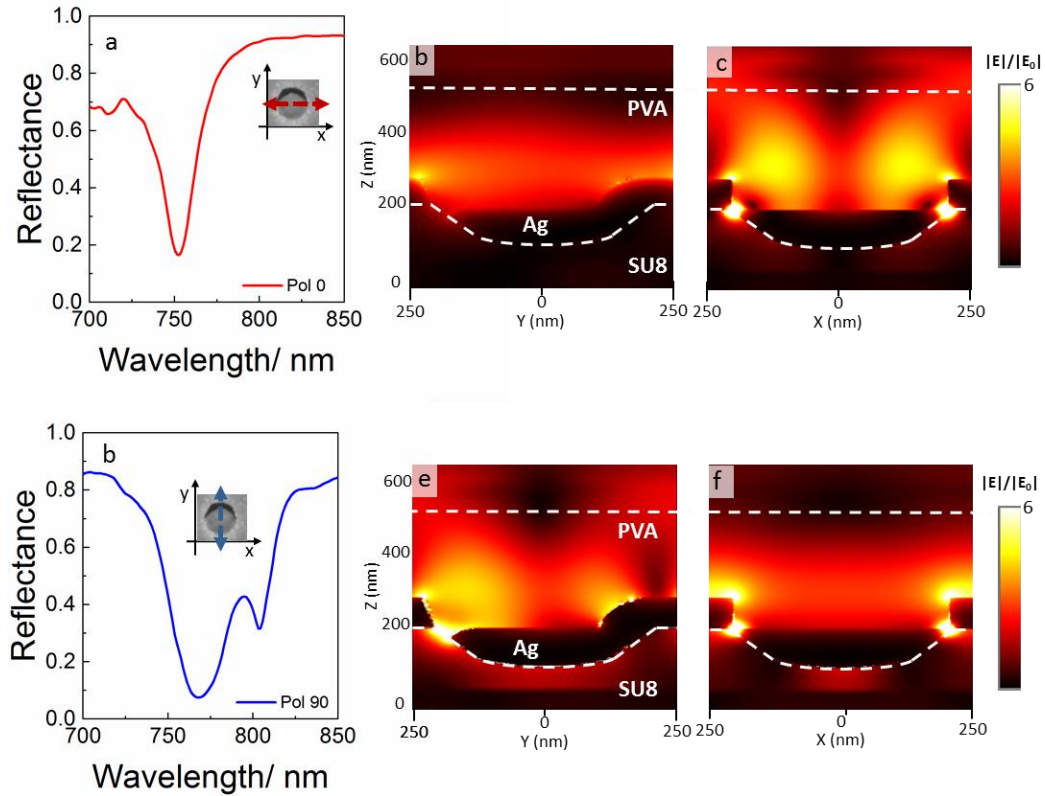
Figure 3.18. FDTD simulated reflectance for polarizations (a) 0° and (b) 90º. Electric field distribution of light at 750 nm for polarization parallel (b-c) and perpendicular to the nanogaps (e-h).

Interestingly the electric filed intensity in the nano gap for polarization 0 is much higher than the one for opposite direction suggesting that the nanogaps could be actively involved in the enhancement process. In fact, the lattice plasmon surface waves generated by the array are scattered by the nanogaps creating a high enhancement of the electric field responsible for the greater PLE. Due to the asymmetry, the propagating plasmons interact with different geometrical sides of the gap, creating a different PLE for each linear polarization.

This effect is further corroborated by the calculation of the Purcell factor (PF) of a dipole, with a wavelength of 750 nm, located in the middle of the nanogap with parallel and perpendicular polarization. The Purcell factor describes the emission rate enhancement of an emitter inside a cavity or resonator, which is correlated to the PL enhancement shown in Figure 3.18b. In agreement with the experiments, a higher Purcell factor is calculated for polarization perpendicular to the nanogap, obtaining a value of *Pf=34* versus a value of *Pf=3* for a polarization parallel to the nanogaps.

Finally to support the hypothesis that the main resonance at 750nm is a Plasmon surface waves we performed numerical simulations varying the angle of incidence expecting the angular evolution of surface lattice modes.[35] Figure 3.19 depicts the optical response upon a variation of the angle of incidence of the impinging light for both TE (electric field perpendicular to the incidence plane) and TM (magnetic field perpendicular to the incidence plane) polarizations, with the direction of the electric field parallel (pol 0) and perpendicular (pol 90) to the nanogap. The intese resonance present around 750 nm which overlaps with the PLE (Figure 3.21a,b) is insensitive to the angle of incidence for polarization parallel and perpendicular in the TE mode (Figure 3.19b-d). On the other hand, for the TM mode the resonance shows angle dependency for parallel polarization at angles higher that 10 degrees and for perpendicular polarization for angles higher than 15 degrees. This behavior is believed to be due to the interaction with the nanogap resonance that is strictly localized at the gap. The propagating surface plasmon polariton nature of the resonances is corroborated by the angle dispersion of the mode at 750nm that exists only for TM polarization.
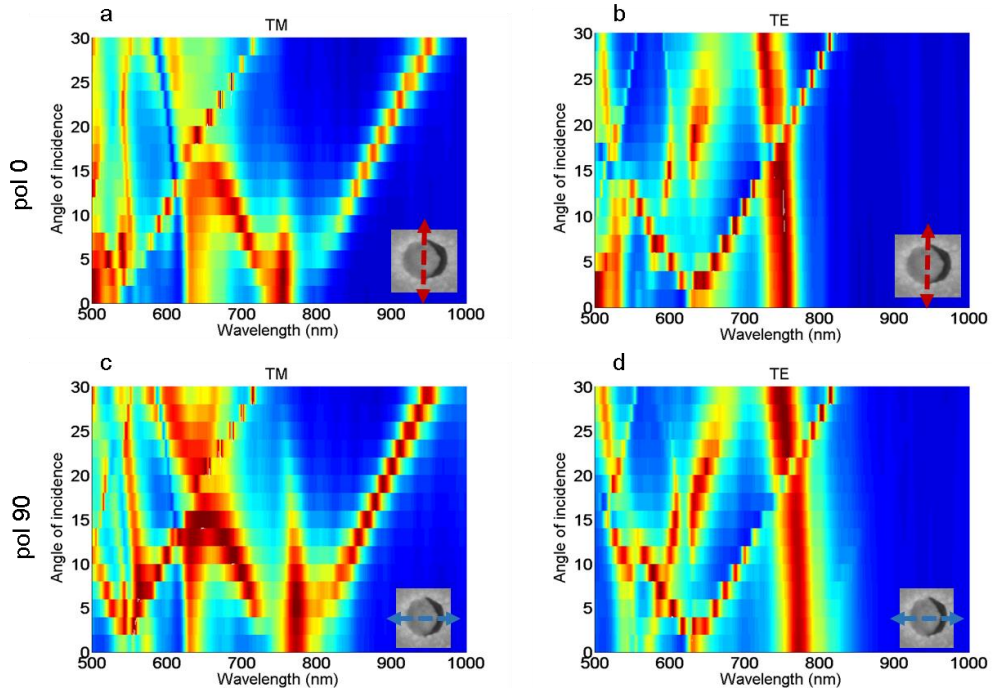
Figure 3.19. Absorption spectra (FDTD) for both polarizations TE and TM for a 30 nm nanogaps array for polarization of the electric field parallel to the nanogap (a, b) and for polarization perpendicular to the nanogap (c, d) with varying angle of incidence. The insets show the direction of the electric field.

3.5 CONCLUSIONS

Along this chapter the plasmonic response of asymmetric metal nanostructures supporting hybrid plasmonic photonic resonances has been analyzed. FT-VIS microspectroscopy, and Fluorescence spectroscopy were used to characterize the samples showing good agreement with simulation and validating the original idea to fabricate nanostructures with polarization selective light matter interaction.

The merger of top down (NIL) and bottom up (OAD) approaches allowed high throughput fabrication of new asymmetric nanostructures demonstrating how highly homogeneous large scale plasmonic devices can be easily engineered for application in enhanced spectroscopy. The possibility to control fabrication parameters such as tilt angle, multiple evaporation setups, lattice parameter of

the array and finally feature depth and shape have been exploited. The relatively ease of the tuning have led to the successful fabrication of metallic array of wedges, spoon-like nanostructures, nanogaps or half metallic pillars each of them producing homogeneous and selective optical response upon the inspection with polarized light.

The optical characterization unveiled the effect of the lattice parameter and tilt angle on the optical response and allowed optimizing and restricting the study to sample with lattice 500nm and 45° tilt, as they showed more intense optical response in the visible and NIR range. Nanogaps array can be fabricated tuning the depth of the holes. Double-wedges arrays have been demonstrated to act as polarization sensitive mirrors that also showed completely different and intense structural color under perpendicular and parallel linear polarization. Further multiple deposition led to chiral metallic nanostructures which show an intense chiroptical activity corroborated by CD spectroscopy. Finally, half metallic pillars arrays have been fabricated.

Photoluminescence enhancement have also been demonstrated with nanogaps arrays. The ordered lattice along with the presence of nanogaps has been found responsible for the 20-fold selective enhancement of emission of ATTO655.

In summary we developed plasmonic devices to control light and its polarization at the nanoscale. This work paves the way toward development of hybrid bottom up/top down approaches to achieve low cost and high throughput fabrication for lab scale optimization and research as well as to meet the need of industrial commercialization of large scale and reliable optoelectronic devices.

3.6 REFERENCES

(1)   Willets, K. A.; Van Duyne, R. P. Localized Surface Plasmon Resonance Spectroscopy and Sensing. *Annu. Rev. Phys. Chem* **2007**, *58*, 267–297.

(2)   Poddubny, A.; Iorsh, I.; Belov, P.; Kivshar, Y. Hyperbolic Metamaterials. *Nature Photonics*. December 2013, pp 958–967.

(3)   Gómez-Castaño, M.; Zheng, H.; García-Pomar, J. L.; Vallée, R.; Mihi, A.; Ravaine, S. Tunable Index Metamaterials Made by Bottom-up Approaches. *Nanoscale Adv.* **2019**, *1*, 1070–1076.

(4)   Lenzi, E.; Jimenez de Aberasturi, D.; Liz-Marzán, L. M. Surface-Enhanced Raman Scattering Tags for Three-Dimensional Bioimaging and Biomarker Detection. *ACS Sensors* **2019**, *4*, 1126–1137.

(5)   Atwater, H. A.; Polman, A. Plasmonics for Improved Photovoltaic Devices. *Nat. Mater.* **2010**, *9*, 205–213.

(6)   Baek, S.; Molet, P.; Choi, M.; Biondi, M.; Ouellette, O.; Fan, J.; Hoogland, S.; García de Arquer, F. P.; Mihi, A.; Sargent, E. H. Nanostructured Back Reflectors for Efficient Colloidal Quantum-Dot Infrared Optoelectronics. *Adv. Mater.* **2019**, 1901745.

(7)   Garcia-Pomar, J. L.; Nieto-Vesperinas, M. Imaging of Extended Objects by a Negative Refractive Index Slab. *New J. Phys.* **2005**, *7*, 160.

(8)   Lozano, G.; Louwers, D. J.; Rodríguez, S. R. K.; Murai, S.; Jansen, O. T. A.; Verschuuren, M. A.; Gómez Rivas, J. Plasmonics for Solid-State Lighting: Enhanced Excitation and Directional Emission of Highly Efficient Light Sources. *Light Sci. Appl.* **2013**, *2*, 66.

(9)   Fedotov, V. A.; Rose, M.; Prosvirnin, S. L.; Papasimakis, N.; Zheludev, N. I. Sharp Trapped-Mode Resonances in Planar Metamaterials with a Broken Structural Symmetry. *Phys. Rev. Lett.* **2007**, *99*.

(10)   Singh, R.; Cao, W.; Al-Naib, I.; Cong, L.; Withayachumnankul, W.; Zhang, W. Ultrasensitive Terahertz Sensing with High- Q Fano Resonances in Metasurfaces. *Appl. Phys. Lett.* **2014**, *105*, 171101.

(11)   Zheludev, N. I.; Prosvirnin, S. L.; Papasimakis, N.; Fedotov, V. A. Lasing Spaser. *Nat. Photonics* **2008**, *2*, 351–354.

(12)   Weis, P.; Garcia-Pomar, J. L.; Rahm, M. Towards Loss Compensated and Lasing Terahertz Metamaterials Based on Optically Pumped Graphene. *Opt. Express* **2014**, *22*, 8473.

(13)   Liu, N.; Kaiser, S.; Giessen, H. Magnetoinductive and Electroinductive Coupling in Plasmonic Metamaterial Molecules. *Adv. Mater.* **2008**, *20*, 4521–4525.

(14)   Papasimakis, N.; Zheludev, N. I. Metamaterial-Induced Transparency: Sharp Fano Resonances and Slow Light. *Opt. Photonics News* **2009**, *20*, 22.

(15)   Cao, T.; Mao, L.; Qiu, Y.; Lu, L.; Banas, A.; Banas, K.; Simpson, R. E.; Chui, H. C. Fano Resonance in Asymmetric Plasmonic Nanostructure: Separation of Sub-10 Nm Enantiomers. *Adv. Opt. Mater.* **2019**, *7*, 1801172.

(16)   Liu, T.; Besteiro, L. V.; Liedl, T.; Correa-Duarte, M. A.; Wang, Z.; Govorov, A. O. Chiral Plasmonic Nanocrystals for Generation of Hot Electrons: Toward Polarization-Sensitive Photochemistry. *Nano Lett.* **2019**, *19*, 1395–1407.

(17)   Knudson, M. P.; Li, R.; Wang, D.; Wang, W.; Schaller, R. D.; Odom, T. W. Polarization-Dependent Lasing Behavior from Low-Symmetry Nanocavity Arrays Article. *ACS Nano* **2019**, *13*, 7441.

(18)   Ramezani, M.; Halpin, A.; Fernández-Domínguez, A. I.; Feist, J.; Rodriguez, S. R.-K.; Garcia-Vidal, F. J.; Gómez Rivas, J. Plasmon-Exciton-Polariton Lasing. *Optica* **2017**, *4*, 31.

(19)   Matioli, E.; Brinkley, S.; Kelchner, K. M.; Hu, Y.-L.; Nakamura, S.; DenBaars, S.; Speck, J.; Weisbuch, C. High-Brightness Polarized Light-Emitting Diodes. *Light Sci. Appl.* **2012**, *1*, e22–e22.

(20)   Zhang, X.; Whitney, A. V.; Zhao, J.; Hicks, E. M.; Van Duyne, R. P. Advances in Contemporary Nanosphere Lithographic Techniques. *J. Nanosci. Nanotechnol.* **2006**, *6*, 1920–1934.

(21)   Maldovan, M.; Thomas, E. L. *Periodic Materials and Interference Lithography: For Photonics, Phononics and Mechanics*; Wiley-VCH Verlag GmbH & Co. KGaA, 2009.

(22)   Malyarchuk, V.; Hua, F.; Mack, N. H.; Velasquez, V. T.; White, J. O.; Nuzzo, R. G.; Rogers, J. A. High Performance Plasmonic Crystal Sensor Formed by Soft Nanoimprint Lithography. *Opt. Express* **2005**, *13*, 5669.

(23)   Kosiorek, A.; Kandulski, W.; Chudzinski, P.; Kempa, K.; Giersig, M. Shadow Nanosphere Lithography: Simulation and Experiment. *Nano Lett.* **2004**, *4*, 1359–1363.

(24)   Tang, Z.; Wei, A. Fabrication of Anisotropic Metal Nanostructures Using Innovations in Template-Assisted Lithography. *ACS Nano*. February 28, 2012, pp 998–1003.

(25)   Gwinner, M. C.; Koroknay, E.; Fu, L.; Patoka, P.; Kandulski, W.; Giersig, M.; Giessen, H. Periodic Large-Area Metallic Split-Ring Resonator Metamaterial Fabrication Based on Shadow Nanosphere Lithography. *Small* **2009**, *5*, 400–406.

(26)   Bochenkov, V. E.; Sutherland, D. S. Chiral Plasmonic Nanocrescents: Large-Area Fabrication and Optical Properties. *Opt. Express* **2018**, *26*, 27101.

(27)   Hou, Y.; Li, S.; Su, Y.; Huang, X.; Liu, Y.; Huang, L.; Yu, Y.; Gao, F.; Zhang, Z.; Du, J. Design and Fabrication of Three-Dimensional Chiral Nanostructures Based on Stepwise Glancing Angle Deposition Technology. *Langmuir* **2013**, *29*, 867–872.

(28)   Ai, B.; Zhao, Y. Glancing Angle Deposition Meets Colloidal Lithography: A New Evolution in the Design of Nanostructures. *Nanophotonics*. De Gruyter 2018, pp 1–26.

(29)   Larsen, G. K.; He, Y.; Ingram, W.; Lapaquette, E. T.; Wang, J.; Zhao, Y. The Fabrication of Three-Dimensional Plasmonic Chiral Structures by Dynamic Shadowing Growth. *Nanoscale* **2014**, *6*, 9467–9476.

(30)   Beesley, D. J.; Semple, J.; Krishnan Jagadamma, L.; Amassian, A.; McLachlan, M. A.; Anthopoulos, T. D.; Demello, J. C. D. J. Beesley, J. Semple, L. Krishnan Jagadamma, A. Amassian, M. A. McLachlan, T. D. Anthopoulos, J. C. Demello, Nat. Commun. 2014. *Nat. Commun.* **2014**, *5*, 3933.

(31)   Zhang, C.; Subbaraman, H.; Li, Q.; Pan, Z.; Ok, J. G.; Ling, T.; Chung, C. J.; Zhang, X.; Lin, X.; Chen, R. T.; Guo, L. J. Printed Photonic Elements: Nanoimprinting and Beyond. *Journal of Materials Chemistry C*. Royal Society of Chemistry 2016, pp 5133–5153.

(32)   Liu, L.; Wu, F.; Xiao, D.; Teng, F.; Xu, D.; Feng, L.; Lu, N. Fabrication of Plasmonic Opposite Metal Spindles in Nanowells by Shadow Deposition for Sensing. *RSC Adv.* **2017**, *7*, 4759–4762.

(33)   Zhang, M.; Pacheco-Peña, V.; Yu, Y.; Chen, W.; Greybush, N. J.; Stein, A.; Engheta, N.; Murray, C. B.; Kagan, C. R. Nanoimprinted Chiral Plasmonic Substrates with Three-Dimensional Nanostructures. *Nano Lett.* **2018**, *18*, 7389–7394.

(34)   Liu, C.; Wang, J.; Yang, W.; Gao, Y.; Yang, Z. Influence of Surface Roughness on Surface Plasmon Resonance Phenomenon of Gold Film. *Chinese Opt. Lett. Vol. 14, Issue 4, pp. 042401-* **2016**, *14*, 042401.

(35)   Kravets, V. G.; Kabashin, A. V; Barnes, W. L.; Grigorenko, A. N. Plasmonic Surface Lattice Resonances: A Review of Properties and Applications. **2018**.

(36)   Murai, S.; Oka, S.; Azzam, S. I.; Kildishev, A. V.; Ishii, S.; Tanaka, K. Enhanced Absorption and Photoluminescence from Dye-Containing Thin Polymer Film on Plasmonic Array. *Opt. Express* **2019**, *27*, 5083.

(37)   Zeng, C.; Hu, X.; Shi, M.; Qiu, X.; Li, Y.; Xia, J. Enhancing Light Emission from

Germanium Quantum Dots by Bowtie Antennas. *J. Light. Technol.* **2016**, *34*, 3283–3287.

(38)   Baumberg, J. J.; Aizpurua, J.; Mikkelsen, M. H.; Smith, D. R. Extreme Nanophotonics from Ultrathin Metallic Gaps. *Nat. Mater.* **2019**, *18*, 668–678.

(39)   Ding, B.; Hrelescu, C.; Arnold, N.; Isic, G.; Klar, T. A. Spectral and Directional Reshaping of Fluorescence in Large Area Self-Assembled Plasmonic−Photonic Crystals. *Nano Lett* **2013**, *13*, 386.

(40)   Vecchi, G.; Giannini, V.; Gómez Rivas, J. Shaping the Fluorescent Emission by Lattice Resonances in Plasmonic Crystals of Nanoantennas. *Phys. Rev. Lett.* **2009**, *102*, 146807.

(41)   Ramezani, M.; Berghuis, M.; Rivas, J. G. Strong Light-Matter Coupling and Exciton-Polariton Condensation in Lattices of Plasmonic Nanoparticles [Invited]. **2019**.

(42)   Green, A. P.; Buckley, A. R. Solid State Concentration Quenching of Organic Fluorophores in PMMA †. *Phys. Chem. Chem. Phys* **2015**, *17*, 1435.

(43)   Mertens, H.; Biteen, J. S.; Atwater, H. A.; Polman, A. Polarization-Selective Plasmon-Enhanced Silicon Quantum-Dot Luminescence.

(44) .   Bodurov, I. Vlaeva, A. Viraneva, T. Yovcheva, S. S. Modified Design of a Laser Refractometer. *Nanosci. Nanotechnol.* **2016**, *16*, 31–33.

SECTION III

GOLD NANOPARTICLES SUPERCRYSTALS

TEMPLATE SELF-ASSEMBLY OF GOLD NANOPARTICLES SUPERCRYSTALS

I n the last decade, nanoscience research was moving towards a more challenging target, such as the fabrication of macroscale devices and materials with nanoscale precision. Thus, achieving a complete understanding and control over inter-particle interactions represents one of the big challenges in the future of nanotechnology. In this regard, molecular science will provide innovative tools to expand the limitation of nanoscience i.e. though self-organization of pre-programmed nanoparticles.[1] Computational methods will also expand their boundaries, providing tools to study both the self-assembly itself and the properties of the final system. The connection of nanoscale and macroscale science will enable future developments

This chapter will explore the potential of nanoparticles self-assembly under confinement. In one hand we have gold nanoparticles, excellent nanoobjects for plasmonic application; on the other hand we bring these nano objects together in a controlled way. This technique allows to precisely placing nanoparticles in ordered arrays which finally leads to easy tuning of their optical response.

This work was carried out in collaboration with the Bionanoplasmonic group at the CIC BiomaGUNE in San Sebastian.

~ ● ~

4.1 INTRODUCTION

Nobel metals nanoparticles (NP) dominate the field of nanotechnology because of the possibility to tailor their properties for several different applications.[2,3] They both offer the unique possibility to enhance light matter interaction and can be used as building blocks for the fabrication of new plasmonic devices.

Metal NPs possess several novel properties compared to bulk materials, such as high extinction coefficients (~10^6 times larger than common dye molecules). These properties allow them to be used in a multitude of applications such as energy harvesting[4], medicine[5], catalysis[6], metamaterials[7], and sensing[8]. Chemical methods developed over the past two decades enable the synthesis of different metal nanocrystals. In this pool of materials, gold nanoparticles stand out because of their excellent optical properties and good chemical stability as well as the possibility to produce nanocrystals with uniform size and shape. Recent works also show increasing interest on non-spherical particles such as triangles,[9] stars,[10] and even chiral nanoparticles[11], (Figure 4.1). This shape engineering allows expanding the optical properties achieving polarization sensitive resonances, chiral plasmonic response, and complex interference effects, making them excellent candidates for applications in electronics, sensing, imaging, and photothermal therapy.[5,12–15]
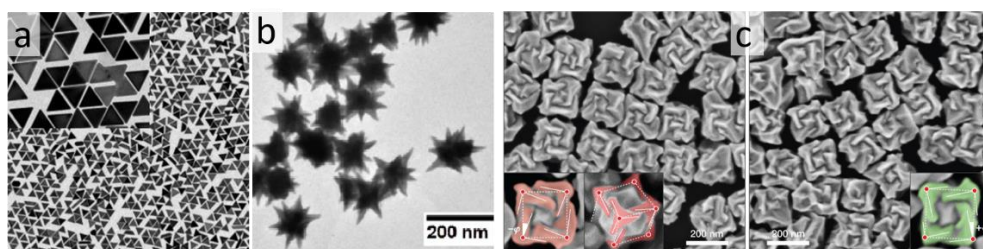

Figure 4.1. SEM images of different shapes of nanoparticles. a) nanotriangles, b) nanostars, c) chiral nanocubes. Reprinted form ref. 9, 10 12

The possibility to use NP as building blocks inspired the fabrication of new engineered materials (Figure 2.4). As we treated in section I, when two metallic particles are sufficiently close to each other, the near-field coupling between

them can give rise to hybridized modes along with an extreme electromagnetic (EM) field enhancement concentrated in the so called "hot spots".[16] These resonances are usually red-shifted and broadened compared to the localized surface plasmon resonances (LSPRs) of isolated particles. The frequencies at which such collective resonances appear, depend on nanoparticles material, gap size, as well as on the cluster dimension and symmetry.[17,18] More complex structures extend the concept of near-field coupling by adding periodicity in the order of visible wavelength which gives rise to additional diffractive resonances due to optical far-field interactions. These so-called lattice plasmon modes can be tuned over a wide range of frequency by varying lattice parameters and have been reported to yield remarkably sharp resonances.[19]

For these reasons, many efforts were spent to achieve the fabrication of controlled nanoparticle ensembles with different shape and size. Electron beam lithography as well as others top-down techniques have been used for years to fabricate nanoparticle ensembles with high precision and reliability. Even though these methods were limited to the fabrication of proof of concept devices they allowed understanding the physical behavior of these emerging systems, shading light into the origin of near field plasmonic coupling.[20] However, the need to implement these systems into real devices pushes toward the development of cheap and scalable techniques such as self-assembly. The assembly route implies fitting different components together following predefined rules, obtaining the target objects. This process is reversible and it undergoes through a series of trial and error steps.[1] Methods as simple as drop casting or precipitation of colloidal dispersions yield centimeter scale assemblies which however usually comes at the cost of poor homogeneity.[21] In order to solve the abovementioned issues, template assisted self-assembly strategies have been improved significantly over the past decade for preparing homogeneously structured nanoparticle films.[18,22] Furthermore, the possibility to arrange nanoparticles into highly ordered superstructures represent a real breakthrough in nanotechnology since it allows tuning the frequency of hybrid plasmonic-photonic resonances and facilitates nanophotonic device engineering.[23] Still, the challenge resides in fabricating hierarchical assemblies

that operate at visible wavelengths and display sufficiently good homogeneity over macroscopic areas.[24,25]

In this chapter, I will present a scalable, template-assisted assembly technique capable of arranging gold nanoparticles into regular, periodic arrays of well-defined plasmonic clusters. The obtained two-dimensional (2D) superlattices exhibit both strong near-field coupling and an optical response that can be tuned from the visible through the near-infrared (NIR). The morphological and optical properties will be analyzed to tune the assembly parameters achieving homogeneous plasmonic crystals over large scale. Finally, a comprehensive study of the optical properties unveils the key parameters responsible for the resonances hybridization and paves the way for further implementation in real devices.

4.2   TEMPLATE ASSISTED SELF-ASSEMBLY

Template self-assembly (TSA) is a versatile fabrication process that can arrange various micrometer to nanometer sized particles into templates with defined patterns. It is a promising technique for functional materials fabrication especially in plasmonics where we can play with the multiple coupling effects between nanoparticle and molecules. The process depicted in Figure 4.2contains the following four main steps: i) <u>Deposition</u> of colloidal solution on the surface of a PDMS mold, ii) <u>Spreading</u> of the colloid solution by placing an hydrophilized glass coverslip on top of the PDMS surface iii) <u>Evaporation</u> of the dispersion medium, iv) <u>Lift-off</u> of the glass substrate.
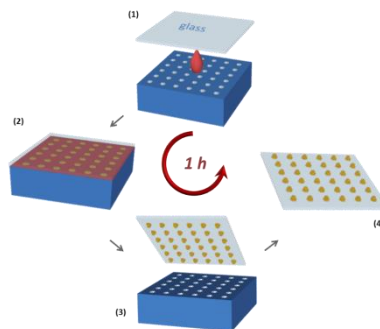
Figure 4.2. Schematic representation of the template-assisted assembly of gold nanospheres into hierarchical superlattices: (1) Deposition of an aqueous AuNSs dispersion on the surface of a patterned PDMS stamp. (2) A glass coverslip is placed on top of the PDMS, spreading the colloidal dispersion over the patterned surface. (3) Removal of the glass substrate carrying the assembled superlattice.

This technique offers a practical route to fabricate complex assemblies of monodispersed colloids with well-defined sizes, shapes, and Structures (Figure 4.3a).[26] These assemblies can be easily engineers to achieve tunable optical properties as in the case of as nanoparticles stripes (Figure 4.3b).[27]
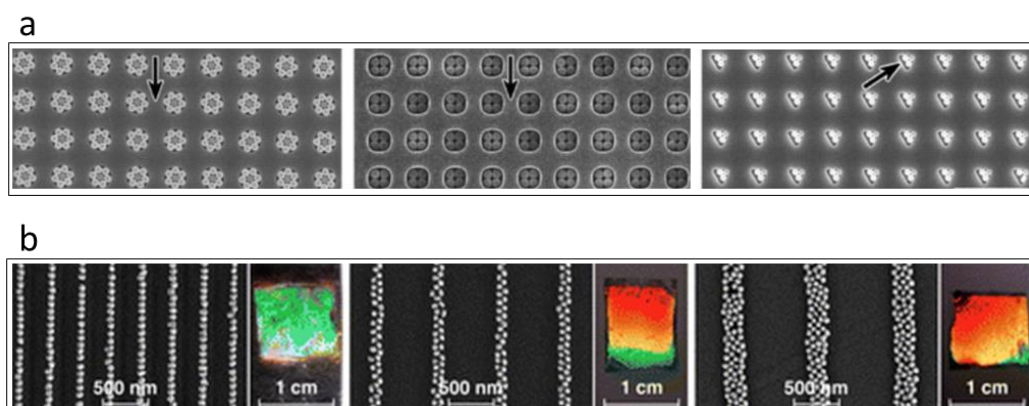

Figure 4.3 a) Colloidal aggregates assembled under the confinement of templates. The arrow indicates the flow direction for the liquid slug. b) single particle chains, dimer chains, or tetramer chains were obtained with homogeneous surface coverage over centimeter-squared-scale areas. Reprinted from ref 26 and 27.

One of the most recent example of TSA is the successful assembly of gold nanospheres into pyramids superlattices.[28] Figure 4.4 show highly ordered pyramidal supercrystals from macro scale to sub micrometer level. In this work a confined drop of gold nanoparticles dispersion yield regular macroscale arrays of separated pyramids.
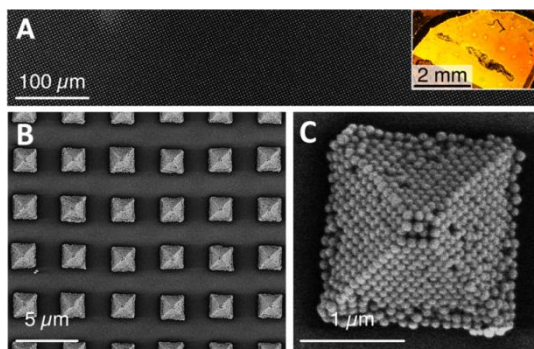
Figure 4.4 Multiscale SEM characterization of 3D supercrystals produced by templated assembly of monodisperse PEG-AuNSs. Macroscopically, the sample exhibits iridescence under sideways illumination (inset top left side). (a) Macroscale homogeneity over millimeter and micrometer scale. (b) Higher magnification images show excellent regularity of the pyramidal structures as well as a high degree of order in their densely packed lateral faces (c). Reprinted from ref. 28.

4.3   PARAMETERS FOR HOMOGENOUS ASSEMBLIES

Template self-assembly is a promising technique however in order to achieve homogeneous results we need to strictly fulfill some key features.

- Highly monodispersed nanoparticles. The second essential prerequisite is to have high quality building blocks that lead to highly order superstructures. Thus, advanced procedures that yield highly concentrated uniform AuNPs are of extreme importance for the development of novel materials based on nanoparticles template self-assembly.

- High quality molds. The exact positioning onto ordered arrays is imposed by soft templates expanding the versatility of the classical self-assembly process. A sweep of lattice constant gives us the possibility to change the coupling condition between localized and propagating surface plasmon modes tuning the final optical response. These new soft templates need to meet certain mechanical and morphological properties that do not affect the

colloidal solution assembly when drying and the final structures when pealing-off.

- <u>Surface chemistry control</u>. The successful and homogeneous self-assembly of nanoparticles into supercrystals over large relies on the interplay of environmental and surface properties of both nanocrystals and substrate. Different approaches are adopted depending on the nanoparticle type. For instance, in gold nanorods and nanospheres, the different morphology changes the inter-particle forces which drive the assembly. For this reason, upon a change of the building block, it is necessary and sometimes compulsory to consider a change in the stabilizing agents and environment.

The quality of these assemblies is often compromised because of the coffee-ring effect. As the name suggests, it refers to the ring stain that is usually observed when a drop of coffee spills and dries on a surface. In general, every colloidal solution that evaporates on a surface leaves such inhomogeneous material distribution. This effect is ascribed to a form of capillary flow in which the liquid evaporating from the edge drain outward liquid from the interior. The dispersed colloids are then driven toward the rim of the confined droplet during drying due to convective forces.[29] In some applications these ring deposits are used to design a pattern onto a surface,[30–32] however, in our case it decreases the quality of the assembly since it drags the nanoparticles outside the patterned area, hindering the template assembly. As a rule of thumb, we can control the shape and thickness of the deposit by controlling the speed and spatial variation of the colloidal solution evaporation.

4.3.1 Nanoparticles synthesis

- *Gold nanospheres*

Monodisperse spherical gold nanoparticles with an average diameter of 52 nm (standard deviation: 2 nm) were synthesized and characterized by the

Bionanoplasmonic group as previously published.[33] In brief, a protocol that combines seeded growth with controlled particle etching was used. Initial seeds were prepared by adding 50 µL of a 0.05 M $HAuCl_4$ solution to 5 mL of a 100 mM CTAC solution and injecting 200 µL of a fresh $NaBH_4$ (20 mM) solution while stirring vigorously. The resulting colloidal suspension was diluted by a factor of 10 with 100 mM CTAC solution. These initial seeds were grown to 10 nm diameter by mixing 900 µL of the diluted gold colloid with 10 mL of 25 mM CTAC solution and 40 µL of 100 mM ascorbic acid, followed by injection of 50 µL of a 50 mM $HAuCl_4$ solution under rapid stirring. Growth to the final size was achieved by diluting 250 µL of the obtained suspension with 100 mL of a 25 mM CTAC solution, adding 400 µL of 100 mM ascorbic acid, and injecting 500 µL of a 50 mM $HAuCl_4$ solution under rapid stirring. After 1 h, 100 µL of a dilute sodium hypochlorite solution (1-1.5 wt.% of available chlorine) was added stirring vigorously. After 5 min, 25 µL of a 50 mM $HAuCl_4$ solution were added and the reaction was left at 30 ºC until a constant absorption at 400 nm (Abs_{400}) was reached. The particles were then cleaned immediately by centrifuge washing twice at 3500 rpm with 2 mM CTAC solution.

- *Gold Nanorods*

Single-crystal gold nanorods with an average length of 55 ± 5 nm and a diameter of 16.5 ± 1.5 nm (aspect ratio: 3.4 ± 0.4) were synthesized via a seeded growth method with minor modifications, according to the following procedure.[34] The seeds were prepared by the $CTAB/NaBH_4$ procedure: 25 µL of a 0.05 M $HAuCl_4$ solution was added to 4.7 mL of a 0.1 M CTAB solution; 300 µL of a freshly prepared 0.01 M $NaBH_4$ solution was then injected under vigorous stirring. Excess borohydride was consumed by ageing the seed solution for 30 min at room temperature prior to use. In a typical synthesis, 45 mg of 5- bromosalicylic acid was added to 50 mL of 0.05 M CTAB and the mixture was mildly stirred for 15 min until complete dissolution. Then, 480 µL of 0.01 M $AgNO_3$, 500 µL of a 0.05 M $HAuCl4$ and 200 µL of 0.1 M ascorbic acid solution were added. After 2 h at 25 °C (or once BrSal has completely reduced Au (III) to Au (I), as monitored by the reduction in the absorbance of the Au(III) CTAB complex at 390 nm), 50 µL of 0.1 M ascorbic acid solution and 80 µL of

the seed solution were added under vigorous stirring. After 2h, the resulting gold nanorods displayed LSPR maxima in the spectral range of 820 to 890 nm. Tailoring the LSPR to 770 nm was achieved by overgrowth of the synthesized gold nanorods. The amount of ascorbic acid necessary for this was determined by overgrowing small aliquots of the prepared nanorods with increasing volumes of the ascorbic acid solution (0.4 to 0.8 µL per mL). The mixture was left undisturbed at room temperature for at least 4 h before the particles were centrifuge washed for 40 min (7000 rpm, 30 °C) using 50 mM CTAB for redispersion.

4.3.2 Molds fabrication

The holes arrays with different lattice parameters were fabricated in silicon by electron beam lithography and replicated with OrmoStamp® (Microresist Technology) to obtain the negative image. The latter material is a photocurable resin with high young modulus (650MPa) suitable to replicate high pillars array avoiding collapse. This step allows the replication of the original master without losing quality. Soft molds were fabricated by pouring a 10:1 mixture of prepolymer and curing agent onto Ormostamp pillars array (Figure 4.5).[35,36] The mixtures were degassed for 2 hours and then cured for 45 min at 100 ºC.

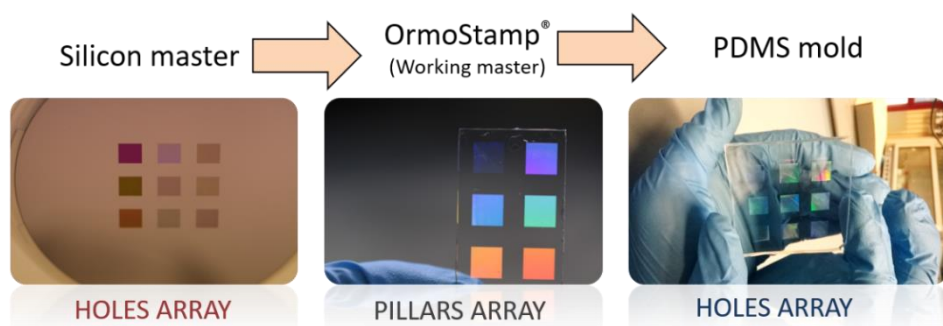*Figure 4.5 Soft mods fabrication workflow. Replication process of the original master that involves an intermediate step to fabricate a rigid working master (OrmoStamp). The final outcome will show high quality holes arrays in soft PDMS.*

When this formulation is used to replicate feature smaller than 700nm its high viscosity hinders the percolation of pre-polymer onto the pillars leading to a

non-conformal covering. Therefore, even though the original master shows holes depth of 350nm, the replicated molds will present shallower holes. However, since the lift-off process becomes more and more critical as the template depth increase, if we decrease the holes depth by using soft PDMS, we turn its resolution issue into strength. Soft PDMS were also used because of its low young module (1MPa) that facilitates the demolding process leading to well defined cluster. The PDMS molds were characterized by atomic force microscopy and the Figure 4.6 shows the approximate depth for every lattice parameter.

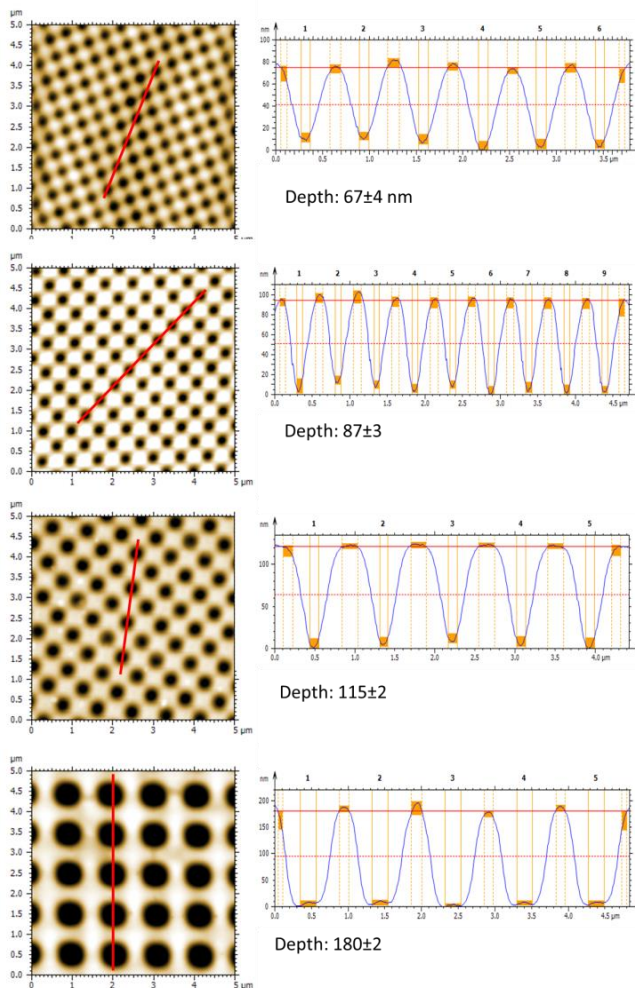*Figure 4.6 Atomic force microscopy images of patterns with L=400 nm, L=500 nm, L=600 nm, and L=740 nm. The replication process is more difficult for smaller lattice parameters, but in this size range still yields stamps suited for carrying out the assembly*

4.4 GOLD NANOSPHERES ASSEMBLY

To achieve template assembly of gold nanoparticles on a substrate we need highly concentrated solution with low surfactant content. As recently reported, PEG coated gold nanospheres (PEG-AuNSs) allows to keep surfactant cetyltrimethylammonium chloride (CTAC) far below its critical micellar concentration[37] thanks to the steric stabilization provided by the hydrophilic polymer that sufficiently protect the particles and prevented irreversible aggregation. This system avoids the coffee ring effect improving the final assembly homogeneity.

- *AuNSs functionalization*

PEGylation was typically done by setting the particles up to an Au^0 concentration of 10 mM (according to Abs_{400}, [38,39]) in 1 mM CTAC solution and adding 1 mg of solid PEG-6k-SH per mL dispersion. The ligand exchange took place overnight and was followed by centrifuge washing with 300 μM CTAC three times yielding the nanoparticles showed in Figure 4.7a. The related extinction is depicted in Figure 4.7b. After this stage, the particle concentration was increased up to 800 mM to create a stock dispersion.
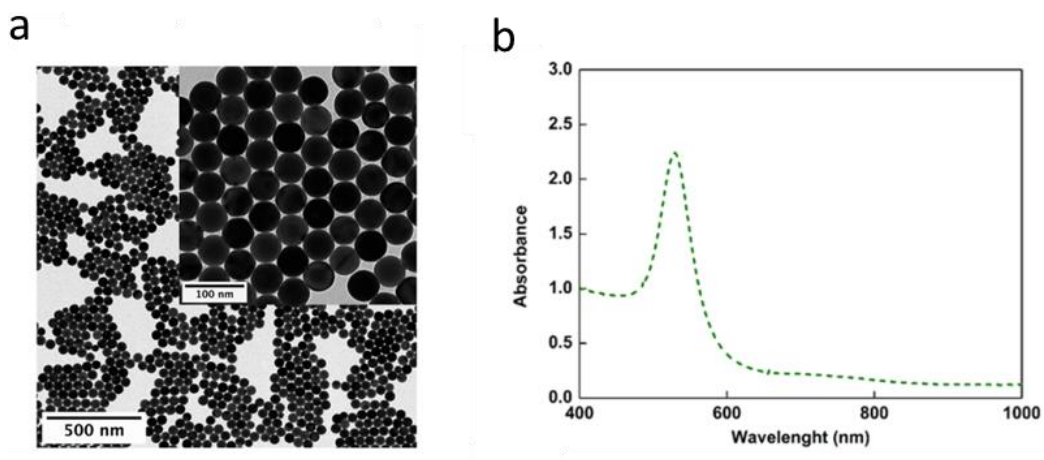

Figure 4.7. (a) Absorbance spectrum of gold nanospheres with a diameter of 52 nm dispersed in dilute CTAC solution. (b) TEM images of PEGylated AuNSs

- *Assembly*

Successful template-assisted self-assembly of AuNSs has been carried out by using PDMS molds featuring square array geometries with lattice parameters (*L*) of 400, 500, 600, 740 and 1600 nm, and hole diameters (*d*) of 230, 270, 330, 440 and 960 nm, respectively. Aliquots of the stock dispersion were diluted with suitable CTAC solutions to reach a final surfactant concentration of 50 μM and Au^0 concentrations between 13 and 90 mM. Figure 4.8a shows the colloidal solution of concentrated gold nanoparticles that forms a gold shimmer due to preassembly on the Eppendorf walls. This effect was a sing of the tendency of AuNSs to assemble and forms highly packed layers.[40] The supercrystals films in Figure 4.8c display iridescent colors under white light illumination, showing an angular dependence similar to that of the corresponding molds (Figure 4.8). Scanning electron microscopy (SEM) images (Figure 4.8) from representative samples put in evidence the long-range order of the AuNSs clusters on glass.
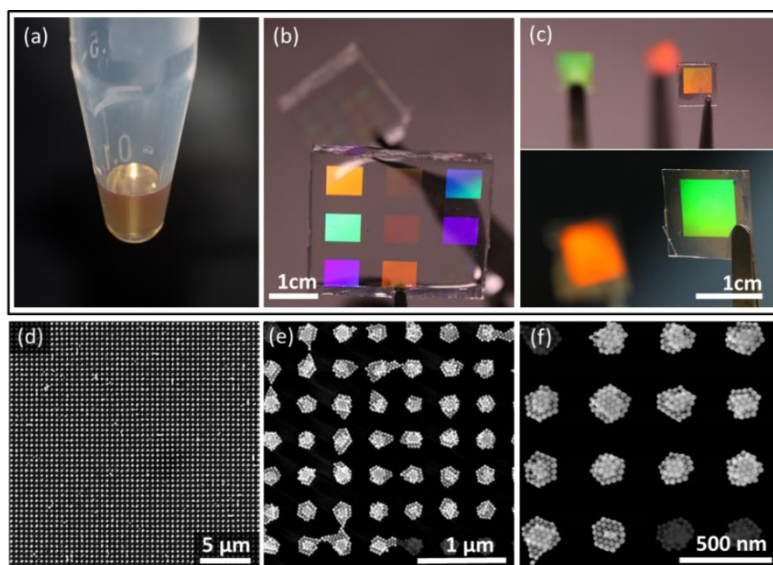

Figure 4.8. Upper panel: Photographs of a dispersion of AuNSs (a), the PDMS molds used for the assembly (b), and AuNSs assemblies obtained on glass (c). Lower panel: SEM micrographs of representative square lattice AuNSs clusters arrays of a representative sample at different magnifications (d-f).

It is worth noting that the AuNSs pack hexagonally within the clusters. That outcome is in accord with previously reported self-assembly and suggests an environment controlled reversible assembly.

- *Optimization: optical and morphological aspect*

In order to achieve tunable and intense plasmonic resonances we optimized the template-assembly conditions varying the concentration of colloidal AuNSs solution and checking the optical response. The Au^0 concentration calculated according to Abs_{400}[38] were used to estimate the AuNPs concertation. Regardless of the shape and size of the nanoparticles a value of 1.2 for the absorbance at 400 nm corresponds to a Au^0 concentration of 0.5 mM.[39] Another important parameter to consider when coming to this optimization process is the amount of particles per area that different cluster and array dimension can soak from the solution. In this regards we designed our plasmonic crystals so that the filling factor (FF) would be the same for each of the structures used. With filling factor, we refer to a geometrical parameter that estimates the percentage of effective area that can be covered with nanoparticles and is defined as:

$$FF = \frac{\pi R^2}{L^2},\qquad\qquad(1)$$

with R being the radius of the holes and L the lattice parameter. It yields $FF \sim 0.25 - 0.27$ for all of the employed stamp geometries.

Optical measurements (extinction=1-R-T, where R and T correspond to Reflectance and Transmittance spectra from the films) together with SEM inspection leads to an accurate fine tuning of the optimum concentration. Both of the analysis serves to evaluate the resulting supercrystals and identify the correlation between optical properties and morphological structures. We thus prepared assemblies with varying AuNSs concentrations and carried out the assembly as reported earlier in this chapter. Figure 4.9 show the extinction spectra and corresponding SEM micrographs of AuNSs organized into a square array with 500nm lattice parameter at different concentrations. The organized structure leads to the arising of new resonances that can be detected by optical microspectroscopy. Those new modes are associated to collective couplings and

are highly sensitive to array structural irregularities so they can be used to evaluate the homogeneity of the self-assembled supercrystal. Combined inspection of the morphology and the extinction spectra indicated that ordered assemblies with well-defined plasmon resonances were obtained for intermediate Au concentrations of about 33 - 40 mM.
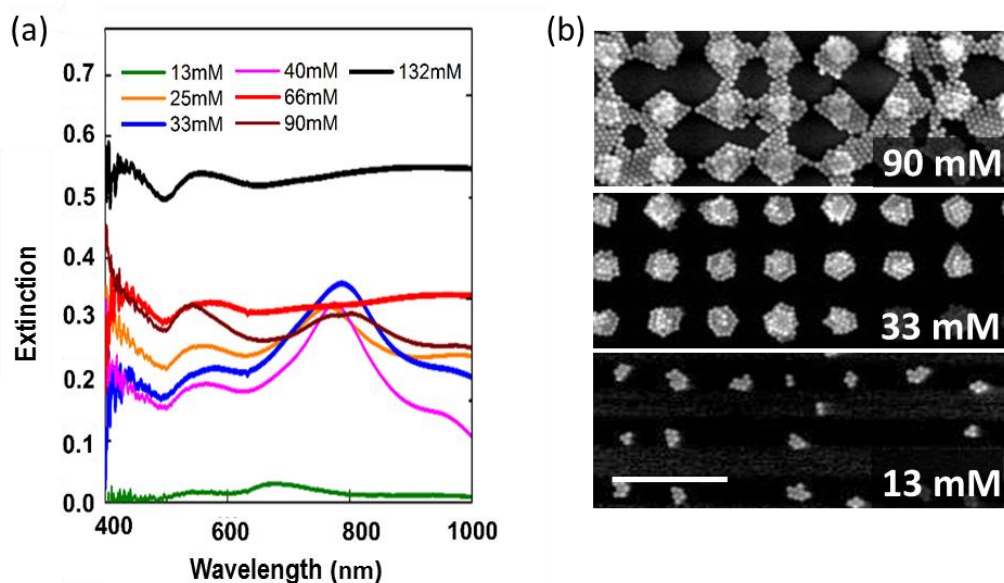
Figure 4.9. (a) Optical extinction spectra of supercrystals fabricated with different concentration form 13mM up to 132 mM. (b) SEM micrograph of three representative samples with 13, 33 and 90 mM concentration of initial colloidal solution. Scale bar 1 μm.

Lower concentrations resulted in incomplete clusters filling with broad resonances, whereas higher concentrations produced accumulation or bridging with additional AuNSs between clusters, accompanied by an increased optical background.

4.5 GOLD NANORODS ASSEMBLY

In the same fashion of nanospheres, highly concentered nanorods solution were achieved by (11-mercaptoundecyl)hexa(ethylene glycol) (MUHEG) coating that foster side-by-side organization of nanorods into structures with feature sizes

between 1 and 50 μm for assembly from aqueous dispersions, and allow to increase the colloidal concentration while keeping surfactant content low.[25]

- *AuNRs functionalization*

To functionalize the particles with MUHEG, the nanorods were centrifuged and redispersed in 1 mM CTAB, followed by addition of an equal amount of 200 μM aqueous MUHEG solution under vigorous agitation. After overnight storage, residual ligands were removed by centrifuge washing three times with 250 μM CTAB, whereby the dispersion volume was halved in each step. The cleaned dispersion was finally concentrated up by multiple centrifugation steps to reach to an Au^0 concentration of 1700 mM (according to Abs400). In general, the MUHEG-coated rods could be centrifuged safely with CTAB concentration as low 50 μM. Below that value irreversible particle aggregation started to occur.

- *Assembly*

Template-assisted self-assembly of AuNRs has been carried out by using PDMS molds featuring square array geometries with lattice parameters (*L*) of 400, 500, 600, 740 and 1600 nm, and hole diameters (*d*) of 230, 270, 330, 440 and 960 nm, respectively. Based on the previous studies[25] the gold nanorods concentration have been kept between 100 and 850 mM with 50 μM of CTAB. However, in this case, the low concentration of free surfactant was not enough to suppress the coffee-ring formation as depicted in Figure 4.10. Since the coffee ring depends on the evaporation rate, acting on this parameter we can control the stain formation. The strategy we followed was to use ethanol/water solution. PDMS is known to be hydrophobic so water droplets will not spread uniformly on the substrate. After studying different ethanol water mixture, we choose an aqueous solution with 40% of ethanol. The first consequence is the increased solution wettability which in turn leads to better spreading of the drop on the patterned surface and more homogeneous nanoparticles distribution. Furthermore, ethanol addition has been demonstrated to tune the evaporation speed rate reducing coffee-ring effect and foster the assembly though CTAB micelles solvation.
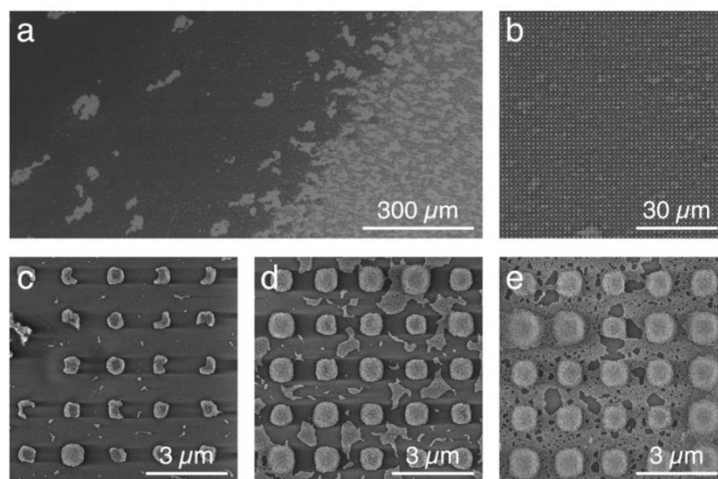
Figure 4.10 SEM images of a substrate prepared with the aqueous dispersion of AuNR. (a) Toward the rim of the substrate a strongly overfilled coffee ring builds up (Right side), whereas the substrate center remains strongly under filled or even empty (left side).The zoomed images in (c-e) were taken with the same magnification at different spots from inside toward the rim.

- *Effect of Ethanol:coffee-ring effect reduction though modified evaporation rate*

The bright shimmer discussed above for gold nanospheres (Figure 4.8a) was a sign of self-organization of nanoparticle in packed structures. Interestingly, at fixed temperature and humidity, this characteristic metallic luster was also observed on gold nanorods directly on the drop deposited on the PDMS mold after a composition-controlled induction period. As the alcohol/water mixture evaporates, the AuNRs concentrate and their distribution inside the drop changes. In this process the drying droplets modify their appearance from dark brown to golden within minutes indicating that AuNRs initiated to pre-assembly at the air/liquid interface, as illustrated in Figure 4.11.[41] This pre-assembly process, not observed in purely aqueous dispersions, was found to consistently start at the droplet rim that is the area of highest curvature and drying speed (Figure 4.11a). The golden surface layer then grows from the bottom to the top (Figure 4.11b) covering the entire liquid air interface (Figure 4.11c, d). After several minutes of waiting, during which more particles accumulate (Figure 4.11f-h) the largest fraction of ethanol has evaporated and the particles start to re-disperse partially near the rim (Figure 4.11i-l). Since this process in not observed in purely water solution and based on the liquid flows

in an evaporating drop demonstrated in previous work[29] we can ascribe the preassembly process to be driven by convection due to EtOH evaporation.[42]
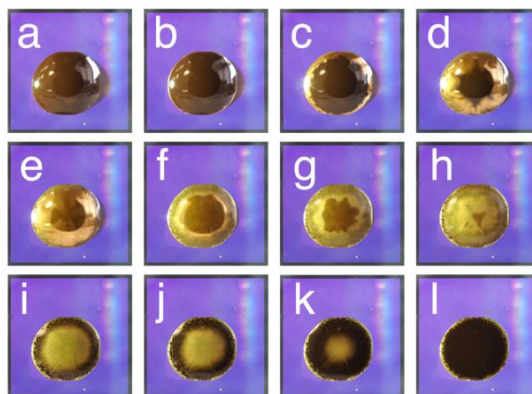

Figure 4.11. Photograph of droplets of EtOH/water colloidal dispersion of gold nanorods (100 mM Au[0] , 75% EtOH v/v) deposited on PDMS during the evaporation of ethanol. a) The first photography was taken approximately 25 s after droplet releasing, b: 34 s, c: 40 s, d: 45 s, e: 53 s, f: 108 s, g: 127 s, h: 147 s, i: 194 s, j: 210 s, k: 238 s, l: 297 s.

The macroscopic appearances of a droplet depicted in Figure 4.11 at selected stages of evaporation can be correlated with the resulting mesostructures demonstrating that different stages of preassembly leads to completely different outcome. This study unveils the relationship between the aggregation state of AuNRs at the air/liquid interface at the moment of contacting the substrate and the final particle distribution after drying. Figure 4.12show SEM measurements of substrate assembled at different evaporation times, for identical initial composition and volume of the dispersion. When interrupting the evaporation at early evaporation stage, most of the liquid was found to move toward the edge of the confined droplet, dragging the nanoparticles away (Figure 4.12a). The particles would then accumulate to form the characteristic coffee ring. In the opposite case, the evaporation stage is left for too long that leads to the appearance of extended nanoparticle aggregation which leads to overfilling of the central region (Figure 4.12d). In the other hand, the intermediate stage is found to slightly induce pre-assembly of nanorods with the formation of medium-sized lamellar AuNRs clusters that possess a moderate hydrodynamic mobility that hinder both the migration to the rim and

accumulation at the center of the stamp.[43] In general, the quality of the local array structure and the overall macroscopic surface homogeneity were optimal when the substrates were placed onto the stamp just before the surface of the droplets turned golden, condition represented in Figure 4.12c.
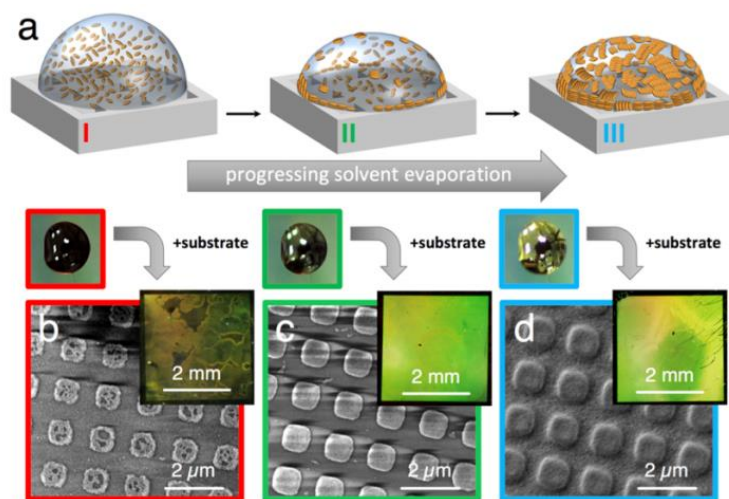

Figure 4.12 Influence of pre-evaporation and correlation between droplet appearance and the resulting assembly structure. (red frame) under filling, (green frame) optimal filling, (blue frame) vast overfilling.

As a result, the role of volatile solvent (ethanol) is found to be determinant in this the nanoparticle assembly system. Collectively, these results make a strong case for the idea that EtOH efficiently triggers the agglomeration and surface activity of AuNRs, thereby reducing particle mobility during drying and ultimately leading to a strongly altered self-assembly behavior. Similar trapping of nanoparticles at the liquid–air interface has been recognized as a method for reducing coffee stains and building highly ordered close-packed layers.[41]

- *Effect of the ethanol: induction of self-assembly*

Interestingly the presence of ethanol triggers the lying rod lamellae self-assembly rather the water solution induces side by side vertical aggregation as depicted in Figure 4.13. This effect suggests some sort of interactions at

molecular level so further studies have been done to unveil the possible assembly mechanism.
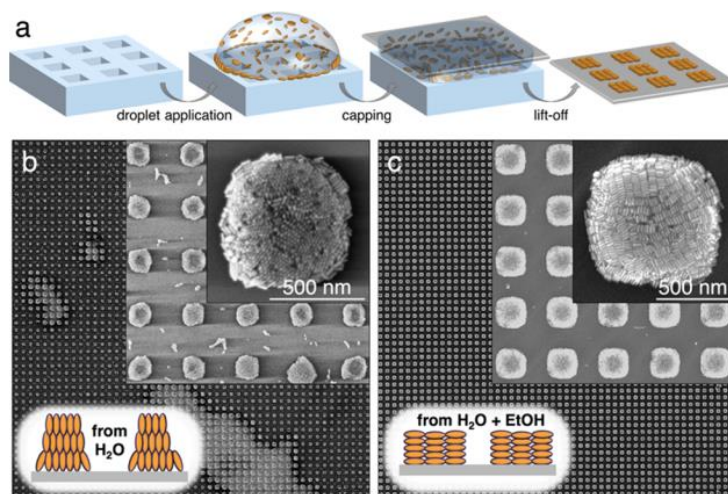

Figure 4.13 (a) Scheme of the patterning process (b) SEM micrographs of supercrystals obtained from MUHEG-coated AuNRs in aqueous dispersion. (c) Representative SEM micrograph of substrate obtained with the same particles dispersed in an EtOH/water mixture.

Ethanol is believed to strip away the excess cetyltrimetilammonium bromide micelles from the MUHEG/water interface. This mechanism increases the hydrophobicity of the particles triggering the nanoparticles assembly. To prove this mechanism we conducted ζ-potential and UV−vis spectroscopy measurements of AuNR colloids for varying CTAB and EtOH concentration. The surface charge of nanoparticles gives direct information on their stability so the tendency of nanorods to assemble. On the other hand the absorbance frequency unveils the formation of nanoparticles aggregates. In water, the particles exhibit a strongly positive ζ-potential, even far below the critical micelle concentration (cmc) of CTAB (1mM). This effect is illustrated in Figure 4.14 where the ζ-potential assumes values around +35 mV down to 100 μM of CTAB. With the addition of EtOH above 25% (v/v), the surface charge drops instantaneously, reaching 0 mV at 35% (v/v) and −10 mV at 45% (v/v) EtOH (Figure 4.14c). These data support the hypothesis that, in water, CTAB micelles remain bound to the AuNR−MUHEG interface far below the cmc ([CTAB] ≥ 30

μM) but are readily removed by EtOH. The resulting loss of colloidal stability is mirrored in the UV–vis spectra showing peaks around 600 nm that are characteristic for side-to-side aggregation of AuNRs.[44]

These changes enable a nearly complete suppression of the coffee ring formation, demonstrating the possibility to obtain a well-defined AuNR arrays over large areas. It is worth noting that ethanol-containing AuNRs dispersions that yield high-quality assemblies displayed, on the Eppendorf walls, a macroscopic appearance of bright metallic luster already observed in PEG-AuNSs used in the previous work (Figure 4.8a). This effect indicates the presence of ordered assembled monolayers. Ethanol-containing AuNR dispersions yielding high-quality assemblies displayed a macroscopic appearance reminiscent of previously described PEG–AuNSs dispersions. This effect was not observed in purely aqueous solution suggesting that ethanol also have a role in stabilizing the assembled structure. Thus, it suggests that the stimulation of preassembly provided by ethanol helps the formation of high ordered, clean and homogeneous supercrystals.
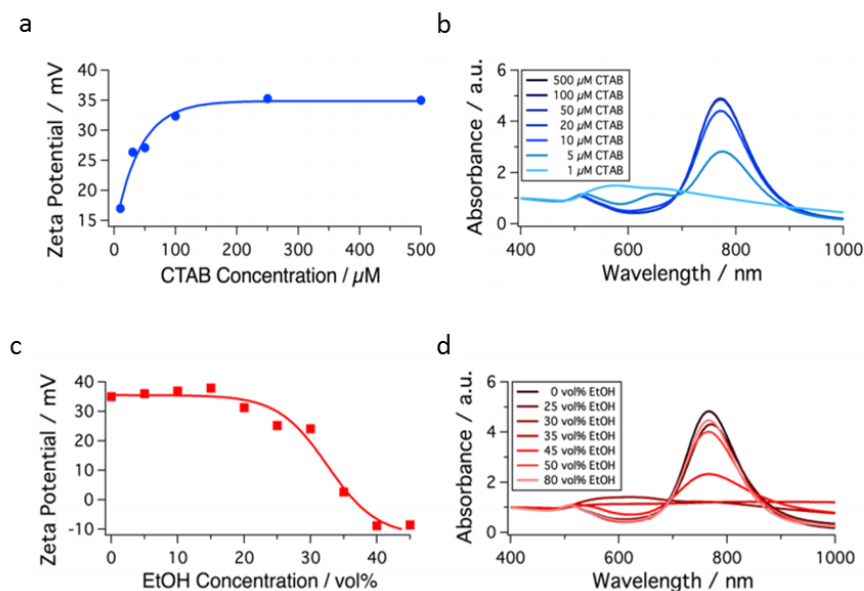

Figure 4.14. (a) ζ-potential trend with the amount of EtOH in solution (c) UV–vis spectroscopy measurements that show the fast agglomeration of the AuNRs at intermediate EtOH concentrations of 30–45% (v/v).

4.6 TUNABLE OPTICAL PROPERTIES OF AUNPS SUPERCRYSTALS

The introduction of superordinate periodic patterns can give rise to additional diffractive resonances due to optical far-field interactions. These so-called lattice plasmon modes can be tuned over a wide frequency range by varying lattice parameters and have been reported to yield remarkably sharp resonances.[27,45,46] Intriguingly, Reinhard *et al.* were able to demonstrate within micrometer-sized areas, the effect of the e-field enhancement of periodic nanoparticle cluster arrays on the intensity of the SERS signal.[20,47] The ability of tuning the frequency of these hybrid plasmonic-photonic resonances further enables nanophotonic device engineering.[23] The challenge resides in fabricating hierarchical assemblies that operate at visible wavelengths. In this work we try to overcome this limitation by fabricating large area plasmonic superlattices with optical resonances tailored for specific visible and near infrared lasers.

- *Tunable gold nanospheres supercrystals*

The influence of the array periodicity on the optical response was studied using assemblies with lattice parameters ranging from 400 to 1600 nm, made from dispersions with optimized gold concentration. Representative SEM images and extinction spectra of the resulting cluster arrays are displayed in Figure 4.15. From inspection of the optical spectra, two main regions can be identified: the first region at lower wavelengths shows a local extinction maximum at λ~560 nm. This peak is close to the dipolar mode of a single AuNS (λ_{LSPR} = 532 nm in water) and is likely influenced by higher order coupling modes of the clusters, which are typically observed for interparticle distances smaller than 2 nm.[27,48] When the NSs within the clusters are closer to each other, a stronger degree of plasmon coupling can be expected, and higher order cluster modes appear at energies close to the single particle LSPR. These higher order cluster modes, which have been discussed in previous works,[27,48] can shift the peak to λ~560 nm.[18,49] The second region at higher wavelengths displays the most intense extinction peak and clearly red-shifts when increasing the lattice parameter of the assembly. The strong correlation of the latter extinction peak

with the lattice parameter indicates that this resonance originates from the hybridization of the plasmonic cluster modes with the diffractive lattice mode.
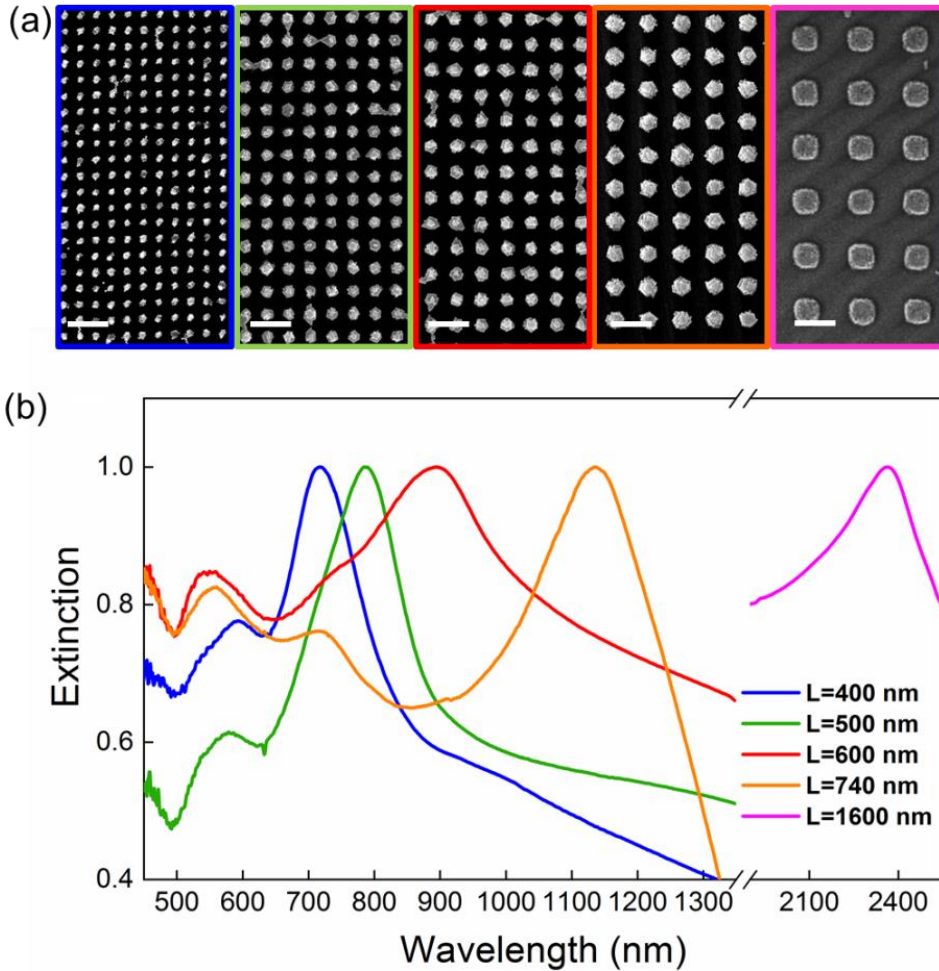
Figure 4.15. Structural and optical characterization of supercrystal assemblies with varying lattice parameter L. (a) SEM micrographs of gold nanoparticle arrays with different lattice parameters: from left to right L=400 nm, L=500 nm, L=600 nm, L=740 nm, and L=1600 nm. (b) Extinction spectra, normalized to the maximum, of AuNS cluster arrays with different lattice parameters (see labels). Scale bar: 1 µm.

- *Tunable gold nanorods supercrystals*

The same approach has been applied to produce plasmonic crystals from Au nanorods using the solvent mixture EtOH:Water to mitigate the coffee ring effect and induce the assembly (Figure 4.16). For micron lattice parameters the

best array quality is achieved with high particle concentrations (up to 850 mM Au^0) and very short induction periods (below 15 s), whereas sub-micrometer lattice parameters (b–d) exhibit good filling for much lower particle concentrations (around 100 mM Au^0) when combined with intermediate pre-assembly times (around 45 s).
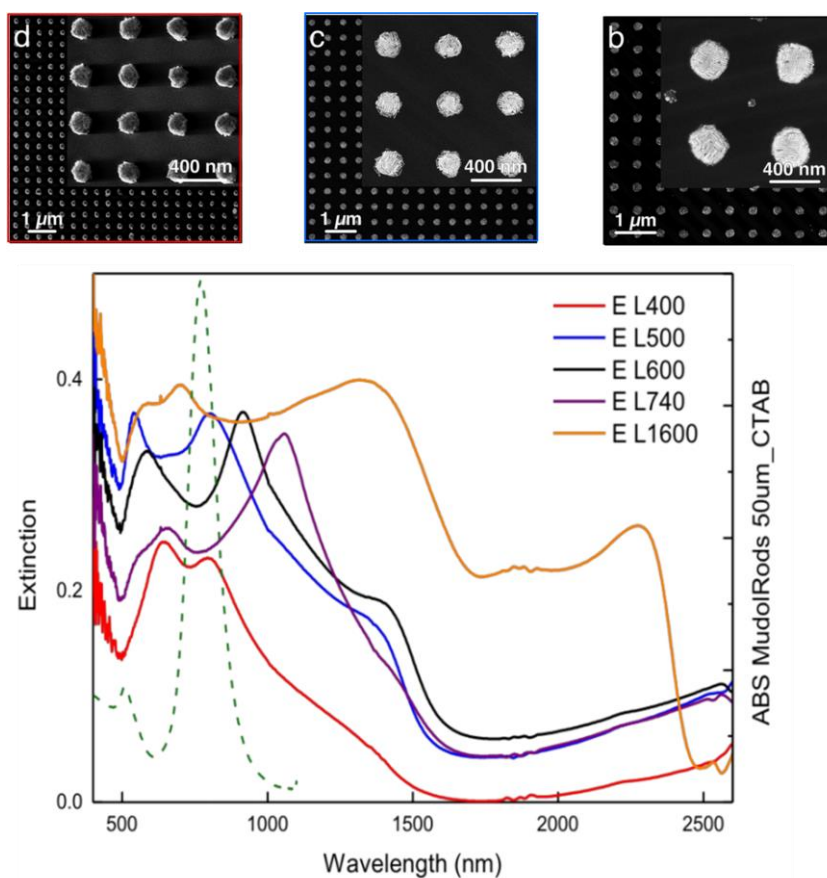
Figure 4.16. Feature size variation from 10 μm to 200 nm. Lattice parameters from (a–d): 20 μm, 600, 500, and 400 nm). The inset shows (a), parallel lamellae of lying rods spanning over several micrometers. (b-d) a side-by-side arrangement of AuNRs.

Optical properties are depicted in **¡Error! No se encuentra el origen de la referencia.**. At first look they do not seem more complicated that the ones form nanospheres arrays and can be easily identified a clear resonance red shift while increasing the lattice parameter. However, nanorods extinction presents two peaks ascribed to longitudinal and transverse LSPR. Therefore near filed

coupling leads to a complex environment that needs further investigation in order to associate each resonance to a specific physical phenomenon.

This technique paves the way to highly regular AuNPs arrays with feature sizes ranging from 200 nm up to tens of microns.

4.7 HYBRID RESONANCES IN AUNPS SUPERCRYSTALS

These resonances, launched by light diffracted by the grating, are typically called surface lattice resonances,[50] and are usually observed near a Rayleigh anomaly, *i.e.,* a change in the magnitude of the reflectivity associated with the onset of diffraction from the grating.[51] Rayleigh anomalies are grazing waves propagating in the plane of the array. Since the electromagnetic field tends to concentrate in the regions with the highest refractive index the light scattered at the Rayleigh anomaly propagates in the glass. As a consequence hybridization of the collective surface plasmon resonances from the AuNSs clusters with the lattice modes is dominated by the refractive index of the substrate as depicted in Figure 4.17.[52,53]
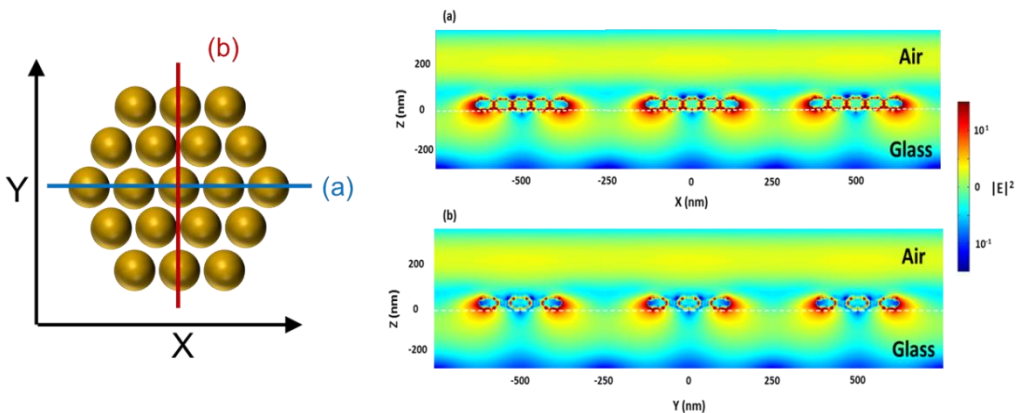
Figure 4.17 FDTD calculations of the electric field intensity $|E|^2$ transversal cuts for periodic cluster arrays, for L=500 nm, with electric field at x-direction polarization (a) and y-direction polarization (b), showing the interaction through the glass substrate.

This implies that the wavelength position of the lattice modes can be predicted *via* a Bragg law, corresponding to the first order of diffraction, under normal incidence for a square lattice

$$\lambda_{max} \simeq L n_{sub}$$

where n_{sub} is the refractive index of the substrate and L corresponds to the center to-center distance between neighboring posts. This formula fits very accurately with the positions of the extinction maxima where distinct resonance peaks arise near the predicted position of the Rayleigh anomaly.

4.8   CONCLUSIONS

Self-assembly of metal colloids is of great interest in the field of plasmonics mainly due to the possibility to tailor the optical properties of metal nanoparticles. We have demonstrated the template self-assembly of gold nanoparticles into hierarchically organized plasmonic mesostructures by using patterned PDMS molds as templates. As a result, we achieved regular square arrays of hexagonally packed gold nanospheres and lying lamellae gold nanorods, reaching periodicities down to 400 nm and feature sizes of 200 nm, over areas up to 1 cm^2. This study resolves some central issues of self-assembly by bridging vastly different length scales from nanometer to millimeter dimensions without losing reproducibility and homogeneity. A comprehensive study has been carried out to optimize the process condition depending of the nature of building blocks. The optimization shed light on the self-assembly process and introduced a new mechanism that is triggered by the presence of ethanol as solvents. The latter parameter has been extensively studied to produce highly ordered gold nanorods supercrystals on the scale of couple hundred nanometers.

These two-dimensional supercrystals exhibited well-defined collective plasmon modes that can be tuned throughout the visible and NIR ranges by changing lattice constant and array geometry. Further theoretical modeling confirmed that the resonances originate from the hybridization of photonic lattice modes with plasmonic resonances sustained by individual AuNPs clusters.

In the next chapter we will show how these tunable optical properties can be used to tailor surface enhanced Raman spectroscopy substrates for specific laser lines. We will then highlight the role of the hybrid photonic plasmonic

modes to the overall enhancement of the Raman scattering. Exploitation of these lattice resonances in SERS spectroscopy demands precise matching of the plasmon frequency with the wavelength of the excitation laser. We will study the efficiency of systems featuring different lattice parameters highlighting the condition to enhance the electric field confinement that directly translate into better SERS performance.

4.9 REFERENCES

(1)   Yan, W.; Xu, L.; Xu, C.; Ma, W.; Kuang, H.; Wang, L.; Kotov, N. A. Self-Assembly of Chiral Nanoparticle Pyramids with Strong *R* / *S* Optical Activity. *J. Am. Chem. Soc.* **2012**, *134*, 15114–15121.

(2)   Azharuddin, M.; Zhu, G. H.; Das, D.; Ozgur, E.; Uzun, L.; Turner, A. P. F.; Patra, H. K. A Repertoire of Biomedical Applications of Noble Metal Nanoparticles. *Chem. Commun.* **2019**, *55*, 6964–6996.

(3)   Vinci, G.; Rapa, M. Noble Metal Nanoparticles Applications: Recent Trends in Food Control. *Bioengineering*. MDPI AG January 22, 2019.

(4)   Furube, A.; Hashimoto, S. Insight into Plasmonic Hot-Electron Transfer and Plasmon Molecular Drive: New Dimensions in Energy Conversion and Nanofabrication. *NPG Asia Mater.* **2017**, 454.

(5)   Huang, X.; El-Sayed, I. H.; Qian, W.; El-Sayed, M. A. Cancer Cell Imaging and Photothermal Therapy in the Near-Infrared Region by Using Gold Nanorods. *J. Am. Chem. Soc.* **2006**, *128*, 2115–2120.

(6)   Ke, S. X.; Zhang, X.; Du, A.; Zhu, H.; Jia, J.; Wang, J.; Ke, X. As Featured in: Surface Plasmon-Enhanced Zeolite Catalysis under Light Irradiation and Its Correlation with Molecular Polarity of Reactants. *Chem. Commun. Chem. Commun* **2014**, *50*, 13893–13895.

(7)   Luk'Yanchuk, B.; Zheludev, N. I.; Maier, S. A.; Halas, N. J.; Nordlander, P.; Giessen, H.; Chong, C. T. The Fano Resonance in Plasmonic Nanostructures and

Metamaterials. *Nat. Mater.* **2010**, *9*, 707–715.

(8)   Solís, D. M.; Taboada, J. M.; Obelleiro, F.; Liz-Marzán, L. M.; García de Abajo, F. J. Optimization of Nanoparticle-Based SERS Substrates through Large-Scale Realistic Simulations. *ACS photonics* **2017**, *4*, 329–337.

(9)   Scarabelli, L.; Coronado-Puchau, M.; Giner-Casares, J. J.; Langer, J.; Liz-Marzán, L. M. Monodisperse Gold Nanotriangles: Size Control, Large-Scale Self-Assembly, and Performance in Surface-Enhanced Raman Scattering. *ACS Nano* **2014**, *8*, 5833–5842.

(10)   Jimenez de Aberasturi, D.; Serrano-Montes, A. B.; Langer, J.; Henriksen-Lacey, M.; Parak, W. J.; Liz-Marzán, L. M. Surface Enhanced Raman Scattering Encoded Gold Nanostars for Multiplexed Cell Discrimination. *Chem. Mater.* **2016**, *28*, 6779–6790.

(11)   Lee, H.-E.; Ahn, H.-Y.; Mun, J.; Lee, Y. Y.; Kim, M.; Cho, N. H.; Chang, K.; Kim, W. S.; Rho, J.; Tae Nam, K. Amino-Acid-and Peptide-Directed Synthesis of Chiral Plasmonic Gold Nanoparticles. **2018**.

(12)   Yang, A.; Hryn, A. J.; Bourgeois, M. R.; Lee, W.-K.; Hu, J.; Schatz, G. C.; Odom, T. W. Programmable and Reversible Plasmon Mode Engineering.

(13)   Willets, K. A.; Van Duyne, R. P. Localized Surface Plasmon Resonance Spectroscopy and Sensing. *Annu. Rev. Phys. Chem* **2007**, *58*, 267–297.

(14)   Kociak, M.; Stéphan, O. Mapping Plasmons at the Nanometer Scale in an Electron Microscope. *Chem. Soc. Rev.* **2014**, *43*, 3865.

(15)   Ding, S.-J.; Nan, F.; Liu, X.-L.; Hao, Z.-H.; Zhou, L.; Zeng, J.; Xu, H.-X.; Zhang, W.; Wang, Q.-Q. Plasmon-Modulated Excitation-Dependent Fluorescence from Activated CTAB Molecules Strongly Coupled to Gold Nanoparticles OPEN. **2017**.

(16)   Wang, W.; Ramezani, M.; Väkeväinen, A. I.; Törmä, P.; Gómez Rivas, J.; Odom, T. W. The Rich Photonic World of Plasmonic Nanoparticle Arrays. **2017**.

(17)   Hentschel, M.; Dregely, D.; Vogelgesang, R.; Giessen, H.; Liu, N. Plasmonic Oligomers: The Role of Individual Particles in Collective Behavior. *ACS Nano* **2011**, *5*, 2042–2050.

(18)   Greybush, N. J.; Liberal, I.; Malassis, L.; Kikkawa, J. M.; Engheta, N.; Murray, C. B.; Kagan, C. R. Plasmon Resonances in Self-Assembled Two-Dimensional Au Nanocrystal Metamolecules. *ACS Nano* **2017**, *11*, 2917–2927.

(19)   Volk, K.; Fitzgerald, J. P. S.; Ruckdeschel, P.; Retsch, M.; König, T. A. F.; Karg, M. Reversible Tuning of Visible Wavelength Surface Lattice Resonances in Self-Assembled Hybrid Monolayers. *Adv. Opt. Mater.* **2017**, *5*.

(20)   Yan, B.; Thubagere, A.; Premasiri, W. R.; Ziegler, L. D.; Negro, L. D.; Reinhard, B. M. Engineered SERS Substrates with Multiscale Signal Enhancement: Nanoparticle Cluster Arrays. *ACS Nano* **2009**, *3*, 1190–1202.

(21)   Strobbia, P.; Languirand, E.; Cullum, B. M. Recent Advances in Plasmonic Nanostructures for Sensing: A Review. *Opt. Eng.* **2015**, *54*, 100902.

(22)   Kraus, T.; Malaquin, L.; Schmid, H.; Riess, W.; Spencer, N. D.; Wolf, H. Nanoparticle Printing with Single-Particle Resolution. *Nat. Nanotechnol.* **2007**, *2*, 570–576.

(23)   Wang, D.; Yang, A.; Hryn, A. J.; Schatz, G. C.; Odom, T. W. Superlattice Plasmons in Hierarchical Au Nanoparticle Arrays. *ACS Photonics* **2015**, *2*, 1789–1794.

(24)   Hamon, C.; Sanz-Ortiz, M. N.; Modin, E.; Hill, E. H.; Scarabelli, L.; Chuvilin, A.; Liz-Marzán, L. M. Hierarchical Organization and Molecular Diffusion in Gold Nanorod/Silica Supercrystal Nanocomposites. *Nanoscale* **2016**, *8*, 7914–7922.

(25)   Hamon, C.; Novikov, S.; Scarabelli, L.; Basabe-Desmonts, L.; Liz-Marzá, L. M. Hierarchical Self-Assembly of Gold Nanoparticles into Patterned Plasmonic Nanostructures. **2014**, *8*, 10694–10703.

(26)   Yin, Y.; Lu, Y.; Gates, B.; Xia, Y. Template-Assisted Self-Assembly: A Practical

Route to Complex Aggregates of Monodispersed Colloids with Well-Defined Sizes, Shapes, and Structures. *J. Am. Chem. Soc.* **2001**, *123*, 8718–8729.

(27)   Hanske, C.; Tebbe, M.; Kuttner, C.; Bieber, V.; Tsukruk, V. V; Chanana, M.; König, T. A. F.; Fery, A. Strongly Coupled Plasmonic Modes on Macroscopic Areas via Template-Assisted Colloidal Self-Assembly. *Nano Lett.* **2014**, *14*, 6863–6871.

(28)   Hanske, C.; González-Rubio, G.; Hamon, C.; Formentín, P.; Modin, E.; Chuvilin, A.; Guerrero-Martínez, A.; Marsal, L. F.; Liz-Marzán, L. M. Large-Scale Plasmonic Pyramidal Supercrystals via Templated Self-Assembly of Monodisperse Gold Nanospheres. *J. Phys. Chem. C* **2017**, *121*, 10899–10906.

(29)   Deegan, R. D.; Bakajin, O.; Dupont, T. F.; Huber, G.; Nagel, S. R.; Witten, T. A. Capillary Flow as the Cause of Ring Stains from Dried Liquid Drops. *Nature* **1997**, *389*, 827–829.

(30)   Wang, W.; Yin, Y.; Tan, Z.; Liu, J. Coffee-Ring Effect-Based Simultaneous SERS Substrate Fabrication and Analyte Enrichment for Trace Analysis. *Nanoscale* **2014**, *6*, 9588–9593.

(31)   Choi, S.; Stassi, S.; Pisano, A. P.; Zohdi, T. I. Coffee-Ring Effect-Based Three Dimensional Patterning of Micro/Nanoparticle Assembly with a Single Droplet. *Langmuir* **2010**, *26*, 11690–11698.

(32)   Lone, S.; Zhang, J. M.; Vakarelski, I. U.; Li, E. Q.; Thoroddsen, S. T. Evaporative Lithography in Open Microfluidic Channel Networks. *Langmuir* **2017**, *33*, 2861–2871.

(33)   Hanske, C.; González-Rubio, G.; Hamon, C.; Formentín, P.; Modin, E.; Chuvilin, A.; Guerrero-Martínez, A.; Marsal, L. F.; Liz-Marzán, L. M. Large-Scale Plasmonic Pyramidal Supercrystals via Templated Self-Assembly of Monodisperse Gold Nanospheres. *J. Phys. Chem. C* **2017**, *121*, 10899–10906.

(34)   Scarabelli, L.; Grzelczak, M.; Liz-Marzán, L. M. Tuning Gold Nanorod Synthesis

through Prereduction with Salicylic Acid. *Chem. Mater.* **2013**, *25*, 4232–4238.

(35)   Xia, Y.; Rogers, J. A.; Paul, K. E.; Whitesides, G. M. Unconventional Methods for Fabricating and Patterning Nanostructures. *Chem. Rev* **1999**, *99*, 1823–1848.

(36)   Qin, D.; Xia, Y.; Whitesides, G. M. Soft Lithography for Micro- and Nanoscale Patterning. *Nat. Protoc.* **2010**, *5*, 491–502.

(37)   NOMURA, T.; ASAI, Y.; MURAHASHI, N.; IWAMOTO, K. Formation of Spherical Micelles by the Novel Platelet Activating Factor Receptor Antagonist, E5880. *Chem. Pharm. Bull. (Tokyo).* **2000**, *48*, 947–950.

(38)   Rodríguez-Lorenzo, L.; Álvarez-Puebla, R. A.; García de Abajo, F. J.; Liz-Marzán, L. M. Surface Enhanced Raman Scattering Using Star-Shaped Gold Colloidal Nanoparticles. *J. Phys. Chem. C* **2010**, *114*, 7336–7340.

(39)   Scarabelli, L.; Sánchez-Iglesias, A.; Pérez-Juste, J.; Liz-Marzán, L. M. A "Tips and Tricks" Practical Guide to the Synthesis of Gold Nanorods. *J. Phys. Chem. Lett.* **2015**, *6*, 4270–4279.

(40)   Bian, K.; Schunk, H.; Ye, D.; Hwang, A.; Luk, T. S.; Li, R.; Wang, Z.; Fan, H. Formation of Self-Assembled Gold Nanoparticle Supercrystals with Facet-Dependent Surface Plasmonic Coupling. *Nat. Commun.* **2018**, *9*.

(41)   Bigioni, T. P.; Lin, X.-M.; Nguyen, T. T.; Corwin, E. I.; Witten, T. A.; Jaeger, H. M. Kinetically Driven Self Assembly of Highly Ordered Nanoparticle Monolayers. *Nat. Mater.* **2006**, *5*, 265–270.

(42)   Deegan, R. D.; Bakajin, O.; Dupont, T. F.; Huber, G.; Nagel, S. R.; Witten, T. A. Contact Line Deposits in an Evaporating Drop. *Phys. Rev. E* **2000**, *62*, 756–765.

(43)   Kim, H.; Boulogne, F.; Um, E.; Jacobi, I.; Button, E.; Stone, H. A. Controlled Uniform Coating from the Interplay of Marangoni Flows and Surface-Adsorbed Macromolecules. **2016**.

(44)   Funston, A. M.; Novo, C.; Davis, T. J.; Mulvaney, P. Plasmon Coupling of Gold Nanorods at Short Distances and in Different Geometries. *Nano Lett.* **2009**, *9*,

1651–1658.

(45)   Wang, D.; Yang, A.; Wang, W.; Hua, Y.; Schaller, R. D.; Schatz, G. C.; Odom, T. W. Band-Edge Engineering for Controlled Multi-Modal Nanolasing in Plasmonic Superlattices. *Nat. Nanotechnol.* **2017**, *12*, 889–894.

(46)   Volk, K.; Fitzgerald, J. P. S.; Ruckdeschel, P.; Retsch, M.; König, T. A. F.; Karg, M. Reversible Tuning of Visible Wavelength Surface Lattice Resonances in Self-Assembled Hybrid Monolayers. *Adv. Opt. Mater.* **2017**, *5*, 1600971.

(47)   Yan, B.; Boriskina, S. V.; Reinhard, B. M. Design and Implementation of Noble Metal Nanoparticle Cluster Arrays for Plasmon Enhanced Biosensing. *J. Phys. Chem. C* **2011**, *115*, 24437–24453.

(48)   Yoon, J. H.; Selbach, F.; Langolf, L.; Schlücker, S. Ideal Dimers of Gold Nanospheres for Precision Plasmonics: Synthesis and Characterization at the Single-Particle Level for Identification of Higher Order Modes. *Small* **2018**, *14*.

(49)   Bao, K.; Mirin, N. A.; Nordlander, P. Fano Resonances in Planar Silver Nanosphere Clusters. *Appl. Phys. A* **2010**, *100*, 333–339.

(50)   Guo, R.; Hakala, T. K.; Törmä, P. Geometry Dependence of Surface Lattice Resonances in Plasmonic Nanoparticle Arrays. *Phys. Rev. B* **2017**, *95*, 155423.

(51)   Khlopin, D.; Laux, F.; Wardley, W. P.; Martin, J.; Wurtz, G. A.; Plain, J.; Bonod, N.; Zayats, A. V.; Dickson, W.; Gérard, D. Lattice Modes and Plasmonic Linewidth Engineering in Gold and Aluminum Nanoparticle Arrays. *J. Opt. Soc. Am. B* **2017**, *34*, 691.

(52)   Auguié, B.; Bendaña, X. M.; Barnes, W. L.; García de Abajo, F. J. Diffractive Arrays of Gold Nanoparticles near an Interface: Critical Role of the Substrate. *Phys. Rev. B* **2010**, *82*, 155447.

(53)   Le Ru, E.; Etchegoin, P. Principles of Surface Enhanced Raman Spectroscopy and Related Plasmonic Effets. *Elsevier* **2009**, *1*, 1–663.

TUNABLE PLASMONIC SUPERCRYSTAL FOR SERS

N anomaterials and nanotechnology are new fields of science and technology. However, nanotechnology is expected to dramatically change operating characteristics of chemical sensors and will probably gain in importance in all fields of sensor application over the next ten to twenty years. It has been found that with reduction in size, novel electrical, mechanical, chemical, catalytic and optical properties can be introduced. Besides it was established that 1-D structures can be ideal system for studying the nature of chemical sensing effects. Nanotechnology enables us to create functional materials, devices, and systems by controlling matter at the atomic and molecular scales, and to exploit novel properties and phenomena. Consider that most chemical and biological sensors, as well as many physical sensors, depend on interactions occurring at these levels and you'll get an idea of the effect nanotechnology will have on the sensor world.

The discovery of the enhancement of Raman scattering by molecules adsorbed on nanostructured metal surfaces is a landmark in the history of spectroscopic and analytical techniques. Significant experimental and theoretical effort has been directed toward understanding the surface-enhanced Raman scattering (SERS) effect and demonstrating its potential in various types of ultrasensitive sensing applications in a wide variety of fields.

~ ● ~

5.1   INTRODUCTION

Ultrasensitive molecular detection and specific quantification of analytes have been leading motivations in the development of advanced spectroscopic techniques.[1] Raman spectroscopy, which probes vibrational transitions, allows the label-free identification of a wide variety of molecules, thereby becoming a highly relevant tool in disciplines including biology, medicine, or forensics.[2–4] However, the extremely low cross section of Raman scattering usually requires either large amounts of analyte or very powerful laser sources since the scattering cross section is proportional to the incoming electric fiend intesity.[5] One way to enhance the Raman signal is to place molecules into a modified environment where the electric field is enhanced, typically a corrugated metal surface. The incoming light as well as the scattered outcome, that carries the vibrational information, would then be enhanced several hundreds of times. Thanks to these enhancements we were able to report sensing techniques that reach sensitivity up to single molecule detection.[6,7] The main mechanism behind the observed huge SERS signals is the electromagnetic enhancement provided by metallic nanostrucutres.[8] A molecule located in the proximity of a plasmonic nanoparticle whose plasmon is being excited, experiences a much higher electric field, which is translated into a higher Raman scattering signal. Close-packed metal nanoparticles further increase the SERS performance.[9,10] Direct writing techniques like e-beam or focused ion beam lithography can be used to obtain nanoparticle arrangements with the nanometer-sized gaps necessary for SERS, but are very inefficient in terms of time and cost.[11] Therefore, self-assembly of chemically synthesized plasmonic nanoparticles is often utilized for substrate preparation. Methods as simple as drop casting or precipitation of colloidal dispersions may yield assemblies that are able to sufficiently amplify Raman cross sections and enable even single molecule detection,[12–14] which however usually comes at the cost of poor signal reproducibility.[15,16] Strategies for preparing homogeneously structured nanoparticle films by template-assisted self-assembly have been improved significantly over the last decade, now having the potential to solve the above mentioned issues.[17–20] These substrates have been employed, for example, in the

detection of gases like carbon monoxide or pyrene,[21,22] as well as in monitoring the expression of bacterial quorum sensing molecules *via* SERS.[23]

In this chapter periodic arrays of well-defined plasmonic clusters with different lattice parameters will be used to tailor SERS sensor for specific laser lines. We will take advantage of tunable resonances in sub micrometer plasmonic crystals array fabricated by template self-assembly. The interaction between diffractive modes and localized plasmon resonances in the visible/NIR range will boost the intensity of plasmonic resonances that in turn lead to higher SERS signal. A detailed investigation will be carried out to characterize those substrates taking into account the manifold factors determining the overall field enhancement in these assemblies, such as cluster dimensions, lattice parameters, number of layers, and the overall degree of order. Finally FDTD simulations will help to unveil and understand the origins of the enhancement corroborating the original idea.

5.2 ENGINEERING NANOPARTICLES SUPERCRYSTALS FOR SERS

The possibility to exploit the multiple electric filed enhancement provided by metal nanostructures relies on the match of the laser wavelength used for SERS with the resonance frequency of plasmonic nanoparticles. Whether for laser excitation in the UV/Vis part of the spectra this requirement is easily fulfilled, when working with low energy wavelength this becomes challenging. The infrared laser at 785nm fits the first biological optical transparency window, thus providing better light penetration in biological tissues, and is particularly interesting for biomolecular detection in complex media. The nanoparticle's LSPR can be easily tuned with their size and shape, however when moving the resonances towards the infrared by increasing the nanoparticle size the intensity of electric field per volume diminish leading to worst performance in SERS. Thus, the overall efficiency drops dramatically. On the other hand, if smaller nanoparticles with resonances in the visible are brought together interesting phenomena such plasmon near field coupling occurs. As a result, a new pool of resonances arise at the so-called hotspots (nanometric volume

region of high intensity electric field) generated in the nanogaps in between the particles.
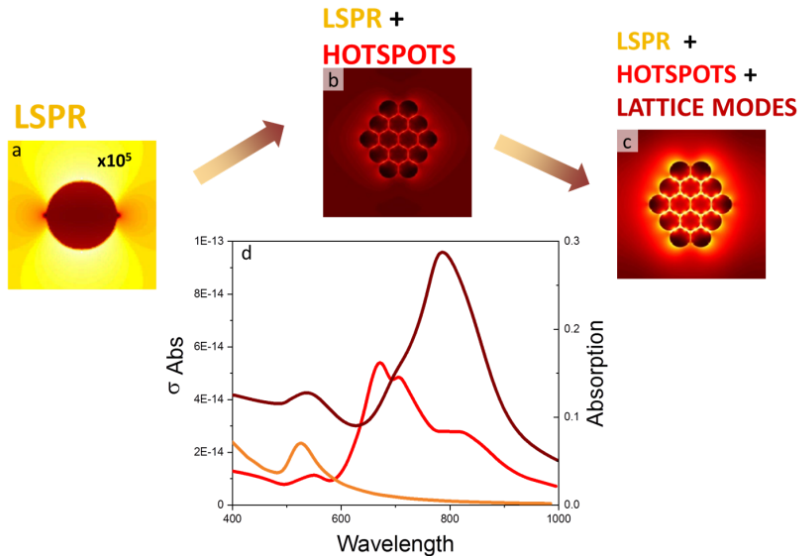

Figure 5.1 Scketch of the hotspot engineering. a-c) electric filed mapping of plasmonic resonances at their maximum absorttion crossserction. The single LSPR of isolated nanoaprticle is enhaced when creating hotspots. The further organization of nanoparticle cluster nto ordered arrays leads to highe electromagnetinc filed intesity corroborating the idea to fabricate gold nanoparticle supercrystals for high performace SERS sensors. (d) Numerical simulation of absorttion cross section od silgle nanoparticel (orange line) and nanoaprticles cluster red line; dark red asborption of cluster array with lattice 500nm.

This method squeezes the oscillating electron in nanometric volumes increasing the absorption cross-section by hundreds of times in relation with single nanoparticles (Figure 5.1). Despite the high efficiency demonstrated in several works as a SERS sensor, this system is often not optimized so a concrete design of hotspot excitation could lead to better SERS performances.

Our design aims to engineer lattices modes in a way in which they can couple effectively with the multi frequency localized surface plasmon resonances typical of nanoparticle enables in order to enhance only specific wavelengths of the spectra. This mechanism leads to higher electric filed enhancement that can be also easily tuned by changing the lattice parameter of the array.

5.3   SUPERCRYSTALS PERFORMANCES AS SERS SENSORS

With the support of the theoretical results, we studied the correlation between plasmon resonances sustained by the different geometrical assemblies and their performance as SERS substrates under 785 nm excitation of the Raman probe 4-acetamidothiophenol (4-AMTP).

1.1.1   Experimental characterization

- *Samples preparation*

We investigated the performance of different cluster arrays as SERS substrates under 785 nm excitation, using 4-acetamidothiophenol (4-AMTP) as a model probe. An optimized cleaning procedure was necessary prior to the SERS measurements. To this end, the nanoparticle assemblies were treated first with oxygen plasma (0.4 mbar O_2, 200 W, 1 min) and then exposed to UV-O_3 treatment for 30 min.

Immediately after cleaning, the substrates were incubated in 800 μL of a freshly prepared 0.1 mM aqueous 4-AMTP solution for at least 60 min. Next, the samples were intensively rinsed with water to remove unbound molecules and dried in a N_2 stream.

- *Probing different lattice supercrystals*

A representative SERS spectrum of 4-AMTP is shown as an inset in Figure 5.2, revealing the characteristic main vibrational modes at 1081 cm^{-1} (C-S and ring stretch) and at 1591 cm^{-1} (ring stretch).[24] In order to assess to what extent the lattice resonance mode influences the SERS signal of the substrates, we compared different monolayer cluster arrays with L = 400, 500, 600, and 740 nm. Whereas the lattice resonances of the largest arrays are far away from the spectral region of interest, we observed that for this geometry, clusters with up to three AuNSs layers can be obtained due to the increased depth of the holes in the mold which allowed us to study also the influence of cluster height on the SERS enhancement.

We explored the local homogeneity of the samples by recording 100 individual data points over an area of 10×10 μm^2 and averaging for each measurement. As the SERS effect directly mirrors the near-field generated at the nanometer scale, even subtle changes in the local NP order, as well as the number and geometry of hot spots, can cause significant intensity fluctuations. Additionally, the 3D packing of AuNSs into multilayered structures is known to affect the SERS response.[25] Therefore, a precise correlation of the local array morphology with the recorded signal enhancement was ensured through SEM characterization of the sites selected for SERS measurements. The results are summarized in Figure 5.2, where the baseline-corrected average intensity of the 1081 cm^{-1} vibration is plotted as a function of the lattice parameter, for a typical set of measurements. For superlattices consisting of monolayer clusters (green triangles), a decrease of L from 740 to 500 nm leads to a nearly linear signal increase by over 200%, followed by a slight drop at L=400 nm, in agreement with the predictions from FDTD simulations. The sample with L=740 nm further exemplifies how the extension from 2D to 3D assembly affects the SERS response: with the transition from monolayer to double layer clusters (red circle) the average SERS signal rises by more than 90%, whereas a third layer (blue square) leads to a further signal enhancement of only 30%.
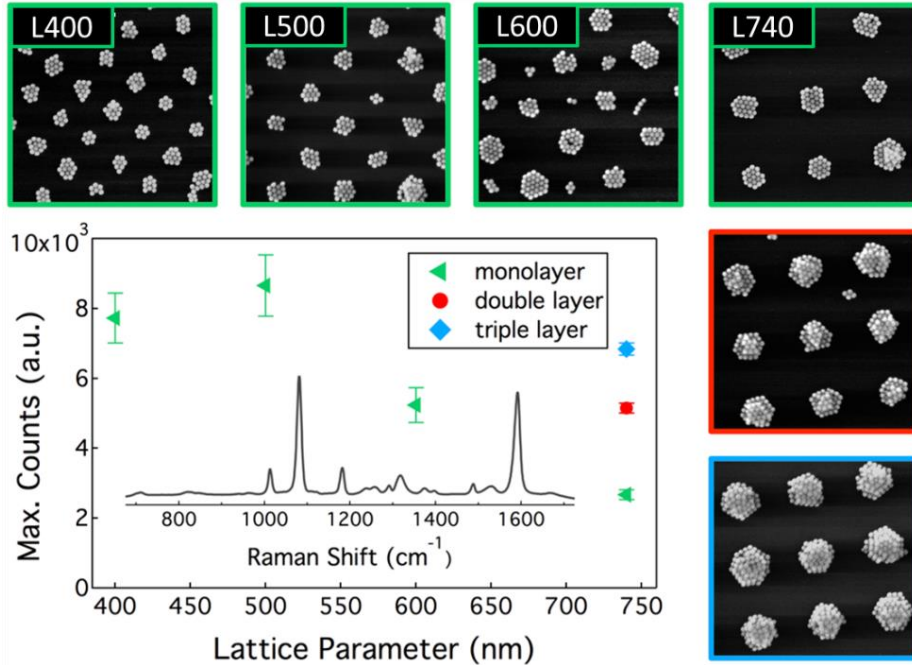
Figure 5.2. SERS signal at 1081 cm^{-1}, as a function of the lattice parameter. The error bars depict the standard deviation of the signal in the probed 10×10 μm² areas. The inset spectrum was recorded on a sample with L= 500 nm.

We attribute the higher counts to an increased hot spot density due to the 3D packing. These results suggest that layered substrates are more efficient that monolayers. However, to correctly evaluate the efficiency of the system, a detailed characterization of the probed arrays compared with random layer substrate (Figure 5.3) is needed. Figure 5.4 illustrates the plot of the SERS intensity normalized by the surface density of particles.
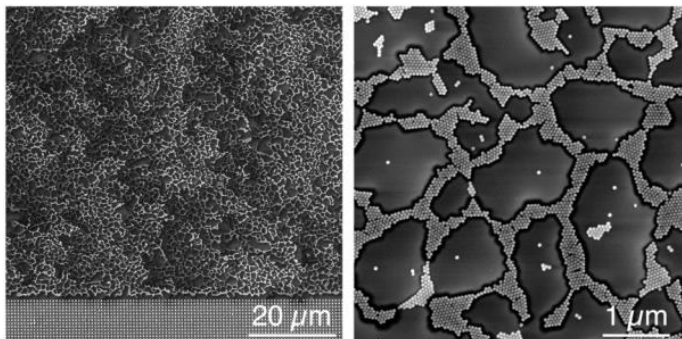

Figure 5.3 Particle assembly at the border between structured and non-structured regions.
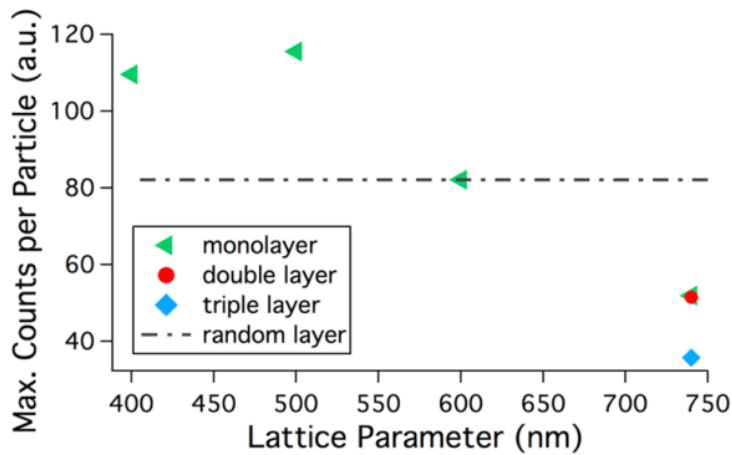
Figure 5.4 SERS signal at 1081 cm⁻¹, normalized to the local particle density obtained from SEM images. The average signal per particle was found to be weakest for periodic nanoparticle assemblies whose extinction maximum was optically detuned from the excitation wavelength of 785 nm.

Overall, samples with an optical resonance close to the excitation wavelength of the laser exhibited significantly higher SERS enhancement than detuned samples. Intriguingly, monolayer samples tailored to the excitation wavelength (*L*=500 nm) yielded a total signal, even higher than that from non-optimized multilayer arrays containing nearly three times as many particles (*L*=740 nm). It should be noted that for arrays with small lattice parameters the average local SERS signals typically fluctuated more (10-20% standard deviation for *L*=400 and 500 nm) than for assemblies with large lattice parameters (2-5% standard deviation for *L*=600 and 740 nm).

- *Intrabatch signal homogeneity*

Interestingly, probing monolayer arrays of varying quality with the same lattice parameter (*L*=500 nm), revealed a clear correlation between the standard deviation and the average SERS signal. An example is displayed in Figure 5.5a, showing that ordered arrays (stdev~10%) reached up to 5 times higher enhancement than irregular ones (stdev~35%). SEM inspection further confirmed that both homogeneity and signal intensity are strongly correlated to the average cluster size, for a given *L*. Plotting the normalized signal at 1081 cm⁻¹ as a function of the average cluster size revealed that the pronounced increase

in SERS enhancement is not exclusively due to an increased number of hot spots. As can be seen in Figure 5.5b, the counts per particle (*i.e.,* per hot spot) remained nearly constant below a threshold value of 15, above which further enhancement was registered until reaching the geometrically determined maximum cluster size of 19 particles. The signal per particle achieved with full cluster arrays (*i.e.,* 19 particles for *L*=500 nm) was at least 3 times higher than that for a random sub-monolayer, obtained using the same method but a non-structured stamp.
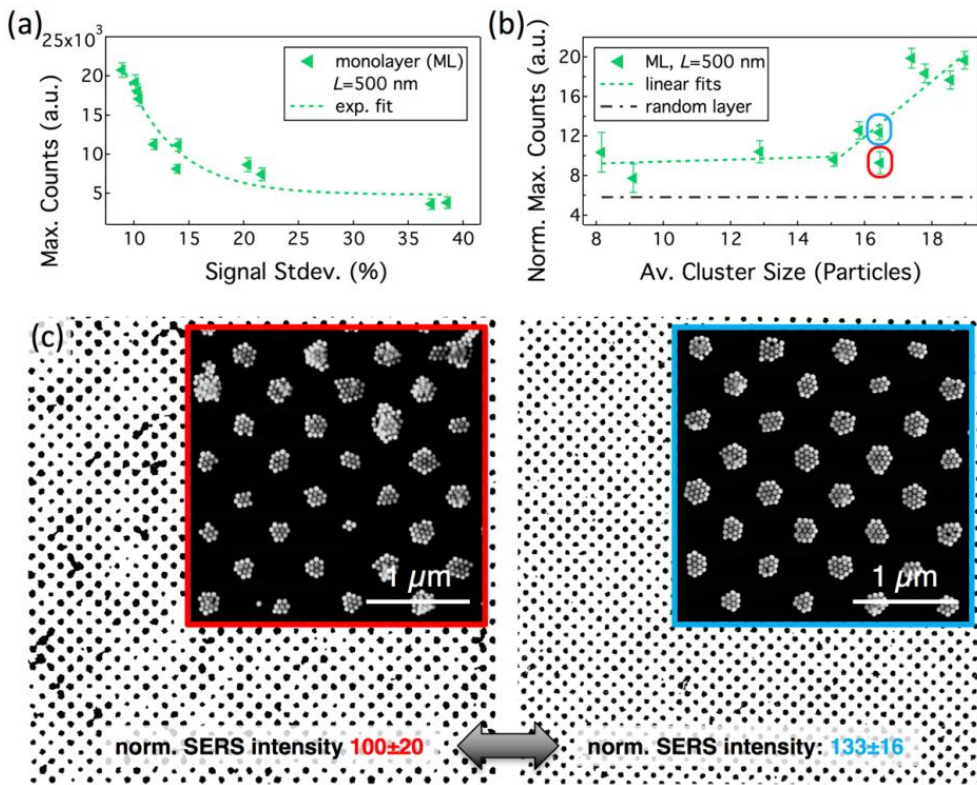

Figure 5.5 Correlated SERS and SEM characterization of monolayer arrays with fixed L=500 nm and varying degree of assembly quality. (a) Increasing inhomogeneity, represented by the standard deviation (Stdev) of counts at 1081 cm⁻¹, was accompanied by an overall decrease in signal strength. (b) The signal per particle was nearly constant for clusters smaller than 15 particles, but increased for larger clusters. The grey, dashed line depicts the signal of a random monolayer. (c) For clusters of identical average diameter (marked by red and blue circles in b), the normalized signal depends strongly on the order within the array, illustrated with binary and inset grayscale SEM images. The error bars in (a,b) correspond to the standard deviation of the signal within the probed 10×10 μm² areas.

These observations are in agreement with FDTD simulations of different cluster arrays with L=500nm, predicting both a cluster size-dependent hybridization efficiency and stronger near-field enhancement in periodic arrays, as compared to isolated clusters. A certain scatter of the counts per particle observed for clusters of identical size can be attributed to local structural defects: as illustrated in Figure 5.5c, comparing two arrays with identical lattice parameter and average cluster diameter, the enhancement clearly depends on the degree of order within the assembly, *i.e.*, on the strength of the lattice resonance.

- *Inter batch signal homogeneity*

The homogeneity of the signal among different samples, was evaluated from 4 different L 500 nm supercrystal assemblies (Figure 5.6 A to D) by incubating the samples in a 5x10-4 M solution of AcTP for 1h. Intra-batch homogeneity was obtained by averaging the SERS intensity of five, randomly chosen 10 x 10 μm² areas distributed over the entire array region, thereby dividing each selected square again into 100 single spectra points.

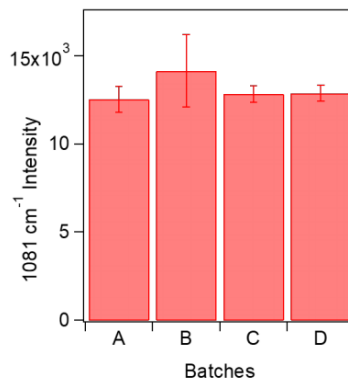*Figure 5.6 Intra-batch and batch-to batch homogeneity tests for 4 supercrystal films with lattice parameter L = 500 nm, named A to D. Intra-batch homogeneity was obtained by averaging the SERS intensity of five, randomly chosen 10 ´ 10 μm2 areas distributed over the entire array region, thereby dividing each selected square again into 100 single spectra points.*

They show that, except for batch B, the mean SERS intensity is nearly constant with standard deviation values below 6% supporting the good SERS performance, high cluster array homogeneity and batch-to batch reproducibility for three of four batches. The higher mean SERS intensity of

batch B together with the considerably higher standard deviation (14%) indicates that this sample lacks the same degree of large-scale homogeneity. They show that, except for batch B, the mean SERS intensity is nearly constant with standard deviation values below 6% supporting the good SERS performance, high cluster array homogeneity and batch-to batch reproducibility for three of four batches. The higher mean SERS intensity of batch B together with the considerably higher standard deviation (14%) indicates that this sample lacks the same degree of large-scale homogeneity.

5.3.1 Theoretical simulation

Simulation has been done to shed light on the performance of supercrystals nanoparticle array. Insight into the physical origin of the hybridized lattice resonances is gained by comparing the measured extinction spectra with the simulated absorption of the corresponding periodic structures, calculated by Finite Difference Time Domain simulations (FDTD). The values of AuNSs per unit area were calculated according to geometrical considerations, confirmed by inspection of SEM micrographs and listed in table 5.1. A corresponding SEM image of each model cluster type, with similar density to the SEM images, is included as an inset in Figure 5.7c,d,e.

Lattice parameter (nm)	NPs/μm^2 (geometrical)	NPs/μm^2 (SEM visualization)
400	75	70
500	76	75
600	83	64
740	89	52
1600	110	85

Table 5.1 Number of nanoparticles (NPs) by area considering one layer of NPs: in the case of the maximum number of NPs that fill a hole in the PDMS mold (geometrical) and by visual inspection of the SEM micrographs (SEM visualization).

The comparison between different lattice paramenter is displayed in Figure 5.7a,b for assemblies with *L*=400, 500, and 600 nm, all having similar filling factors of AuNSs (*FF*=0.25 - 0.27), which correspond to maxima particle densities of 75, 76 and 83 AuNSs/μm², respectively.
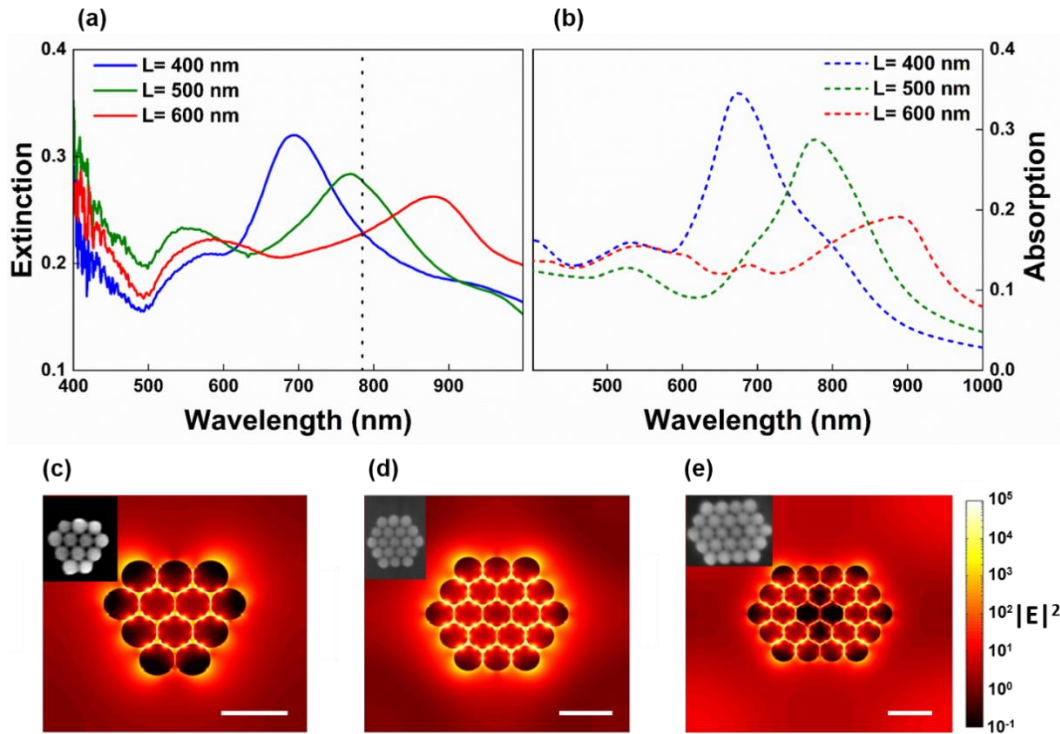

Figure 5.7. (a) Extinction spectra measured from AuNSs arrays for varying lattice parameter L. The black dashed line marks the excitation laser wavelength used for surface-enhanced Raman spectroscopy, λ=785 nm. (b) Absorption spectra from FDTD simulations. (c,d,e) Snapshots of a transversal cut of an AuNSs superlattice unit cluster (insets are SEM micrographs with analogous configuration), showing the intensity of the electric field |E|², for lattice parameters L=400 nm, 500 nm, and 600 nm, calculated at an excitation wavelength of 785 nm. Scale bars 100 nm.

As exemplified in Figure 5.8 the cluster size was found to influence the position of the optical resonance only marginally, for assemblies containing 9 or more particles. Still, variations in the configuration and orientation of the clusters lead to a slight damping of the extinction intensity and an increase of the full-width-at-half- maximum (FWHM) in the experimental data, as compared to numerical simulations of periodically arranged, identical clusters. Aside from

that, we find excellent agreement between the measured and the calculated spectra.
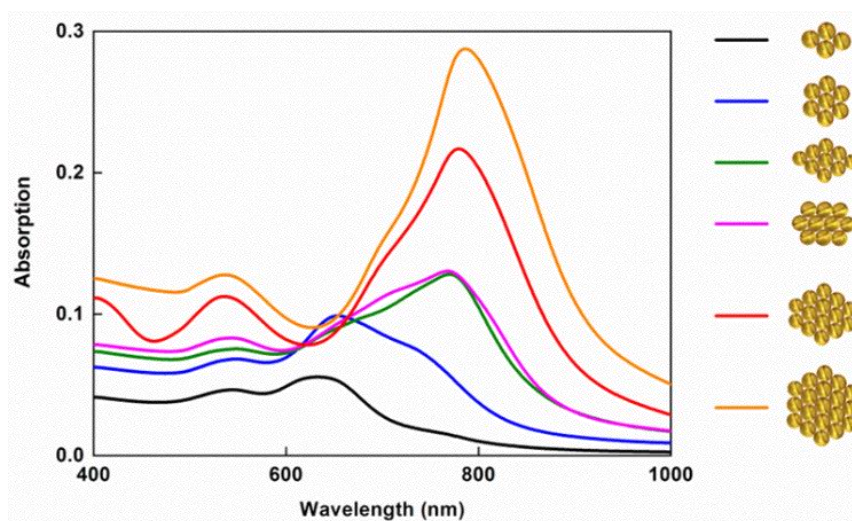

Figure 5.8. FDTD calculations of absorption spectra for periodic arrays of clusters with different cluster size and the same lattice parameter L=500 nm. Unpolarized light at normal incidence was used

In general, the spectral position of the plasmon resonances is expected to correlate with the excitation of the highest local field factor and to affect the maximum Raman signal enhancement.[8] This should allow us to engineer the optical properties of the AuNSs assemblies in a straightforward manner, toward targeting excitation with a specific laser line. Herein, we focus on irradiation with a laser of 785 nm wavelength. Comparing the extinction spectra of supercrystals films with different geometries (Figure 5.7a, b) we find that arrays with lattice parameter *L*=500 nm have their main resonance band close to 785 nm. Snapshots of the electric field intensity $|E|^2$ at a transversal section of the periodic AuNSs cluster arrays (Figure 5.7c,e) also display the highest enhancement for the lattice with *L*=500 nm, under excitation at 785 nm. This extra field enhancement originates from the periodic arrangement of the plasmonic clusters in a square lattice, which becomes obvious when comparing the field enhancement profiles of isolated and periodically arranged clusters depicted in Figure 5.9.
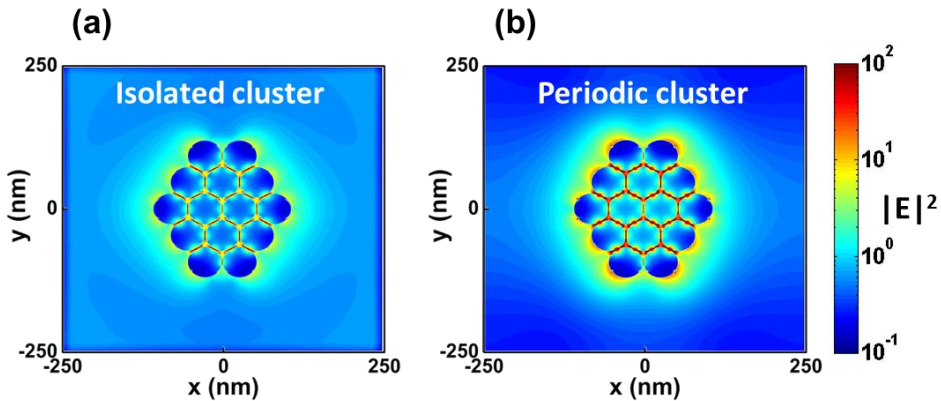
Figure 5.9. Snapshots of a transversal cut of a cluster of AuNPs, showing the intensity of the electric field |E|² upon excitation at λ=785 nm for an isolated cluster (a) and a cluster in a periodic assembly with lattice parameter L=500 nm (b). Both samples are illuminated with unpolarized light at normal incidence

Average enhancement factor spectra were calculated by averaging the surface integral of the field enhancement factor $\frac{|E|^4}{|E_0|^4}$ over the whole surface of the available gold nanospheres, where E_0 is the incident electric field. This result further corroborate the lattice-dependent enhancement effect and again predict the strongest fields for *L*= 500 nm (Figure 5.10).[26]
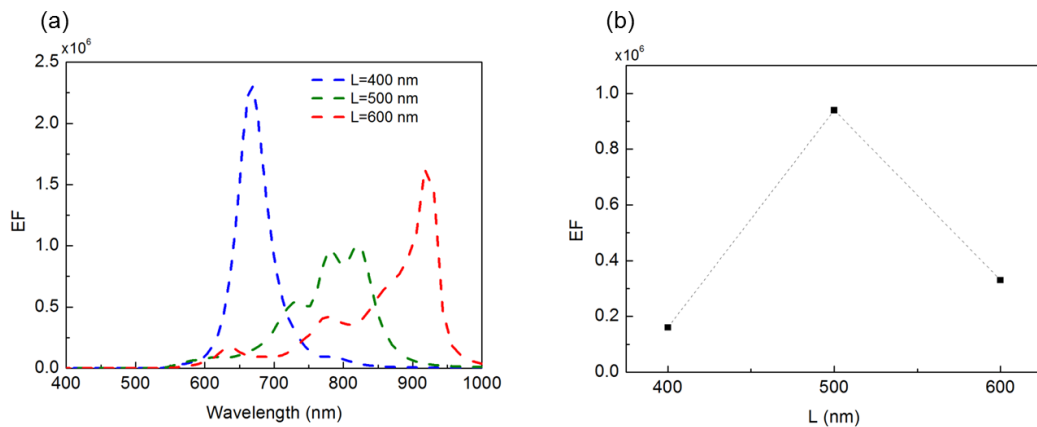

Figure 5.10 (a) FDTD calculations of the average enhancement factor (EF) spectra for different lattice parameters, L, normalized by the number of AuNSs per μm². (b) Extracted EF values at λ=785 nm for different lattice parameters, L. Linear polarization in x-direction of the electric field at normal incidence was used for these numerical calculations.

5.4 CONCLUSIONS

In this chapter we studied the optical response of plasmonic crystals nanoparticles mesostructures in order to engineer their SERS performance. We explored the performance of 2D cluster arrays as SERS substrates, using 4-AMTP as a model Raman probe. Correlation of Raman and SEM measurements demonstrated that, lattices with a periodicity L=500 nm were the most effective SERS platforms under 785 nm laser excitation, in agreement with the predictions by a simple model based on extinction. The signal intensity was also found to strongly depend on the degree of order within the arrays, and, intriguingly, monolayer clusters with the optimal lattice parameter may even display larger enhancement than non-optimized multilayered assemblies. Investigation of L=500 nm monolayer arrays of different qualities indicated that the SERS intensity per particle grows linearly with the particle number, for clusters containing more than 15 particles, eventually reaching over three-fold enhancement as compared to non-resonant random assemblies. This process thus paves the way toward highly efficient, uniform and reproducible SERS substrates.

5.5 REFERENCES

(1) Fedick, P. W.; Bills, B. J.; Manicke, N. E.; Cooks, R. G. Forensic Sampling and Analysis from a Single Substrate: Surface-Enhanced Raman Spectroscopy Followed by Paper Spray Mass Spectrometry. *Anal. Chem.* **2017**, *89*, 10973–10979.

(2) Baumberg, J.; Bell, S.; Bonifacio, A.; Chikkaraddy, R.; Chisanga, M.; Corsetti, S.; Delfino, I.; Eremina, O.; Fasolato, C.; Faulds, K.; Fleming, H.; Goodacre, R.; Graham, D.; Hardy, M.; Jamieson, L.; Keyes, T.; Królikowska, A.; Kuttner, C.; Langer, J.; et al. SERS in Biology/Biomedical SERS: General Discussion. *Faraday Discuss.* **2017**, *205*, 429–456.

(3) Premasiri, W. R.; Chen, Y.; Fore, J.; Brodeur, A.; Ziegler, L. D. SERS Biomedical Applications: Diagnostics, Forensics, and Metabolomics. *Front. Adv. Mol. Spectrosc.* **2017**, 327–367.

(4) Sun, F.; Hung, H.-C.; Sinclair, A.; Zhang, P.; Bai, T.; Galvan, D. D.; Jain, P.; Li, B.; Jiang, S.; Yu, Q. Hierarchical Zwitterionic Modification of a SERS Substrate Enables Real-Time Drug Monitoring in Blood Plasma. *Nat. Commun.* **2016**, *7*, 13437.

(5) Graham, D.; Goodacre, R.; Arnolds, H.; Masson, J.-F.; Schatz, G.; Baumberg, J.; Kim, D.-H.; Aizpurua, J.; Lum, W.; Silvestri, A.; de Nijs, B.; Xu, Y.; Di Martino, G.; Natan, M.; Schlücker, S.; Wuytens, P.; Bruzas, I.; Kuttner, C.; Hardy, M.; et al. Theory of SERS Enhancement: General Discussion. *Faraday Discuss.* **2017**, *205*, 173–211.

(6) Jeanmaire, D. L.; Van Duyne, R. P. Surface Raman Spectroelectrochemistry: Part I. Heterocyclic, Aromatic, and Aliphatic Amines Adsorbed on the Anodized Silver Electrode. *J. Electroanal. Chem. Interfacial Electrochem.* **1977**, *84*, 1–20.

(7) Albrecht, M. G.; Creighton, J. A. Anomalously Intense Raman Spectra of Pyridine at a Silver Electrode. *J. Am. Chem. Soc.* **1977**, *99*, 5215–5217.

(8) Moskovits, M. Persistent Misconceptions Regarding SERS. *Phys. Chem. Chem.*

Phys. **2013**, *15*, 5301.

(9)   Luo, S.-C.; Sivashanmugan, K.; Liao, J.-D.; Yao, C.-K.; Peng, H.-C. Nanofabricated SERS-Active Substrates for Single-Molecule to Virus Detection in Vitro: A Review. *Biosens. Bioelectron.* **2014**, *61*, 232–240.

(10)   Willets, K. A.; Van Duyne, R. P. Localized Surface Plasmon Resonance Spectroscopy and Sensing. *Annu. Rev. Phys. Chem* **2007**, *58*, 267–297.

(11)   Yang, A.; Hoang, T. B.; Dridi, M.; Deeb, C.; Mikkelsen, M. H.; Schatz, G. C.; Odom, T. W. Real-Time Tunable Lasing from Plasmonic Nanocavity Arrays. *Nat. Commun.* **2015**, *6*.

(12)   Cha, H.; Yoon, J. H.; Yoon, S. Probing Quantum Plasmon Coupling Using Gold Nanoparticle Dimers with Tunable Interparticle Distances Down to the Subnanometer Range. *ACS Nano* **2014**, *8*, 8554–8563.

(13)   Hao, E.; Schatz, G. C. Electromagnetic Fields around Silver Nanoparticles and Dimers Shape Effects in Plasmon Resonance of Individual Colloidal Silver Nanoparticles Experimental Observation of Narrow Surface Plasmon Resonances in Gold Nanoparticle Arrays Electromagnetic Fields. *J. Chem. Phys.* **2004**, *120*, 11101–10871.

(14)   Huang, Y.; Zhou, Q.; Hou, M.; Ma, L.; Zhang, Z. Nanogap Effects on Near-and Far-Field Plasmonic Behaviors of Metallic Nanoparticle Dimers. *Phys. Chem. Chem. Phys. Phys. Chem. Chem. Phys* **2015**, *17*, 29293–29298.

(15)   Mosier-Boss, P. A. Review of SERS Substrates for Chemical Sensing. *Nanomaterials* **2017**, *7*, 142.

(16)   Strobbia, P.; Languirand, E.; Cullum, B. M. Recent Advances in Plasmonic Nanostructures for Sensing: A Review. *Opt. Eng.* **2015**, *54*, 100902.

(17)   Kraus, T.; Malaquin, L.; Schmid, H.; Riess, W.; Spencer, N. D.; Wolf, H. Nanoparticle Printing with Single-Particle Resolution. *Nat. Nanotechnol.* **2007**, *2*, 570–576.

(18)   Hanske, C.; Müller, M. B.; Bieber, V.; Tebbe, M.; Jessl, S.; Wittemann, A.; Fery, A. The Role of Substrate Wettability in Nanoparticle Transfer from Wrinkled Elastomers: Fundamentals and Application toward Hierarchical Patterning. *Langmuir* **2012**, *28*, 16745–16750.

(19)   Volk, K.; Fitzgerald, J. P. S.; Ruckdeschel, P.; Retsch, M.; König, T. A. F.; Karg, M. Reversible Tuning of Visible Wavelength Surface Lattice Resonances in Self-Assembled Hybrid Monolayers. *Adv. Opt. Mater.* **2017**, *5*, 1600971.

(20)   Greybush, N. J.; Liberal, I.; Malassis, L.; Kikkawa, J. M.; Engheta, N.; Murray, C. B.; Kagan, C. R. Plasmon Resonances in Self-Assembled Two-Dimensional Au Nanocrystal Metamolecules. *ACS Nano* **2017**, *11*, 2917–2927.

(21)   Gu, X.; Tian, S.; Zhou, Q.; Adkins, J.; Gu, Z.; Li, X.; Zheng, J. SERS Detection of Polycyclic Aromatic Hydrocarbons on a Bowl-Shaped Silver Cavity Substrate. *RSC Adv.* **2013**, *3*, 25989.

(22)   Polavarapu, L.; Liz-Marzán, L. M. Towards Low-Cost Flexible Substrates for Nanoplasmonic Sensing. *Phys. Chem. Chem. Phys.* **2013**, *15*, 5288.

(23)   Bodelón, G.; Montes-García, V.; López-Puente, V.; Hill, E. H.; Hamon, C.; Sanz-Ortiz, M. N.; Rodal-Cedeira, S.; Costas, C.; Celiksoy, S.; Pérez-Juste, I.; Scarabelli, L.; La Porta, A.; Pérez-Juste, J.; Pastoriza-Santos, I.; Liz-Marzán, L. M. Detection and Imaging of Quorum Sensing in Pseudomonas Aeruginosa Biofilm Communities by Surface-Enhanced Resonance Raman Scattering. *Nat. Mater.* **2016**, *15*, 1203–1211.

(24)   Zhang, Y.; Li, X.; Xue, B.; Kong, X.; Liu, X.; Tu, L.; Chang, Y. A Facile and General Route to Synthesize Silica-Coated SERS Tags with the Enhanced Signal Intensity. *Sci. Rep.* **2015**, *5*.

(25)   Hamon, C.; Novikov, S. M.; Scarabelli, L.; Solís, D. M.; Altantzis, T.; Bals, S.; Taboada, J. M.; Obelleiro, F.; Liz-Marzán, L. M. Collective Plasmonic Properties in Few-Layer Gold Nanorod Supercrystals. *ACS Photonics* **2015**, *2*, 1482–1488.

(26)   Huang, Y.; Zhang, X.; Ringe, E.; Hou, M.; Ma, L.; Zhang, Z. Tunable Lattice Coupling of Multipole Plasmon Modes and Near-Field Enhancement in Closely Spaced Gold Nanorod Arrays. *Sci. Rep.* **2016**, *6*, 23159.

GENERAL CONCLUSIONS AND OUTLOOKS

This thesis has been devoted to the fabrication of large scale plasmonic crystals using hybrid top down and bottom up approaches that enable unprecedented control over several nanofabrication parameters while overcoming the main drawbacks of each approach. The optical characterization allowed to unveil the origin of phenomena such as the interference between localized surface plasmon resonances with propagating plasmons. The most significant contributions from the studies developed throughout these years are given below.

Asymmetric plasmonic crystals for enhanced spectroscopy

- Nanoimprint lithography, together with oblique angle metal deposition was used to fabricate new asymmetric nanostructures. The possibility to control fabrication parameters such as tilt angle, multiple evaporation setups, lattice parameter of the array and finally feature depth and shape, demonstrated the ease of tuning of highly homogeneous large scale plasmonic devices.

- The fabrication process has led to the successful fabrication of metallic array of wedges, spoon-like nanostructures, nanogaps half metallic pillars and chiral nanostructures each of them producing homogeneous and selective optical response upon the inspection with linearly or circularly polarized light.

- Photoluminescence enhancement and shaping have been also demonstrated with nanogaps array. The ordered lattice along with the

presence of nanogaps has been found responsible for the 20-fold selective enhancement of emission of ATTO655.

Gold Nanoparticle Plasmonic Superlattices for SERS

- Template self-assembly of gold nanoparticles into hierarchically organized plasmonic mesostructures has been optimized using PDMS molds as templates and highly concentrated surfactant stabilized gold nanoparticles. We achieved regular square arrays of hexagonally packed gold nanospheres and lying lamellae gold nanorods, reaching periodicities down to 400 nm and feature sizes of 200 nm, over areas up to 1 cm^2.

- The use of PDMS templates to drive colloidal organization resolved the lack of large scale homogeneity, demonstrating the efficient bridging of vastly different length scales from nanometer to millimeter dimensions. The template self-assembly approach largely improves the large-scale reproducibility and overall quality of the resulting arrays. As the crucial experimental parameters in this method, we identified the dispersion medium composition, solvent evaporation time, particle concentration, and surfactant concentration. A strong correlation was found between particle pre-assembly and quality of the resulting final substrate.

- We efficiently tune the optical response of plasmonic system without any shape and size modification but thanks to the organization of colloids in clusters arrays. Concretely, these two-dimensional supercrystals exhibited well-defined collective plasmon modes that can be shifted throughout the visible and NIR ranges by changing lattice constant. Further theoretical modeling confirmed that the resonances originate from the hybridization of photonic lattice modes with plasmonic resonances sustained by individual AuNPs clusters.

- We designed the optical properties of different supercrystals to enhance the intensity of hot spots resonances in nanoparticles clusters. Concretely, using ordered arrays, we increased the absorption cross-section by hundreds of times in relation with single nanoparticles. These resonances have been tuned to match the first biological transparency window (785nm) so opening the possibility to use these platform with biological media. We explored the performance of 2D cluster arrays as SERS substrates, using 4-AMTP as a model Raman probe. Correlation of Raman and SEM measurements demonstrated that, lattices with a periodicity *L*=500 nm were the most effective SERS platforms under 785 nm laser excitation, in agreement with the predictions by a simple model based on extinction. Intra batch and inter batch analysis demonstrate the dependency of the signal on the overall cluster homogeneity, as well as the reproducibility of the signal among different substrates.

This works pave the way for further developments of supercrystals based on template self-assembly and will enable real device implementation for sensing.

Final remarks

Nanotechnology is enabling us to create functional materials, devices, and systems by controlling matter at the atomic and molecular scales. This field has been breaking at high pace into our daily life from almost two decades and in order to keep this trend it needs to continuously evolve.

Overall, this work is a demonstration of how the field of nanotechnology is evolving. On one hand we have the sought of new, affordable and low cost nanofabrication techniques. On the other hand, thanks to the development of advanced characterization techniques and precise theoretical modelling, we are improving the common knowledges on the physical and chemical phenomena arising at the nanoscale.

Today most of the nano research is heading toward the development of method and techniques to bridge the gap between vastly different length scales. Thus a complete merger of nanoscale, mesoscale and macroscale engineering will transform the nanotechnology into a more complex broad field of science where the synergic interaction between different disciplines will drive next generation breakthrough.

APPENDIX A

5.6 A.1. PEER-REVIEWED PUBLICATIONS

- C. Matricardi, J. L. Garcia-Pomar, P. Molet, L. Perez, M. Isabel Alonso, M. Campoy-Quiles and A. Mihi "Symmetry Breaking Plasmonic Crystals for Polarization Dependent Response" In preparation **2020**.

- C. Hanske, E. H. Hill, D. Vila-Liarte, G. González-Rubio, C. Matricardi, A. Mihi, L.M. Liz-Marzán "Solvent-Assisted Self-Assembly of Gold Nanorods into Hierarchically Organized Plasmonic Mesostructures" ACS applied materials & interfaces **2019** 11,12, 11763-11771

- C. Matricardi, C. Hanske, J. L. GarciaPomar, J. Langer, A. Mihi, and L.M. Liz-Marzán **"**Gold Nanoparticle Plasmonic Superlattices as Surface Enhanced Raman Spectroscopy Substrates" ACS nano **2018** 12, 8, 8531-8539

- Espinha, C. Dore, C. Matricardi, M.I. Alonso, A.R. Goñi, A. Mihi. "Hydroxypropyl Cellulose Photonic Architectures by Soft Nanoimprinting Lithography"Nature Photonics **2018**, 12, 343–348.

- P. Molet , J.L. Garcia-Pomar, C. Matricardi, M. Garriga, M.I. Alonso, A. Mihi. "Ultrathin Semiconductor Superabsorbers from the Visible to the Near-Infrared"Advanced Materials **2018**, 30, 1705876

- D. Graham, R. Goodacre, H. Arnolds, J. Masson, G. Schatz, J. Baumberg, D. Kim, J. Aizpurua, W. Lum, A. Silvestri, B. De Nijs, Y. Xu, G. Di Martino, M.

Natan, S. Schlücker, *Et. Al.* "Theory of SERS enhancement: general discussion" Faraday Discussions, **2017**, 205, 173-211.

5.7 A.2. CONTRIBUTIONS TO SCIENTIFIC EVENT

• "Asymmetric Plasmonic-Photonic Architectures for enhanced fluorescence" Poster presentation at NANOP international conference. Best poster presentation award. Munich, Germany **2019**

• AMOLF nanophotonics school, Amsterdam, 17-21 June **2019**

• Member of the organization committee of the 3rd Scientific Meeting of BNC-b PhD Students, Barcelona, June **2019**

• "Polarization dependent fluorescence enhancement by asymmetric plasmonic crystals" Oral Presentation at Organic Electronics Meeting (ORGI), Barcelona ES, May **2019**

• "Template assisted serf assembly as a tool for rapid fabrication of nanoparticles arrays" Poster and Flash presentation at Self-assembly of colloidal system summer school (SACS), Bordeaux FR, September **2018**

• "Gold Nanoparticle-based supercrystals as Surface Enhanced Raman Scattering (SERS) substrates"; Oral presentation at Imagenano conference, Bilbao ES, March **2018**

• "Plasmonic nanostructures for SERS"; Oral presentation at Scientific Meeting of BNC-b PhD Students, Barcelona ES, November **2017**

- <u>"Tunable optical properties of gold nanoparticles supercrystals</u>"; Poster presentation at Faraday Discussion conference, Glasgow UK, August **2017**

- "Light, crystals and other fancy stuff" Oral presentation to broad audience at the 11th Barcelona Science Festival, Barcelona, June **2017**